858

LUMINESCENT DECAY AND SPECTRA OF IMPURITY-ACTIVATED ALKALI HALIDES UNDER HIGH PRESSURE

BY

DAVID IRA KLICK

B.A., Lawrence University, 1973
M.S., University of Illinois, 1974

THESIS

Submitted in partial fulfillment of the requirements
for the degree of Doctor of Philosophy in Physics
in the Graduate College of the
University of Illinois at Urbana-Champaign, 1977

Urbana, Illinois

LUMINESCENT DECAY AND SPECTRA OF IMPURITY-ACTIVATED ALKALI HALIDES UNDER HIGH PRESSURE

BY

DAVID IRA KLICK

B.A., Lawrence University, 1973
M.S., University of Illinois, 1974

THESIS

Submitted in partial fulfillment of the requirements
for the degree of Doctor of Philosophy in Physics
in the Graduate College of the
University of Illinois at Urbana-Champaign, 1977

Urbana, Illinois

LUMINESCENT DECAY AND SPECTRA OF IMPURITY-ACTIVATED ALKALI HALIDES UNDER HIGH PRESSURE

David Ira Klick, Ph.D.
Department of Physics
University of Illinois at Urbana-Champaign, 1977

The effect of high pressure on the luminescence of alkali halides doped with the transition-metal ions Cu^+ and Ag^+ and the heavy-metal ions In^+ and Tl^+ was investigated to 140 kbar. Measurement of spectra allowed the prediction of kinetic properties, and the predictions agree with lifetime data.

In view of the localized nature of the electronic transitions, a pressure-dependent single configuration coordinate model is used to interpret the luminescence data. While pressure affects the volume, it also couples to the nontotally symmetric coordinates that determine the lifetime in the phosphors studied here. Luminescent kinetics are governed by the assistance of odd phonons for Cu^+ and Ag^+, and by Jahn-Teller distortions for In^+ and Tl^+.

Analysis of room-temperature measurements of emission peak location and peak halfwidth yields parameters characteristic of the potential wells of transition-metal ions in alkali halides. Using a pressure-dependent model of phonon-assisted transitions, these parameters predict the change in lifetime with pressure. Agreement between calculation and the experimentally determined lifetime is reasonable. The possibilities and limitations of the analysis are discussed.

Measurements of steady-state intensity and lifetime were made over a range of pressures (4 to 60 kbar) and temperatures (100 to 300°K) for

five alkali halide crystals doped with In^+ and Tl^+. The emission spectrum is a doublet (or a triplet in the case of CsI:Tl), caused by a Jahn-Teller splitting of the excited state. The relative intensity distribution of the spectral peaks as a function of temperature and pressure determines the parameters for a model of two levels in "dynamic equilibrium." The same model predicts lifetime changes with temperature and pressure which are in excellent agreement with the data for the In^+-doped compounds. For the Tl^+-doped compounds, metastable states control the lifetime, and parameters are extracted from the data for a multi-level model. Level splittings, level degeneracies, and intrinsic radiative rates are among the parameters determined in this study.

Lifetimes were found from low-light level decay curves recorded after pulsed light excitation. A signal-averaging transient digitizer was used for lifetimes from one microsecond to five seconds. The single-photon counting method was employed for fast lifetimes of one hundred nanoseconds to fifty microseconds.

To

my parents,

Ruth and Clifford Klick

ACKNOWLEDGMENTS

The author wishes to express appreciation to Professor H. G. Drickamer for his guidance in this work. His enthusiastic and dedicated approach to research is an example for all of us.

Around Dr. Drickamer has gathered a group of students of exceptionally high scientific ability and sense of purpose. Among these are several who provided assistance that was invaluable in completing this thesis: Mr. John Hook took some of the data on KI:In and helped with the kinetics arguments found in Part 4. Dr. Kevin Bieg wrote the computer program DECAY and collaborated on the project found in Part 3. Dr. Craig Tyner helped bring the single photon counting apparatus to the point where it works routinely. Mr. Grant Webster wrote the single photon counting correction in computer program DECAY and helped in setting up the photon counting equipment. Mr. George Chryssomallis designed and built the "SPC Control" circuit for the single photon counting apparatus.

Thanks are also due to Mr. Ronald Harrison for constructing the lifetime apparatus (including the spark gap) and to the members of the electronics shop in the Department of Chemistry, who designed or built some of the circuits. The author soon learned that most problems in construction and electronics were best taken to these experts, who immediately provided friendly assistance.

The financial support of the United States Energy Research and Development Administration (contract number 1198) is acknowledged, as is administrative help from the Department of Physics and the Materials Research Laboratory.

The author would especially like to thank his parents. He is, of course, greatly in their debt from his years at home, but their continuing interest and encouragement are just as highly valued. The author is grateful beyond words to his wife, Beverly. From the beginning to the end of the study leading to this thesis, she kept him happy. Her drafting of most of the figures in this thesis is but a small part of the help she has been in its development.

TABLE OF CONTENTS

INTRODUCTION

The impurity-activated alkali halides have been studied extensively. The specific impurities investigated in this work are the transition-metal ions Cu^+ and Ag^+, and the heavy-metal ions In^+ and Tl^+. Incorporating such an ion into the alkali halide lattice greatly alters its optical properties, causing the host to absorb light in spectral regions where it had been transparent before doping. Typically, the absorbed light is emitted as luminescence, the characteristics of which are specific to the particular impurity. The property of luminescence had led to the widespread use of these phosphors (particularly CsI:Tl) as scintillation counters for particle detection. They are intrinsically interesting as well, and have been widely studied both experimentally and theoretically.

This is a study of the effects of high pressure on the luminescence from impurity-activated alkali halides. High pressure is a useful tool for probing material properties; its most common effect is to cause changes in the relative energies of electronic states. These energy differences can be monitored by spectral measurements. Through shifting energy levels or changing transition probabilities, pressure has been shown to strongly affect the efficiency of luminescence. Study of the efficiency and kinetics of luminescence under high pressure can lead to a better understanding of competing processes in the excited state. Such results provide information not only on the pressure effects of the system, but also on the atmospheric pressure interactions between impurity center and host lattice.

The impurity-activated alkali halides are representative of a wide class of phosphors whose interesting optical properties are caused by

defects in the solid. These systems have been studied extensively at atmospheric pressure. One can use this wealth of information to help interpret the pressure effects, which can sometimes be complicated. In turn, the pressure results will be of interest to a large number of workers. Additionally, high pressure is especially useful for studying the alkali halides, because one can investigate physical properties in two different crystal structures. The potassium and rubidium halides undergo a polymorphic phase change between the two structures at modest high pressures. Because of all of this, the doped alkali halides are an ideal choice for an experimental investigation of the pressure effects on optical transitions of localized centers. Spectral properties under high pressure have already been studied for these phosphors in this laboratory, so that the interpretation of the kinetic data presented here rests on other work.

Part 1, which follows immediately, gives a detailed introduction to the topic of luminescence, particularly its time dependence. High pressure and its effects are discussed in general. Part 2 includes sections on experimental methods used here, but not original to this thesis. A complete description of the apparatus for measuring decay curves is given here and in the Appendices. In Part 3 is the study of transition-metal doped alkali halides and a discussion of the effect of pressure on a forbidden transition probability. Part 4 concerns heavy-metal ions in alkali halides, the excited states of which are split by Jahn-Teller distortions. Pressure affects the kinetics of their luminescence by changing the size and direction of the splitting. A summary of the thesis, including the specific results of most interest, is found in Part 5.

1. GENERAL BACKGROUND AND THEORY

1. Historical Review

1.1 High Pressure Research

High pressure is a useful experimental tool in the study of the interaction of atoms and the electronic structure of condensed media [1,2]. When the interatomic distances of a solid are altered by pressure, many of the physical and chemical properties change as well.

The pressure unit used here and in most of the literature is the kilobar (kbar), defined as 10^9 dynes/cm^2. It is the same as 986.92 atmospheres, 1019.72 kg/cm^2, or 10^8 pascals = 10^8 N/m^2.

The means for attaining such high hydrostatic pressures have developed largely from the pioneering work of P.W. Bridgman [3]. His contributions include the principle of cascading cells (where each of a series of nested cells maintains only the pressure difference between neighboring cells) and the Bridgman anvil (which makes use of the principle of massive support, whereby the containing material can be locally stressed well beyond its yield point if the surrounding material is below its yield point). Bridgman anvil devices have achieved static pressures close to 200 kbar.

True hydrostatic pressures above 30 kbar, however, awaited the recent advances in the diamond cell [4], which can reach hydrostatic pressures of 100 kbar, using as a pressure-transmitting medium a mixture of alcohols. Static pressures as high as one megabar have been reported [5] using this cell. Its limitations, as well as some advantages, arise mainly from the miniscule volume of sample used.

The cell used in this laboratory is of the Drickamer supported taper design [6,7]. It is a Bridgman anvil device which employs a compressible

medium (sodium chloride in these optical studies) between the tapered pistons. Pressure gradients across the sample are minimized by the large pressure drop across the supporting material in the tapered region. One can view this design as a continuum of cascading "cells," each one reducing the pressure drop across the ones inside.

Methods that have been used to probe materials inside the Drickamer cell include electrical resistance, x-ray diffraction, Mössbauer resonance, and ultraviolet (uv), visible, and infrared (ir) spectroscopy. The recent monograph of Drickamer and Frank [2] summarizes this research. Other reviews of high pressure techniques and applications are available [8-11].

1.2 Luminescence

Luminescence is the emission of light in excess of thermal radiation. While thermal radiation from a material depends chiefly on the temperature, the spectrum and efficiency of luminescence are dictated by the nature of the material (and also the type of excitation). Thus luminescence, like pressure, is useful as a probe for investigating material properties.

Luminescence is further distinguished from Raman and Rayleigh radiation by the requirement of a time delay between excitation and luminescence that is longer than the period of radiation (on the order of 10^{-15} sec). During the time delay, the luminescent center emits thermal radiation until it reaches the relaxed excited state (RES). Emission (herein used as a synonym for luminescence) occurs some time later, depending on the degree to which the transition from the RES to the ground state is forbidden. Luminescence that occurs within a microsecond (μsec) of excitation, by an essentially allowed transition, is called fluorescence. If the excitation is trapped in a metastable level or if the transition is

nearly forbidden, the luminescence is termed phosphorescence. It is clear that to study the luminescent properties of a material is to investigate its energy levels and their interconnection. The luminescent process can be a complicated one, involving absorption, storage, transfer, and finally emission of energy as uv, visible, or ir radiation.

There are many ways of exciting luminescence. Only photoluminescence (light excitation) has been used in this study. Other sources of excitation are chemical reactions (chemiluminescence), electron beams (cathodoluminescence), electric fields (electroluminescence), mechanical deformation (triboluminescence), and heating (thermoluminescence). In some of these, the excitation is of such low energy that it merely triggers the light emission, detrapping an already excited system. The actual emission transition in a particular phosphor is generally independent of the type of excitation.

The relationship of the absorbing and emitting centers further categorizes luminescence. If the two centers are apart, the excitation must be transferred by movement of charge (photoconduction) or through interacting fields (sensitized luminescence). When the center that absorbs also emits, one has localized luminescence, which is further divided into host-activated (a luminescent center at every lattice site) and impurity-activated (a small concentration of dopant serves as centers) luminescence. This study involves only impurity-activated luminescence.

In addition to their scientific value in understanding the electronic structure of materials, luminescent phenomena have found a variety of commercial applications. Fluorescent lamps, TV and CRT screens, x-ray detectors, and luminescent paints and dyes require efficient phosphors of the appropriate color. More recently, the growth of lasers and electro-optics

has added stimulus to the study of luminescence, particularly studies of kinetics, on which the device efficiency depends.

Overviews of the field of luminescence can be found in the books by Leverenz [12], Goldberg [13], and Curie [14]. The prime review article on inorganic phosphors remains that of Klick and Schulman [15].

2. Theory of Optical Processes

2.1 Atomic and Molecular Transitions

A comprehensive treatment of the theory of transition probabilities is required in order to understand the limitations of the final equations. Much of the information in this section and the next is taken from the review articles of Fowler [16] and Dexter [17]. Here we review atomic fluorescence, with emphasis on equations that must be revised when the atom is placed in a medium.

Atomic spectroscopy rests on the Einstein coefficients, which can be derived from classical black body theory or from quantum electrodynamics. Given an upper level 1 and a lower level 0 of energy splitting $(E_1 - E_0)$, the coefficient for induced transition (absorption or emission) is

$$B_{01} = B_{10} = (8\pi^3 e^2/3h^2)|M_{10}|^2 \quad , \tag{1}$$

where the electric dipole matrix element is

$$M_{10} = \sum_s \int \psi_1^* M_s \psi_0 dV \quad . \tag{2}$$

The sum in Eq. (1) is over all electrons, and the integral of the atomic wave functions ψ_1 and ψ_0 is over all electronic coordinates.

Once the radiation is absorbed, the atom may be induced to emit according to Eq. (1), or it may spontaneously emit at a rate given by the

coefficient

$$A_{10} = 1/\tau = (64\pi^4 e^2/3c^3h^4)(E_1 - E_0)^3|M_{10}|^2 \quad . \qquad (3)$$

The steady state intensity I of the emission is proportional to A_{10}, and thus inversely related to the exponential lifetime τ. Lifetimes are on the order of a nanosecond (nsec), which means that line widths are about a millionth of the peak energy (by the uncertainty principle). The natural linewidth depends on the lifetime of both initial and final levels; the halfwidth HW $\propto 1/\tau_1 + 1/\tau_0$. Thus a weak line can be broad if the final state is short-lived [18]. In atomic systems, absorption and spontaneous emission are related by

$$A_{10} = B_{01} \ (8\pi/c^3h^2) \ (E_1 - E_0)^3 \quad . \qquad (4)$$

The value of the matrix element in Eq. (2) is governed by selection rules. These are typically derived using LS coupling, which is rigorous only for light atoms. In heavy atoms, some of these rules are broken by spin-orbit coupling. The rules and how they are broken are as follows:

a) Only one electron is involved in a transition, with a change in its angular momentum ℓ by 1 ($\Delta\ell = \pm 1$). This is broken by configuration interaction, or mixing of states with the same quantum numbers and similar energies, but different electronic configurations.

b) The Laporte rule states that parity is conserved in the integral of Eq. (2). This means that the initial and final states must have opposite parity. Only the electric quadrupole or magnetic dipole interactions allow a transition between two even or two odd states.

c) Rules for the total orbital and spin angular momenta are $\Delta L = 0, \pm 1$ and $\Delta S = 0$. In addition, an $L = 0$ initial state cannot have an $L = 0$

final state. These rules are broken by spin-orbit coupling.

d) There are rules for the total angular momentum J and the eigenvalues of its z-component. These are never broken.

The situation in molecules is similar to that in atoms, but one must proceed more carefully, as do Birks and Munro [19]. The same analysis must be applied in the solid state. In analogy to Eq. (4), one can relate the emission lifetime to the absorption oscillator strength f by

$$1/\tau = (8\pi^2 e^2 \nu^2 / m_e c^3)\ f \quad , \tag{5}$$

but only under certain assumptions. If Eq. (5) is true, a typical oscillator strength of one leads to a lifetime of 4 nsec at 500 nanometers (nm), also typical.

The analysis begins with Eq. (2) and the Born-Oppenheimer approximation is made. In words, the electrons can adjust instantaneously to changes in nuclear positions, because the nuclei are heavier. Each atomic wavefunction is assumed to be separable into a product of an electronic function $\phi(rQ)$ and a vibrational function $\chi(Q)$, where r is an electronic coordinate and Q is a nuclear coordinate. The transition is from electronic state 0 to 1 and vibrational state 0 to n, in absorption. Then

$$B_{00,1n} \propto \left| \int \chi_{00}^{*}(Q)\ M_{01}(Q) \chi_{1n}(Q)\ dQ \right|^2 \quad , \tag{6}$$

where the electronic dependence is in M_{01} as

$$M_{01}(Q) = \int \phi_0^{*}(r,Q)\ M\ \phi_1(r,Q)\ dr \quad . \tag{7}$$

A key step is the Condon approximation, which assumes that the nuclei are stationary during the transition. Then the matrix element depends only on an average value of $Q = Q_0$, as

$$M_{01}(Q) \simeq M_{01}(Q_0) \quad . \tag{8}$$

Eq. (6) is now separable as

$$B_{00,1n} \propto |M_{01}(Q_0)|^2 \; |\int \chi_{00}^{*}(Q)\chi_{1n}(Q)\, dQ|^2 \quad , \tag{9}$$

where the second argument in Eq. (9) is called a Franck-Condon vibrational overlap factor. Since the transition can occur to any vibrational state, the total absorption probability is a sum over all final states n of Eq. (9). By closure,

$$B_{01} \propto |M_{01}(Q_0)|^2 \quad , \tag{10}$$

because the functions $\chi_{1n}(Q)$ form an orthonormal set.

The procedure in emission is similar, except that one must make the narrow peak assumption that

$$\sum_n (E_{1n} - E_{00})^3 \simeq (E_1 - E_0)^3 \quad . \tag{11}$$

In addition, the average value of Q in the RES will be displaced from Q_0 by q, so that

$$M_{10}(Q) \simeq M_{10}(Q_0 + q) \quad . \tag{12}$$

Then only if the matrix elements in ground and excited states are equal,

$$M_{01}(Q_0) = M_{10}(Q_0 + q) \quad , \tag{13}$$

will Eq. (5) be true. This occurs when the wave functions of the ground and excited states are identical.

In this laboratory, it was found [20] that the ground and excited harmonic oscillator wells formed by the medium around each center have the

same force constants for anthracene, phenanthrene, and other organic molecules, in a wide variety of media. This implies that Eq. (13) typically holds for molecules, and that Eq. (5) is valid. Where Eq. (5) has failed (e.g. higher diphenyl polyenes), there is evidence that the solute forms an excimer with the solvent [19]. In this case, the state emitted from is different from the state absorbed to, so that Eq. (13) could not be true.

Before applying Eq. (5), one must correct the data for non-radiative de-excitation. If a quenching phenomenon of lifetime τ_Q competes with the radiative process τ_{rad}, then the measured lifetime is

$$\tau_{meas}^{-1} = \tau_{rad}^{-1} + \tau_Q^{-1} \quad , \tag{14}$$

which is related to the quantum efficiency η by

$$\tau_{meas} = \eta\tau_{rad} \quad . \tag{15}$$

Knowing τ_{meas} and η, the experimental radiative lifetime τ_{rad} can be compared to that predicted from absorption by Eq. (5). When Eq. (5) holds, not only can the emission lifetime be predicted from the absorption oscillator strength, but the emission spectrum is the mirror image of the absorption spectrum. Good agreement is found [19] between prediction and experiment in anthracene, perylene, acridine, and a number of dyes. In other cases, agreement with Eq. (5) is still within 50% and the spectra are degraded mirror images.

In conclusion, for most molecules, as well as for atoms, absorption and emission measurements overlap, since the absorption spectrum and intensity determine the emission spectrum and lifetime. Additionally, the emission intensity is simply related to the lifetime. Selection rules for molecules are the same as for atoms, although they may be relaxed by lack

of spherical symmetry. Vibrational selection is determined by the Franck-Condon factors of Eq. (9).

2.2 Luminescence in Solids

In the condensed phase, one follows the same analysis to reach Eq. (5), and finds that absorption and emission are inverse processes. The assumptions made will now be evaluated for real systems to assess their applicability.

The Born-Oppenheimer or adiabatic approximation is considered quite good for visible transitions [17]. The criterion of validity is that the transition energy is much greater than the energy of a typical phonon; this certainly is true here.

Less well-established is the Condon approximation. Dexter [17] uses a particle-in-a-box model to show that if a peak HW is 10% of the peak energy, the Condon approximation neglects the enhancement of the transition probability on the low energy (LE) side, relative to that on the high energy (HE) side of the band, by about 10%. In a theoretical study of KCl:Tl, it was found [21] that this approximation is completely justified. The assumption that an optical band is much narrower than the value of its peak is similar to the Condon approximation, and this takes us past Eq. (11).

Similarly to Eq. (3), with the foregoing assumptions we can now give an expression for the lifetime of emission for a center in a medium of refractive index n:

$$A_{10} = \frac{1}{\tau} = \left[\frac{64e^2\pi^4}{9c^3h^4}\right] n\,(n^2 + 2)(h\nu_{em})^3\,|M_{10}(Q_0 + q)|^2 \quad , \qquad (16)$$

where $h\nu_{em}$ is the emission peak energy $(E_1 - E_0)$. One can go on to relate

the lifetime to the oscillator strength as in Eq. (5), but whereas Eq. (5) generally holds for atoms and molecules, it does not in the solid state [22].

For the F-center in alkali halides, the lifetime is ten times longer than that predicted from the strong oscillator strength. The excited state may be more diffuse than the ground state, so that the wave functions are different and Eq. (13) does not hold. In NaI:Cu, as in other Cu^+-doped alkali halides (to be discussed later), the lifetime is 10^4 times longer than predicted. It is thought that a symmetry difference between ground and excited states is responsible for the change in transition probability [16].

A theory was developed (see next section) and tested in this laboratory, which links the ground and excited states. In many organics, as previously mentioned, it works well. More often than not, however, for inorganics and especially the doped alkali halides [23], it is found that the state emitted from is quite different from the state absorbed to. Even if the excited well is not of different symmetry (as in NaI:Cu), at least its force constant is usually far from that of the ground state well (as in the F-center). One can seldom, then, use information about the ground state gathered from absorption to predict the parameters of luminescence in solids. No absorption data were taken for this thesis, and the absorption literature was not found to be very helpful in explaining the results of emission measurements.

Besides changing the lifetime through the refractive index and the nuclear displacement q, as in Eq. (16), the medium can revise the selection rules that govern the matrix element M_{10}. The symmetry of the luminescent center in the condensed phase is lower than the spherical symmetry of

the free atom. This leads to splitting of degeneracies and changes in selection rules (crystal field effects). The $\Delta\ell$ and parity rules may be seemingly violated by the interaction of the center with phonons during an optical transition (the vibronic interaction). For example, many relatively intense colors in crystals are due to $d^n \rightarrow d^n$ absorption in transition metal ions. The crystal field splits the degeneracy slightly, so that energy differences are in the visible region. In addition, since the initial and final states have the same parity, either the crystal field or lattice vibrations must mix in some other states for the absorption to be strong (e.g. mixing between d^n and $d^{n-1}p$). Electric dipole transitions are then allowed [24].

The rules concerning L and S can be broken by spin-orbit coupling, which depends on the gradient of the wave function at the nucleus. Since a wave function is affected by its surroundings, the degree to which a spin-flip transition is forbidden depends on the medium. For instance the Mn^{+2} transition, which is forbidden in vacuum, has a lifetime of .1 sec in ionic ZnF_2 and one millisecond (msec) in covalent ZnS.

Little remains of the principles of atomic fluorescence in the solid state. Selection rules are relaxed. The absorption oscillator strength is no longer simply related to the lifetime. The bandwidth has no relation to the lifetime, as we will shortly see.

However, by Eq. (16), the lifetime is still inversely proportional to the integrated emission intensity $I \propto A_{10} = 1/\tau$, for a simple system. For example, one finds that the intensity of the above vibronic transition rises with temperature, while the lifetime drops. (The radiative transition becomes more allowed due to the presence of more phonons.)

On the other hand, just as common is the opposite effect; the measured lifetime may be directly proportional to the intensity. The explanation is that the intrinsic radiative lifetime is constant, while a nonradiative process competes more or less successfully for the excitation. Such a situation is governed by Eq. (15), where the intensity (proportional to η) is directly proportional to the lifetime (τ_{meas}). The competing process most often encountered with inorganic phosphors is thermal quenching [25]. Here intensity and lifetime drop together as the temperature rises.

Another case was observed in this laboratory [26]. The emission intensity of ZnS:Cu,Al drops an order of magnitude in 50 kbar, while the lifetime is nearly constant. In this instance, both of the above processes may be occurring; the transition becomes more forbidden (tending to increase the lifetime), and is quenched (tending to decrease the lifetime). The two mechanisms are compensatory so that the lifetime is constant but the intensity must drop. The inescapable conclusion serves to justify this thesis: There is no substitute for measuring lifetimes.

2.3 Effect of Pressure on Luminescence

A useful model for explaining the luminescent spectra of solids is the configuration coordinate (CC) model. After making the Born-Oppenheimer approximation, one finds that the Schrödinger equation of the solid separates into electronic and nuclear parts. Since motion of the electrons is much faster than nuclear motion, the nuclei see a potential which involves the average positions of the electrons, but not their instantaneous positions. Expanding this potential about equilibrium leads to a quadratic function of Q, so that the nuclear motion can be described as a harmonic oscillator. The potential of the ground state E_g is

$$E_g(Q) = \sum_i (\omega_i Q_i)^2/2 \quad , \tag{17}$$

where the Q_i are nuclear coordinates. These are transformed to normal modes Q_i of the localized center, called interaction modes. Expansion of the electron-lattice (EL) interaction V about equilibrium Q_0 for the excited state e gives

$$E_e(Q) = \sum_i (\partial V/\partial Q_i)_0 \, Q_i + \sum_i (\omega_i' Q_i)^2/2 \quad . \tag{18}$$

A linear EL coupling results in a relative horizontal displacement q of the two harmonic wells, while a quadratic coupling leads to different force constants ω_i^2 and $(\omega_i')^2$.

Fig. 1 is a picture of these results, a diagram of a single configuration coordinate. Typically in the doped alkali halides, $\omega' < \omega$ and $q > 0$, as shown. Optical transitions occur vertically on the CC diagram, as the Franck-Condon factors of Eq. (9) are then maximized. A photon is absorbed (A to B), in less than 10^{-13} sec. Nuclear rearrangement (B to C) takes about 10^{-11} sec. The system remains in the RES (C), until emission (C to D). Further vibrational relaxation (D to A) leaves the center ready to absorb again.

A number of spectral properties are explained by the CC model. The Stokes' shift ($E_{AB} - E_{CD}$) is seen in all solids as a shift of the emission peak to an energy lower than that of the absorption peak. If the ground and excited wells have equal force constants, the spectrum has Gaussian peaks. However, if quadratic EL coupling exists, the peaks are skewed, or asymmetric [27,28]. The bandwidth is determined, not by the inverse lifetime as for an atomic transition, but by the thermal occupation of vibrational levels in the initial state, overlapped (vertically) with high

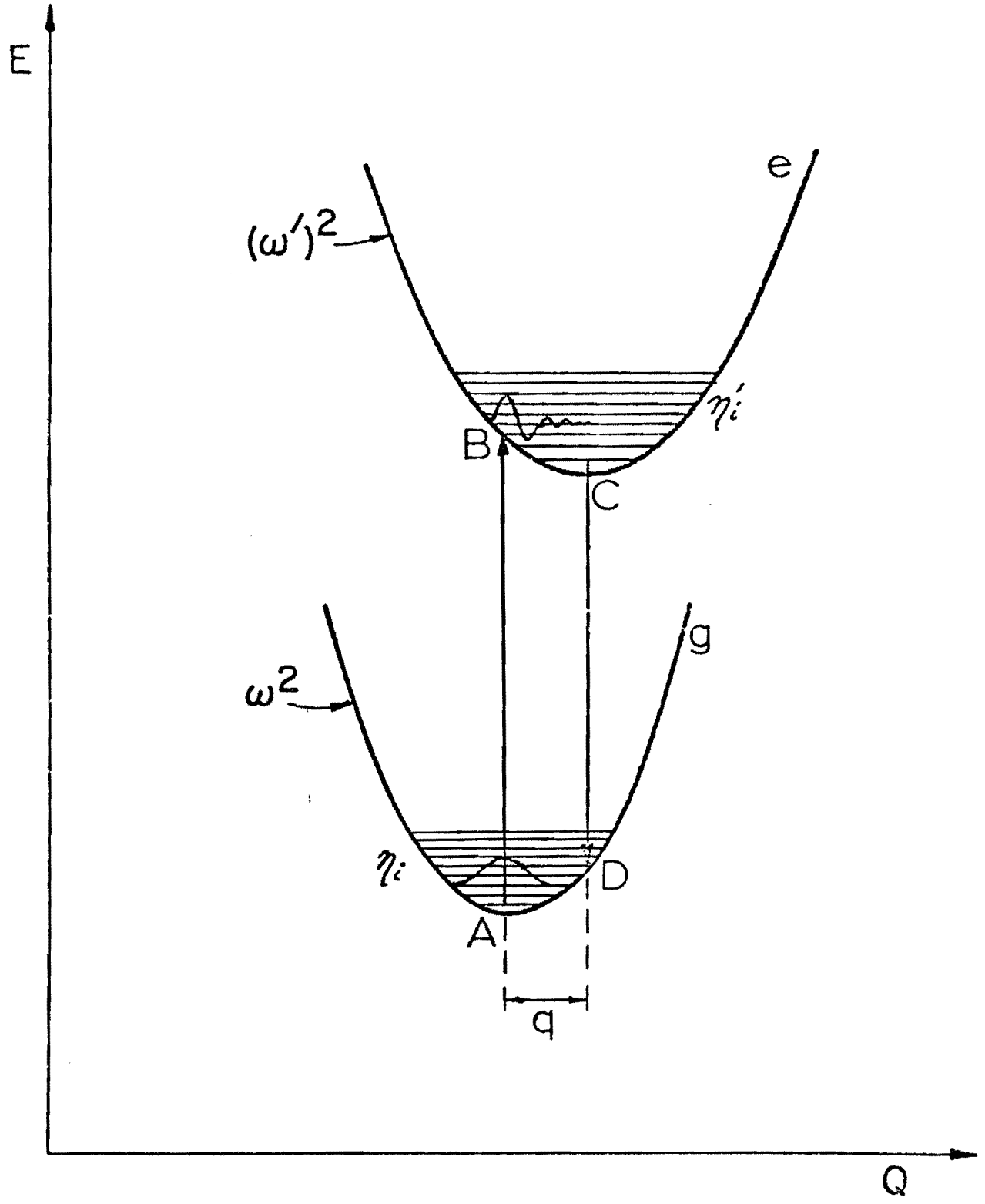

Fig. 1 Configuration Coordinate Diagram for a Localized Center

vibrational levels in the final state.

The CC model has been successfully employed to describe luminescent systems ranging from the F-center, where the Stokes' shift is 1/2 and the HW is 1/5 of the peak energy, to inner shell transitions of rare earth ions, in which the Stokes' shift and HW are about .1% of the peak energy. The single configuration coordinate of most importance is thought to be the A_{1g} totally symmetric breathing mode, in which the nearest neighbors expand or contract around the luminescent center. It is assumed that there is a single ground and excited state, both nondegenerate, which couple fairly weakly to the environment (well-localized). The single CC model breaks down when more than one coordinate is important, when electronic degeneracy occurs, or when the center is delocalized. These conditions frequently occur [23], so that one must be careful in employing the CC model.

A theory of the effect of pressure on the CC model has been developed [29,30]. To first approximation, pressure couples only to the A_{1g} volume mode Q of the localized center through a pV work term. Just as applying gravity to a mass on a spring changes the equilibrium position but not the force constant, so too will the linear pQ term change Q_0 but not ω^2. Eqs. (17) and (18) become

$$E_g(Q) = 1/2\ \omega^2 Q^2 + pQ \tag{19}$$

and

$$E_e(Q) = 1/2\ (\omega')^2\ (Q - q_0)^2 + pQ + E_0 \quad , \tag{20}$$

where E_0 and q_0 are the atmospheric values of E_{th} and q respectively. E_{th} is the energy difference and q the coordinate difference between the

excited and ground equilibria (well bottoms). The pressure dependence of E_{th} and q are given by [23]

$$E_{th} = E_0 + (q + q_0)\ p/2 \tag{21}$$

and

$$q = q_0 + p\ [\omega^{-2} - (\omega')^{-2}] \quad . \tag{22}$$

It can be seen that vertical (in energy) relative motion of the wells depends on horizontal well displacement. Horizontal (in volume) motion with pressure depends on unequal force constants (quadratic coupling).

The parameters q_0, E_0, ω^2, and $(\omega')^2$ completely determine the double-well system, even above atmospheric pressure. In turn, these parameters can be calculated from spectral measurements, such as the emission peak's energy, halfwidth, and skewness, and their change with pressure. With all the measurements one can make, the four well parameters are overdetermined. Then, sets of parameters calculated from different measurements can be compared for consistency [20]. More often, some of the measurements are more believable than others, and one uses these to calculate well parameters. The method used depends on the particular class of phosphors, so further discussion will be deferred to part 3.

Applying pressure to the CC model predicts peak shifts and changes in HW and skewness. How will lifetimes be affected? According to the simplest theory, very little. Eq. (16) gives the lifetime of an allowed transition in the CC model (neglecting radiationless paths). Horizontal well motion will not change the lifetime, since the Franck-Condon vibrational overlap factors were removed in Eq. (10). Even if one doesn't make the Condon approximation, an allowed transition probability will be only minutely

affected by pressure [21]. Vertical well motion (reflected by a shift in $h\nu_{em}$ of Eq. (16)) may change τ in a way predictable from steady state measurements, but this has not been shown. Compression of the medium causes an increase in the refractive index n, which will cause τ to drop, by Eq. (16). This refractive index effect has been tested successfully in organics [31], but the change in n with pressure is much smaller with inorganics (1% in 70 kbar for NaCl [32]).

The only other variable in Eq. (16) is the matrix element. Quite a few possible pressure effects are hidden here. The wave functions used in the matrix element must depend in some way on the well force constants. While we usually make the approximation that ω and ω' are independent of pressure, it has been shown in some cases that the approximation is invalid [20,33]. If the wells change shape under pressure, altering the matrix element, it seems that the resultant lifetime change would be difficult to predict.

The matrix element obeys the selection rules, and as these are changed by the medium, they can also have a pressure dependence. Spin-orbit coupling depends on the gradient of the wave function at the nucleus. The wave function can be pressure-dependent (as above), so that the spin-flip selection rule may be affected by pressure. Another effect is that pressure could cause a symmetry change (phase transition) that would alter the selection rules, and thus discontinuously change the lifetime. The most likely dependence on pressure of selection rules involves energy differences, which are more sensitive to pressure than wave functions and atomic positions. Configuration interaction depends on the inverse square of the splitting between the energy levels that are mixing. Pressure often shifts one level past another, so that large lifetime changes could be expected if these

levels are mixing.

A final effect of pressure on the matrix element involves the theory of forbidden transitions. This is the explanation given for the lifetime changes of the Cu^+- and Ag^+- doped alkali halides, so the discussion will be deferred until part 3.

To this point, Eq. (16) has been used to enumerate the effects of pressure on lifetimes. Eq. (16) is valid if the single CC model is an adequate description of the luminescent center. An increase in τ will invariably be accompanied by a decrease in the integrated intensity, which is proportional to A_{10}. When one speaks of the intrinsic radiative lifetime, it is given by Eq. (16).

In many cases, however, other processes compete for the excitation, and the measured lifetime is shorter than the intrinsic radiative lifetime. The ground well in Fig. 1 may cross the excited well, allowing nonradiative de-excitation. The energy barrier to de-excitation is altered by pressure, so the ease of thermal quenching is pressure-dependent. A quantum mechanical single configuration coordinate model has been found to predict successfully the lifetime as a function of pressure, using well parameters derived from steady state measurements [25]. The measured lifetime and intensity are related by Eq. (15), where the intrinsic radiative lifetime is generally constant with pressure. Other quenching processes that are more complicated than the single CC model allows also typically obey Eq. (15).

If radiative energy transfer is the competing process, the luminescent decay of the donor is no longer exponential. The decay curve can be fit by the appropriate function and the degree of energy transfer is found. Pressure has been shown to affect sensitized luminescence mainly through

the changing spectral overlap (shifting energy levels again) between donor emission and acceptor absorption [34]. Decay measurements were necessary to prove agreement with the Forster-Dexter theory.

It is obvious that with so many pressure-dependent factors affecting the lifetime, decay measurements could be difficult to interpret. In practice, however, it has been found that one effect typically dominates the others in a particular experiment. It is beneficial to have a large change in lifetime with pressure, so that the other effects are minor in comparison.

In addition to the previously mentioned decay measurements under high pressure [25,26,34], which employed the apparatus to be described here, there have been others. Long ago in this laboratory, phosphorescent lifetimes were measured to 50 kbar for three Mn^{+2}-activated oxygenated phosphors and four organic dyes [35]. Offen [31] has measured fluorescent and phosphorescent lifetimes in organic molecules; lifetimes invariable dropped 10 to 50% in 30 kbar.

There have also been many decay measurements at low pressures, in hydrostatic cells to ten kbar (e.g.[20]). Slow decays (τ > 1 sec) are easily measured with a steady state apparatus, and there have been high-pressure studies of slow time-dependent phenomena (e.g. [32]). To our knowledge, however, Gregg [35] and Offen [31] have done the only work on fast (τ < 1 sec) decays at high (> 10 kbar) pressure, and that mostly with organic phosphors. Thus, the apparatus to be described next in part 2 allowed the first comprehensive study of fast decays of inorganic phosphors under high pressure.

2. EXPERIMENTAL APPARATUS AND PROCEDURE

1. High Pressure Cells

The two solid state high pressure cells used in this study are modifications of the cells developed by Fitch, Slykhouse, and Drickamer [6]. For emission measurements, the optical windows are located 90° apart. They are filled with optical grade fused sodium chloride, which is transparent to radiation in the spectral region of interest. The sodium chloride also serves as the pressure-transmitting medium.

Cell I has a 1/8 inch piston and yields internal pressures up to 44 kbar. Cell II is a supported taper cell with 1/2 inch tapered pistons and is capable of generating quasi-hydrostatic pressures up to 150 kbar. Because of its greater light transmission, ease of loading, and accuracy of pressure, Cell I is preferred for use at pressures between 4 and 40 kbar, while Cell II is generally used for pressures between 15 and 150 kbar. These cells are shown in Fig. 2, and their specifications are given in Table 1. Pressure is applied to the cells by means of a hydraulic press with a 4-1/2 inch diameter ram. The external applied pressure is measured with Heise-Bourdon gauges.

The calibration of internal pressure versus external applied pressure has been determined by means of the R_1 ruby fluorescence shift [23]. This shift, determined by the National Bureau of Standards [4], is -.75 cm^{-1}/kbar to 195 kbar. For Cell I the calibration is linear in external applied pressure:

$$p_{int}(\text{kbar}) = .08\ p_{ext}(\text{psi}).$$

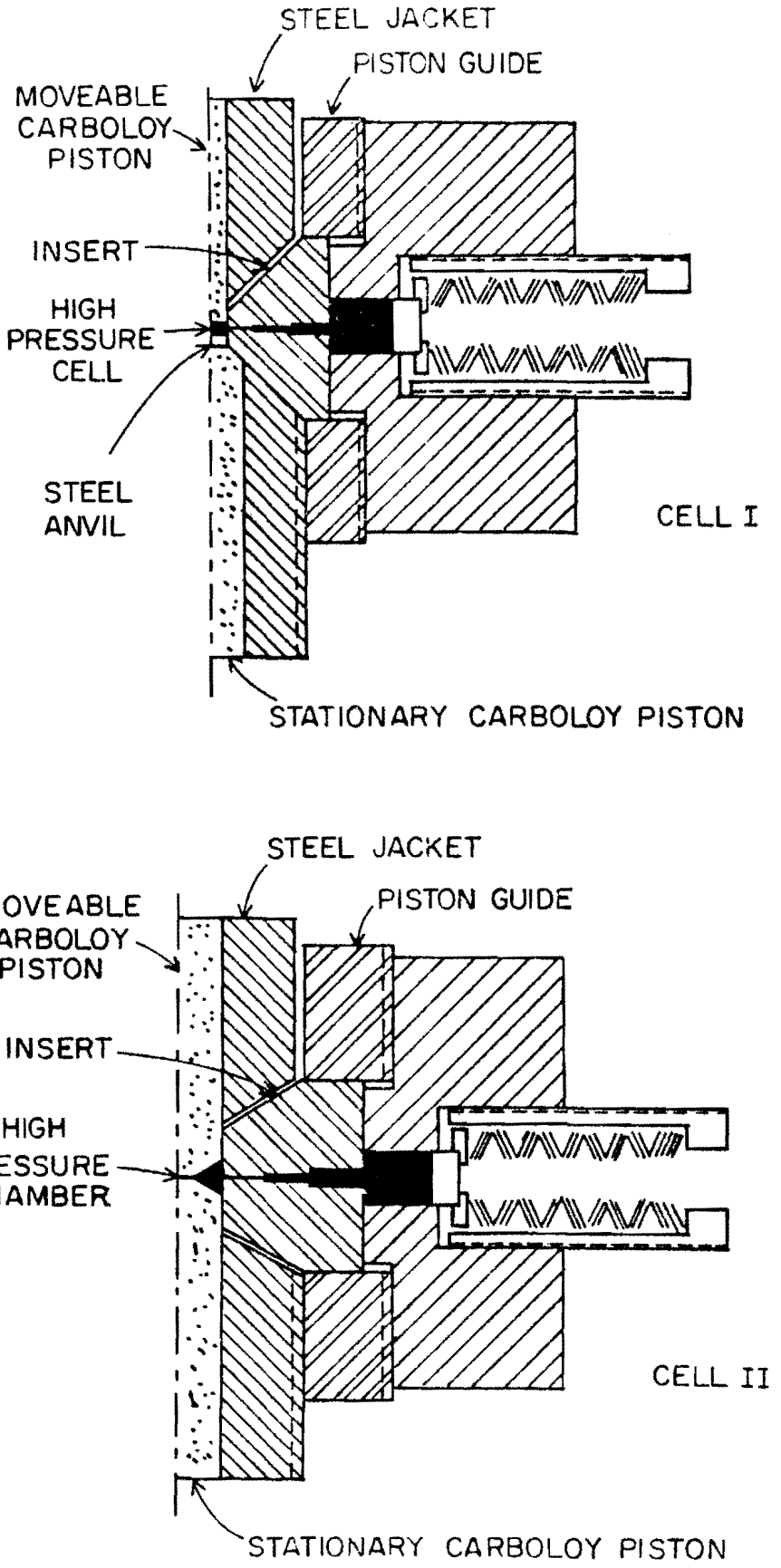

Fig. 2 High Pressure Optical Cells

Table 1

Specifications of High Pressure Optical Cells

	Cell I	Cell II
Piston Diameter	0.125"	0.500"
Piston Taper	0°	6°
Diameter of Flat	0.125"	0.093"
Jacket Diameter	3.31"	3.5"
Insert Diameter	1.000"	1.875"
Window Holes*		
(1) Length	0.125"	0.125"
Diameter	0.028"	0.037"
(2) Length	0.125"	0.188"
Diameter	0.046"	0.052"
(3) Length	0.188"	0.188"
Diameter	0.066"	0.082"
(4) Length	. . .	0.188"
Diameter	. . .	0.100"

*Holes are numbered starting from the inside of the cell

In Cell II, the internal pressure is a function of both external applied pressure and sample center thickness. The calibration is given in Table 2. Further details of the high pressure cells and their calibration are given by Drotning [23].

Note that the aperture of the long, narrow cone that makes up the cell window is less than 1 mm, and that the cone has an optical speed (base diameter/length) of about f/10. The salt that fills the cones, while transparent, can become cracked under pressure, which severely degrades its transmission. From these facts, it is obvious that the main problem in the design of optics is to get light into the cell and to collect light from the cell.

By means of certain modifications [25], Cells I and II can be taken to liquid nitrogen (LN_2) temperature. The main problem is to keep the windows in place at low temperatures. A static pressure of up to 1000 psi is applied uniformly across the outer surface of the windows by a uv-grade sapphire disc, pressed upon by Belleville spring washers (see Fig. 2). This pressure serves to keep the NaCl window material fused as it contracts during cooling and within the windows as it softens upon heating.

In order to maintain a constant low temperature while taking data, one regulates the flow of cold gaseous N_2 around the cell. The cell is placed in an insulating box, and LN_2 is boiled into the box. One follows an isobar to as low as 100°K, levelling the temperature at various points to take data. Since the pressure-transmitting medium is contracting, one must continually pump to keep the pressure constant. Temperature is monitored by a thermocouple close to the sample, and is estimated to be

Table 2

Pressure Calibration - High Pressure Optical Cell II

	Sample Center Thickness (.001")								
P_{ext}(psi)	3.5	4	5	6	7	8	9	10	11
1000	30.5	27.5	22.5	19	16	14	12	11	10
2000	52	49	43	37.5	32	28	24.5	22	20
3000	74	69.5	61	54	48	42.5	37	32.5	29
4000	95	90.5	82	73	64.7	56.3	49	42.5	36
5000	110	105.5	97.5	88	77	68	59.2	52	45
6000	122	118	109.5	99.5	90	80	71.5	63.3	55.5
7000	138	134	123	111.5	101	91	81	71.5	63
8000	146.5	142.5	133	123	112	100.5	89.5	79	69.5
9000	155	151	141.5	131.5	121.5	110.5	99	87.5	77
10000	162.5	159.5	151	142	131	120	108	96	84.5

Internal pressures in kbars

within a degree of the true sample temperature. The cell is resistively heated to room temperature (RT) before the pressure is increased to take another isobar. In low temperature (LT) and RT work, the pressure is always increased while taking data, except in recycling pressure at the end of the run to check reversibility.

2. Sample Preparation and Cell Loading

Crystals used in this study were prepared in this laboratory (except for the CsI:Tl sample, which was purchased from the Crystal Growth Laboratory of the Dept. of Physics, University of Utah). The methods used were those of Drotning [23] and Bieg [36]. One to two grams of Harshaw optical grade alkali halide crystal were placed in a quartz ampoule with a dopant. For Cu^+ or Ag^+ doping, .05 mole % of reagent grade monovalent impurity halide was used; for Tl^+ or In^+, .01% was used. Chlorides were used for doping alkali chlorides and bromides; iodides for doping alkali iodides.

The ampoule was evacuated, sealed, and placed in a furnace at about 30°C above the melting point of the host. After five minutes of melting, the furnace was shut off and allowed to cool. The ampoule was broken open to produce samples of sufficient size to fit in the pressure cell and pure enough such that no extraneous peaks were observable.

Annealing was necessary for the Cu^+ and Ag^+ samples, since they tend to form dimers which absorb and emit at lower energy than the individual centers. A few crystals were placed in a sealed, evacuated ampoule at 500°C for 3/4 hour. The ampoule was then quenched in ice water, freezing

the impurities in nonaggregated sites. Bieg found that this procedure left the emission spectrum stable for several hours after quenching. Lifetimes were taken within five hours of quenching.

The annealing procedure was not wholly satisfactory. As the crystals were in vacuum, heat transfer to the ice water at the moment of quenching was slow. It was suggested that filling the ampoule with dry nitrogen would improve heat transfer, but this was not tried. Also, the impurities were apparently quite volatile, since the Cu^+- and Ag^+- doped crystals lost emission intensity over a period of months and during annealing. A few times, when Ag^+-doped crystals were found to no longer emit after annealing, the unannealed sample was used in the run. No differences were seen in lifetime versus pressure between annealed and unannealed samples.

Chunks of the sample crystal were cleaved to an appropriate size, depending on the particular pressure cell being used. For Cell I, the sample crystal was a slab approximately 1/8 x 1/8 x .03 inches. A cylindrical block of optical grade sodium chloride was cleaved to make two half-cylinders. The face of one of these cylinder halves was then carved away, such that when the sample slab was placed between the cylinder halves, the front face of the sample lay approximately on a circular diameter. This is illustrated in Fig. 3. This cylinder sandwich was placed in the cell so that the entrance and exit beams intercepted the front plane of the sample at 45° angles. The assembly was then press-fused to about 4 kbar with the top piston in place. The single crystals that made up the sandwich had now been crushed and fused clear. A top ring was fused into place at about 8 kbar, and the cell was ready to run.

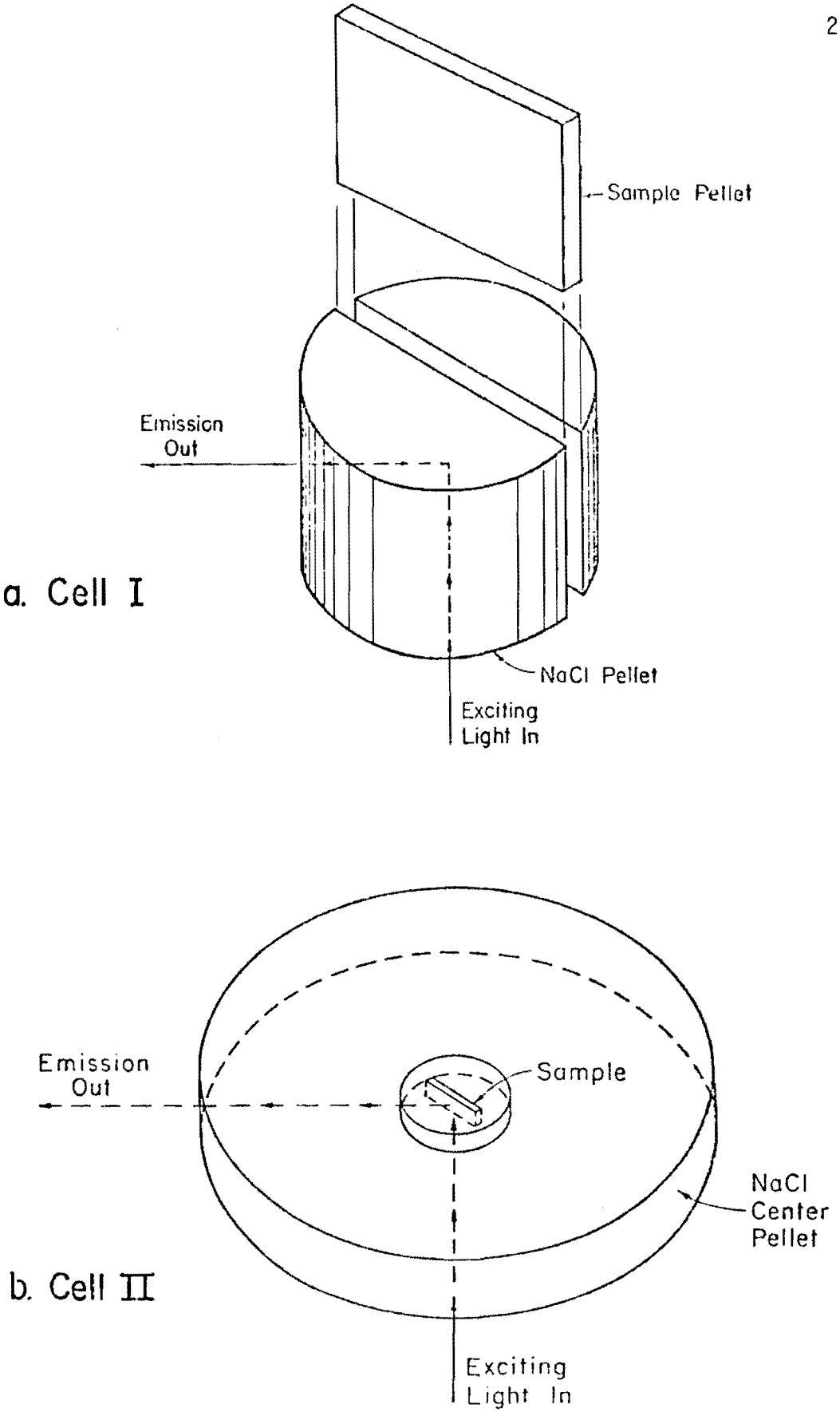

Fig. 3 High Pressure Cell Loading

Cell II was loaded somewhat differently, since the internal pressure depends on the pellet center thickness as well as the applied pressure. Initially, therefore, the length across the pistons with the cell empty was measured with a micrometer. A sodium chloride pellet was carved about 1/2 inch in diameter and of a weight necessary to give the desired center thickness. In most cases, the maximum thickness of .007 to .009 inches was desired, since having a lot of light was more important than attaining a very high pressure. A pellet of about .24 gram was satisfactory. The pellet was then pressed into the cell to 2500 psi with a flat-faced upper piston, an upper retaining ring added, and finally repressed with the tapered upper piston to 3000 psi. A small slot, oriented at 45° to the cell windows, was then carved in the pellet across the center flat and the sample crystal inserted, as in Fig. 3. Finally, the pellet and sample were repressed to 3000 psi, and the center thickness was measured. In addition, the center thickness was measured after completion of a run as a check for salt extrusion.

3. Emission Spectra

A schematic diagram of the steady state emission apparatus is shown in Fig. 4. It allows spectral measurements in the range 220 nm to 1500 nm, from the near uv to the near ir.

Three lamps are available for excitation: 150 W Xe, 200 W Hg, and 200 W Xe-Hg. Choice of lamp depended on the excitation spectrum of the phosphor. The double 1/4 m monochromator was fitted with a grating blazed at 300 nm. Slits as large as possible were used, giving a bandpass of 1.6 nm, which is sufficient to pass Hg lines.

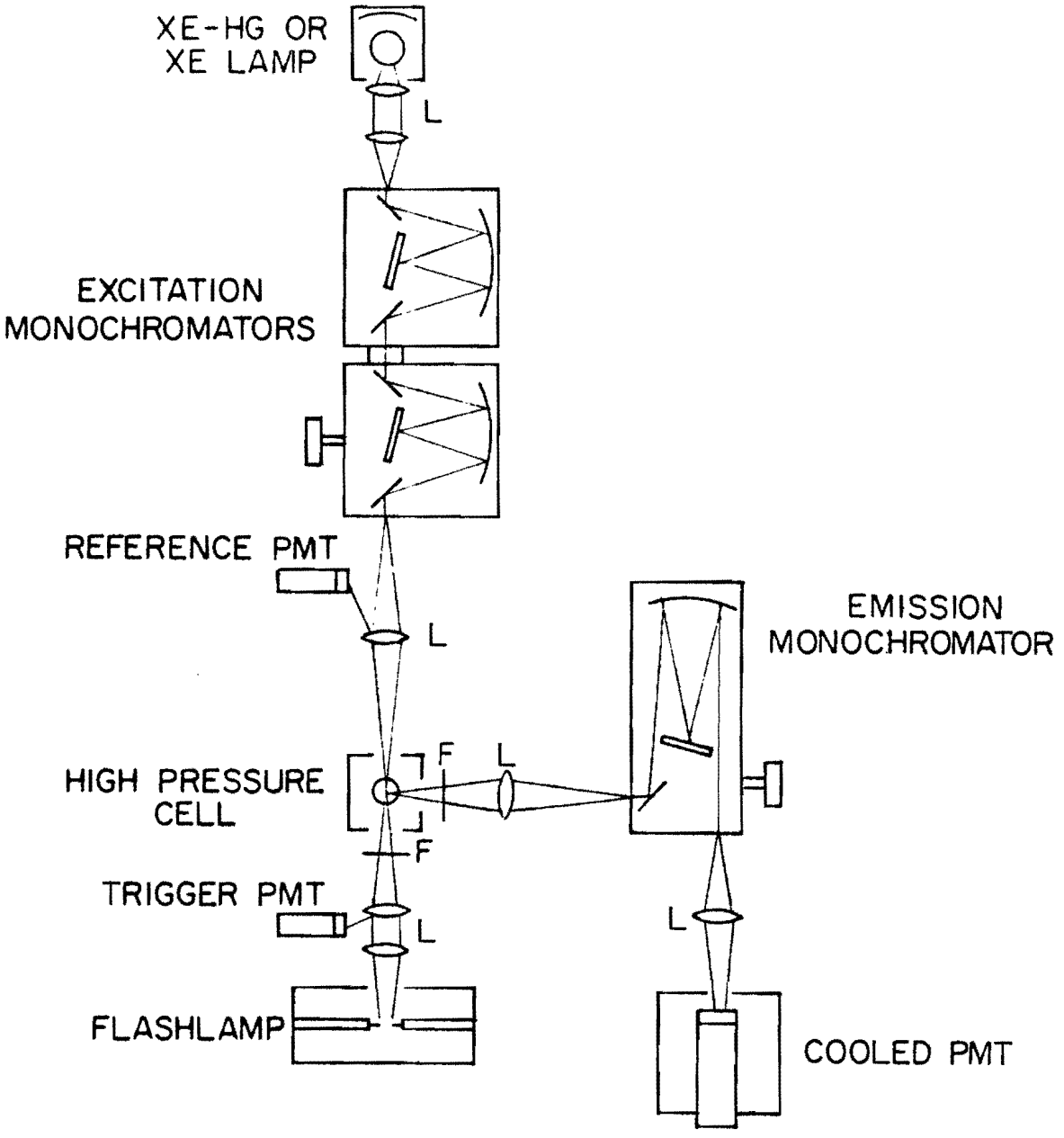

Fig. 4 Emission Spectrometer Block Diagram

The exciting light is focussed on the sample, and the emitted light is collected at 90°. Frequently, a cutoff filter was used to block reflected exciting light, which might pass in second order to obscure the emission spectrum. The Bausch and Lomb 1/2 m monochromator was fitted with a grating blazed at 300 nm for near uv emissions, or one blazed at 500 nm for visible emissions. Slits were set so that sufficient resolution was obtained.

To detect emission, an EMI 9558 QA photomultiplier (PM) was always used at -1200 volts. The PM was cooled to dry ice temperature (-70°C) in a Products for Research, Inc. TE-200-RF housing that is shielded from magnetic and radio frequency fields. Products for Research, Inc. supplies a dynode chain that is suitable for digital and analog signal processing. The analog processing involves DC amplification of PM currents on the order of nanoamps to microamps. A DVM reads the amplifier voltage output. At an early point in the work that leads to this thesis, a digital system was acquired, and most of the spectra discussed here were taken by the photon counting (digital) method [37-40].

To count photons, the PM output is hooked through a 1/2' cable to an Ortec 9301 pulse preamplifier that has a gain of ten and an input impedance of 50Ω. The photon-generated pulses are sent down a 10' cable to an Ortec 9302 amplifier/discriminator that has a gain of twenty. The discriminator selects pulses to be counted and shapes them. An Ortec 9315 photon counter counts the pulses during a specified gate time, and the result is displayed for a set period.

The advantages of the digital system over the analog one are a better discrimination against noise, equal weighting of photons, and ease of

operation. There are no disadvantages, since the maximum current that the DC amplifier can handle is nearly equivalent to the maximum count rate (1 MHz) for the digital system. Appendix A includes details on the photon counting equipment.

A possible cause of error in taking spectra is fluctuation of the lamp. To correct for this, the emission signal can be divided by the signal from a reference PM (EMI 9529 B) that monitors the exciting light. In the analog system, the DVM ratios the signal and reference amplifier outputs. In the digital system, the reference PM is hooked to a preamp and a discriminator, and the photon counter ratios the signal and reference count rates. It was found that the ratio mode is not very helpful, and no spectra were taken in this mode. Ratioing would not help if the excitation fluctuations were due more to arc wander than to brightness change. (The reference PM monitors the output of the whole arc, not just the 10% segment that enters the cell.) However, a well known remedy for arc wander (setting a magnetic stirrer by the lamp) did not reduce measured fluctuations.

Data points (intensity vs. wavelength) were taken at sufficiently fine wavelength intervals to achieve the desired resolution. Points were entered into program SKEW, which corrects the spectrum and fits one or two Gaussians with skew to the data. A plot (of relative number of quanta per unit time per energy interval versus energy) and its parameters are output for examination.

4. Decay Apparatus

A block diagram of the decay apparatus is shown in Fig. 5. It was grafted onto the steady state emission apparatus that has just been described, so that it uses the same press, emission monochromator, and signal PM. A separate setup is being constructed, that will offer improvements in transient measurements. Several aspects of its design are discussed in Appendix B (Laser Emission Rig).

4.1 Lamps

There are two ways of making transient luminescent measurements: phase and pulsed [41]. In the former, an excitation source is modulated, and the phase shift and demodulation of the emission are measured. The exponential lifetime or degree of nonexponentiality are extracted. In the pulsed method, the decaying emission is recorded after a flash excitation. The main advantage of pulsed excitation (which was used exclusively in this work) is that nonexponential decays yield information. Such decays are often found, and examples that have been studied in this laboratory are the donor decay in sensitized luminescence [34] and the sum of two exponentials, to be discussed in Part 4.

A third type of excitation is the step function. It can be shown that after a steady state lamp is turned off, an exponential process decays with the same lifetime as after an infinitesimally short flash (delta function flash). However, nonexponential processes yield different decay curves. Since obtaining a fast and clean cutoff is difficult, the pulsed method is generally chosen.

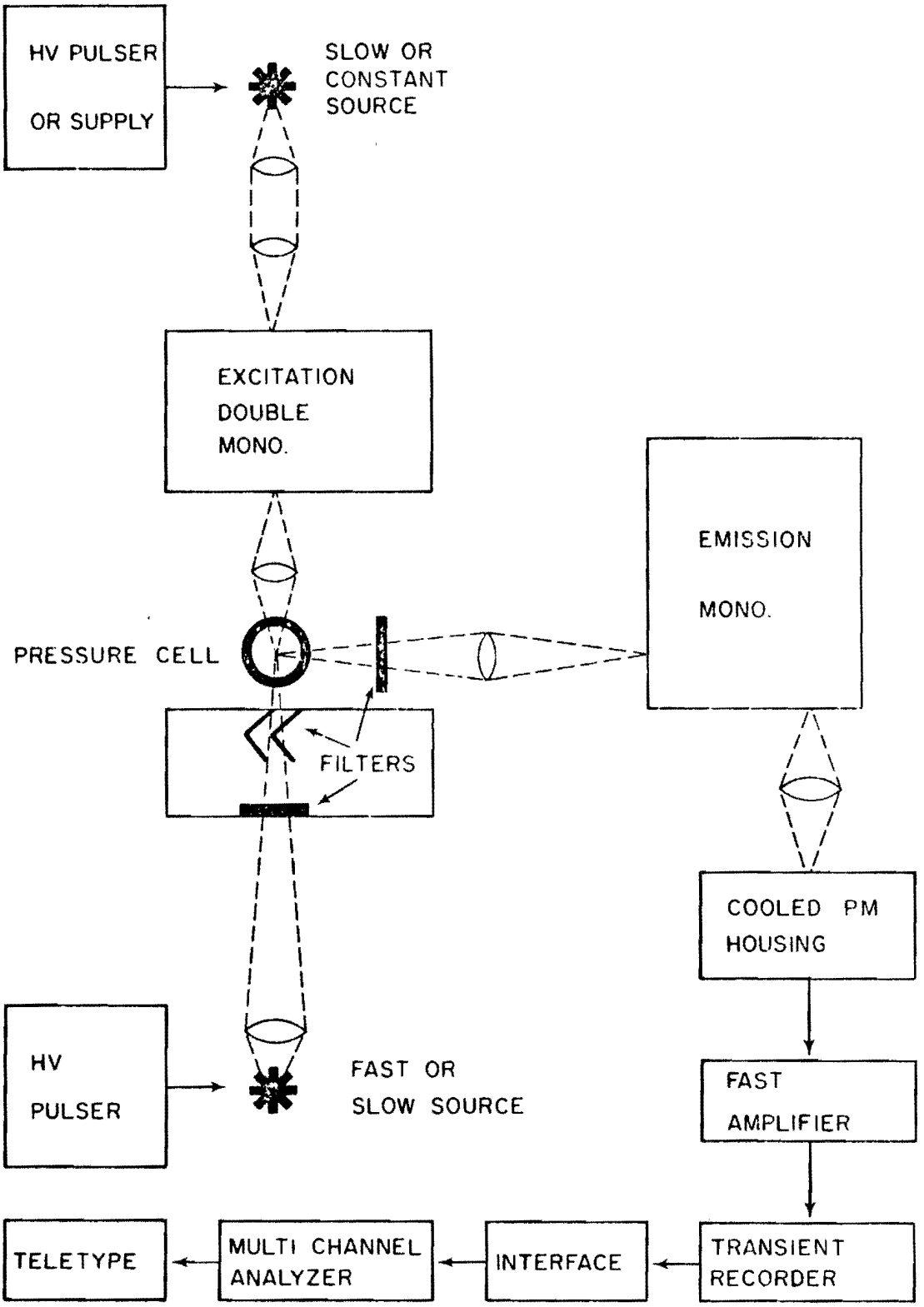

Fig. 5 Decay Apparatus Block Diagram

To obtain a pulse of light, followed by dead time in which the sample can emit undisturbed, one can either open a shutter (chopper or Kerr cell) from a steady state source, or flash the source. The latter is generally two orders of magnitude more efficient, for the following reason. The dead time must typically be 100 times longer than the light time, in order to approximate the ideal delta function flash. (Sufficiently nonideal flashes require deconvolution of the decay curve.) A flashing lamp can have a high peak power but a low average power, whereas in a steady state lamp, peak and average powers are equal. Since average power is thermally limited to the same degree for both lamps, the flashed lamp will have 100 times the power during the light pulse.

The flashed source can be a spark gap, a flashlamp, or a laser. Two sources were used in this work: a spark gap in nitrogen and a xenon flashlamp. Other sources, including lasers, have their advantages, which are discussed in Appendix B. The flashlamp is slower and brighter than the spark gap.

The flashlamp is an EG&G FX-12 flashtube filled with xenon to one atmosphere. It has a 1/4 inch gap and a quartz window. The operating parameters chosen were -1400 v with a 1 μF capacitor. This gives a flash whose electrical energy is one Joule. The flash is triggered externally by an EG&G TM-11A flashlamp trigger set at 20 KV, at a rate not faster than 2 Hz. High voltage (-1400 v) is provided by a Fluke 405B power supply through a 50 KΩ, 20 W resistor. Fig. 6 shows the circuit. The flashlamp wears out in about 10^4 flashes.

The spark gap is patterned after the light source of Zynger and Crouch [42]. It is in effect a coaxial capacitor that stores electrical energy

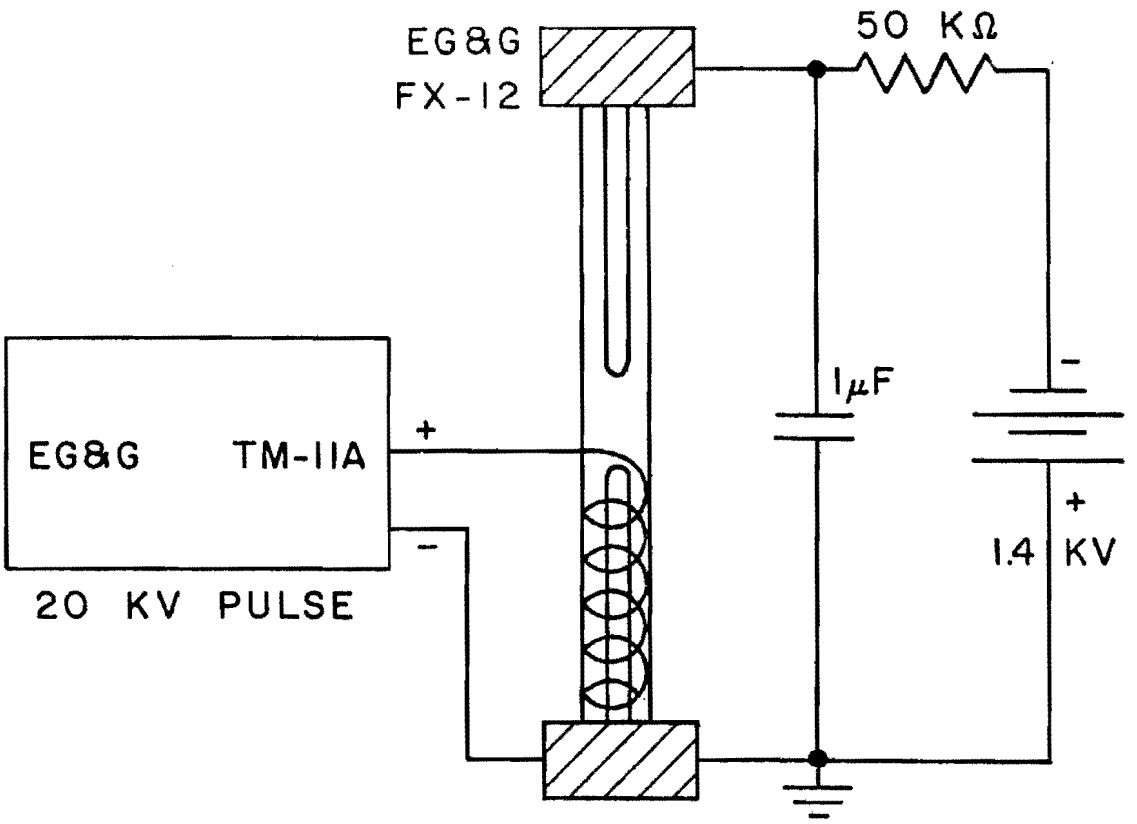

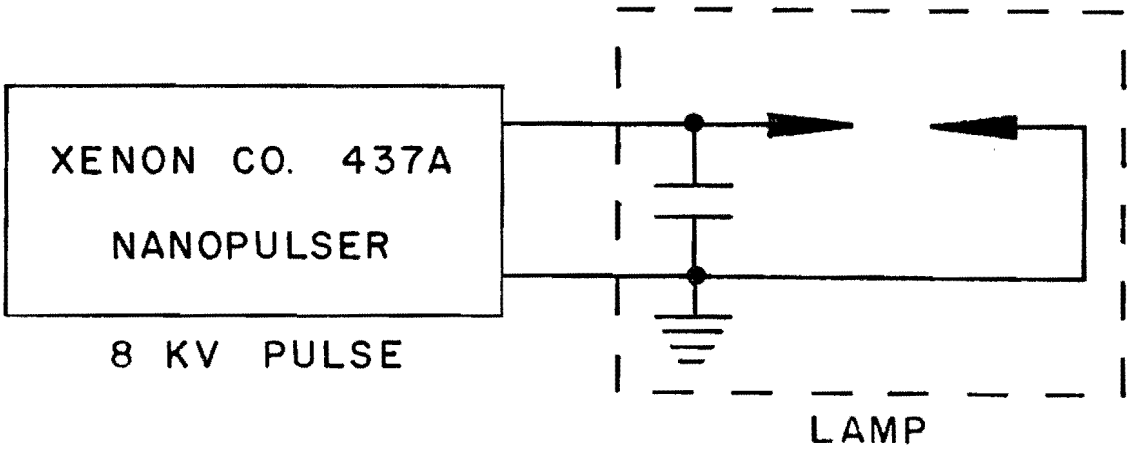

Fig. 6 Pulsed Lamp Circuit Diagrams
(Flashlamp Top and Spark Gap Bottom)

until breakdown occurs across the gap. The copper outer tube is separated from the aluminum inner rod by a .037 inch sheath of teflon. (Zynger and Crouch used a sheath one half as thick. We tried this and the teflon broke down. Doubling the thickness did not appreciably reduce the intensity and the teflon has not broken down. In addition, to reduce corona discharge, the teflon is coated with transformer oil. The brass rod is electrically connected to the grounded copper tube by a coating of Aquadag graphite around the lock rings.) A diagram of the light source is shown in Fig. 7. The copper tube is 16" long, with a 1.97" OD and a .83" ID. Centered in the tube is the spark gap, at 8" from each end.

Fig. 6 shows the spark gap circuit. A Xenon Corp. 437A Nanopulser charges up the coaxial capacitor with an 8 KV, 40 μsec pulse. When the voltage is reached at which gap breakdown occurs, a spark shorts the capacitor to ground. Breakdown voltage is a function of the arc length, which can be adjusted from 0 to 5 mm. The electrodes are of .020 inch tungsten rod ground to a point (30° included angle) on a diamond wheel. They are fixed in place by Allen head set screws, and then the arc length is varied by a screw adjustment. Electrode replacement is after about 5×10^5 flashes, when they become blunt. The Nanopulser pulse rate is 0 to 60 Hz, but by using an external oscillator, the rate can be increased to 160 Hz. A further increase in the rate would be likely after properly adjusting the internal LC circuit.

In Fig. 8 is a time profile of the flashlamp's flash. The HW is about 2 μsec, but there is a substantial tail extending to 8 μsec. This lamp has therefore not been used to measure lifetimes shorter than 20 μsec.

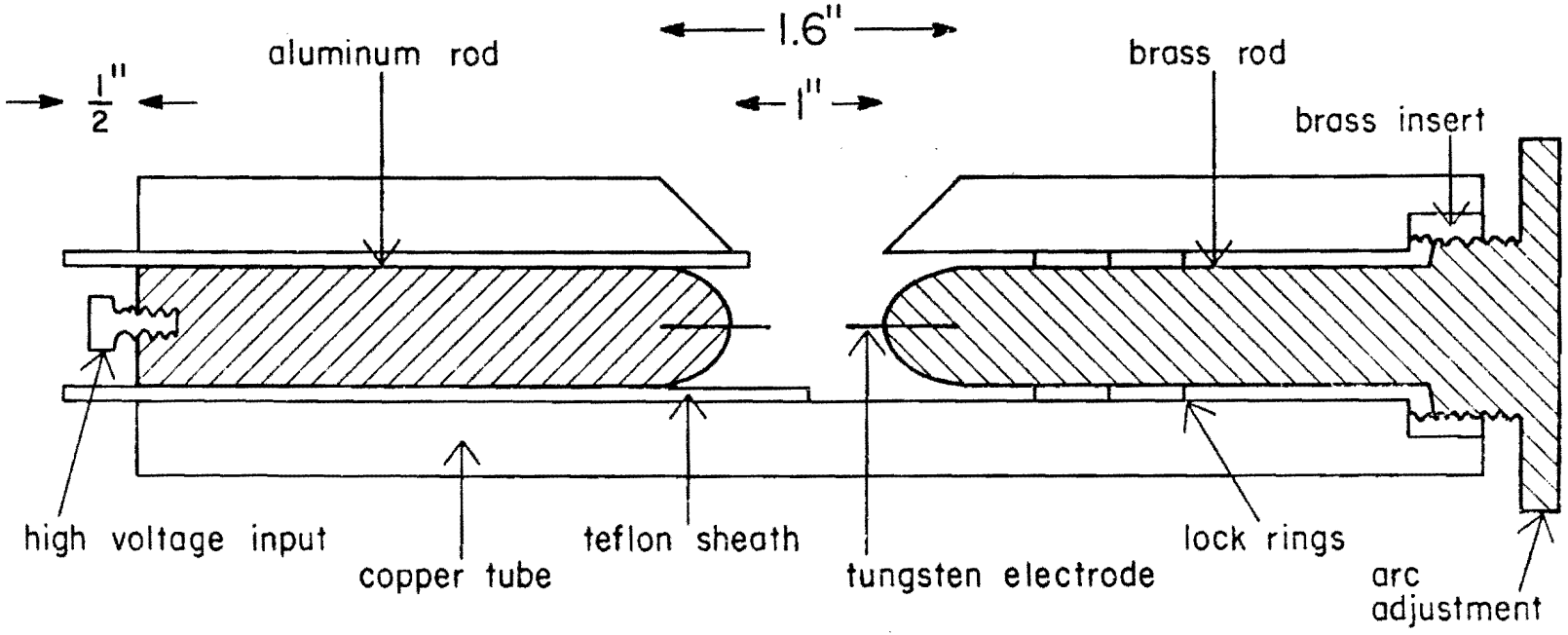

Fig. 7 Cross Section of the Spark Gap

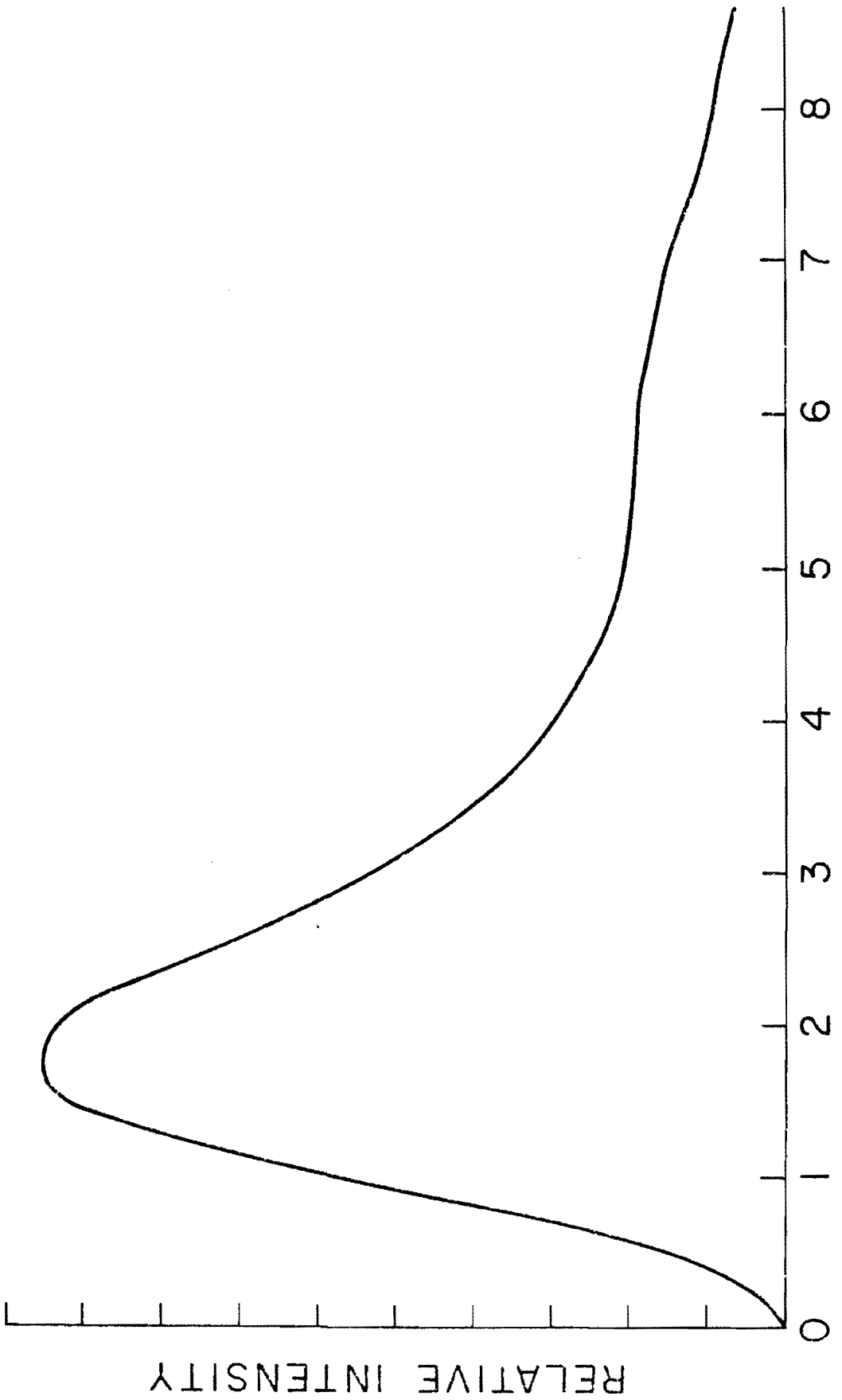

Fig. 8 Time Profile of Flashlamp Light Pulse

Fig. 9 shows the spark gap's time profile. Its HW is about 10 nsec, but there is a tail. Calculations show that 61% of the light has appeared within 35 nsec of the start, 86% within 70 nsec, 94% within 105 nsec, and 98% within 140 nsec. Therefore, decays with lifetimes below 100 nsec should not be measured with this lamp. Figs. 8 and 9 are smoothed curves from data taken by the averaging methods to be described. While they were taken at a specific wavelength, the time profile is not expected to change with wavelength.

The lamp intensity does, of course, change with wavelength. Fig. 10 gives corrected lamp spectra (taken by averaging the peak value of several flashes at each wavelength). Curve 1 is from the xenon flashlamp, and it is a typical xenon continuum, rather weak in the uv. Curve 2 is the spark gap spectrum using a 4.65 mm arc length. Curve 3 uses a 2.4 mm arc length. (Curves 2 and 3 are normalized at 250 nm, and the absolute intensity of curve 1 is orders of magnitude larger than that of the spark gap.) The spark gap spectrum is formed by broadened N_2 lines, mostly in the uv. A longer arc adds more flash in the visible. Nitrogen is forced into the well around the spark gap, in order to reduce ozone buildup and to have a pure N_2 spectrum. (In Fig. 10, however, the spark gap was in air.)

The lamp time profiles should be checked occasionally to see that they have not degraded for some reason. Another lamp problem that should be checked often is afterflashing of the spark gap. The afterflashes are small flashes 100 times less intense than the main flash, that occur at least 20 μsec and usually 150 μsec after the main flash. For slow decays (>20 μsec) this could be a problem, if the reflected flash is not completely blocked.

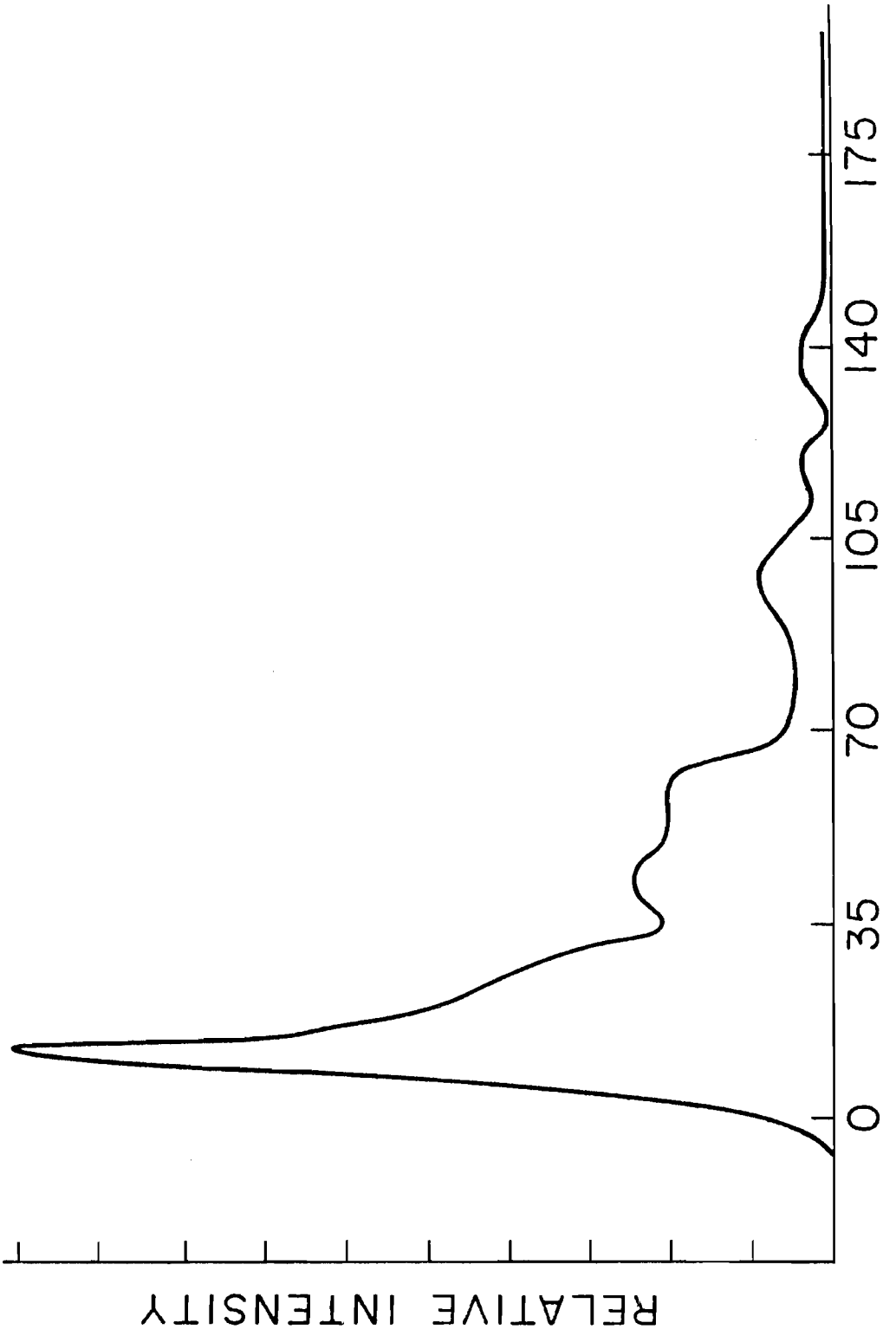

Fig. 9 Time Profile of Spark Gap Light Pulse

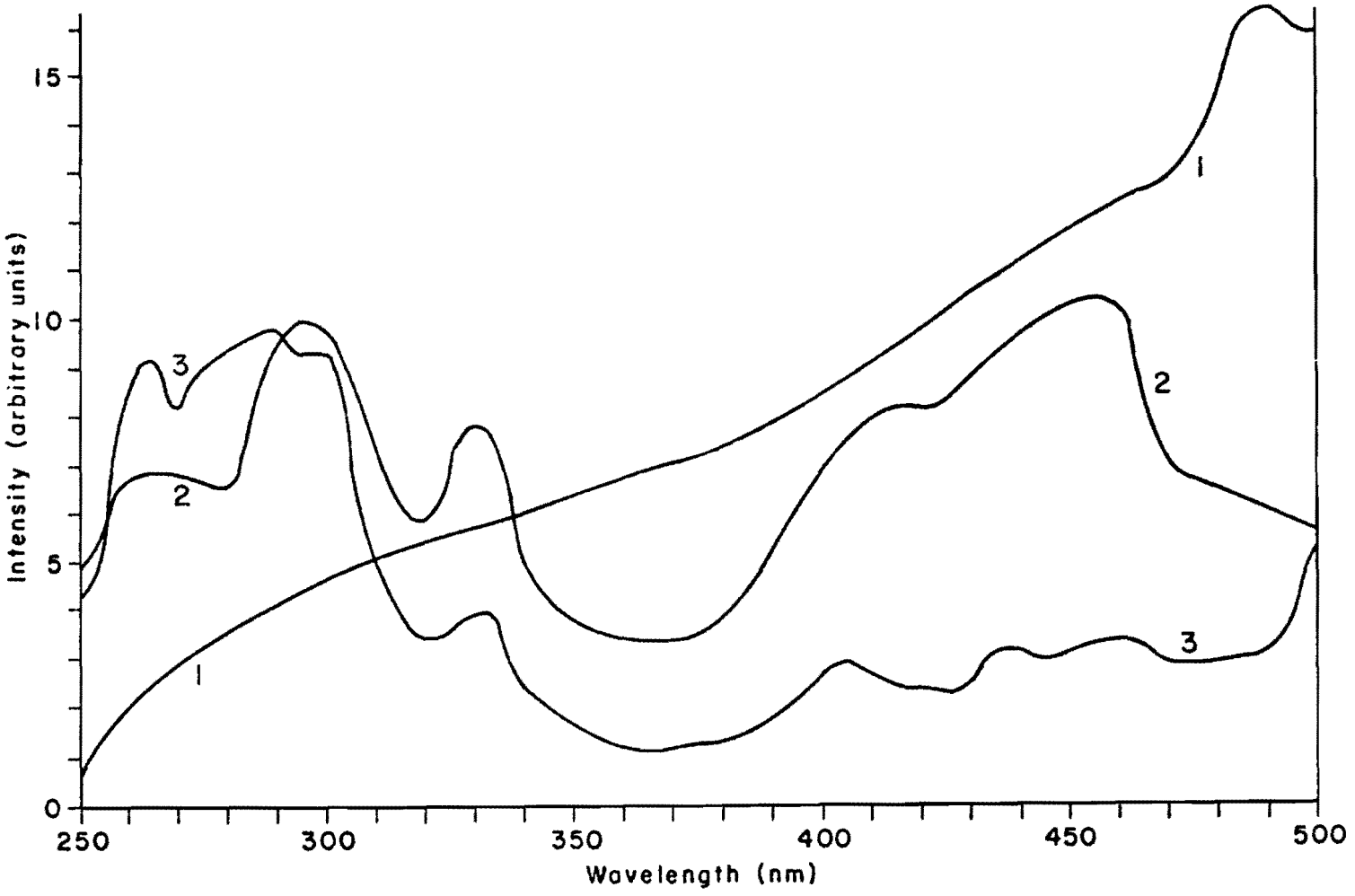

Fig. 10 Corrected Spectral Output of Pulsed Lamps: 1) Flashlamp; 2) Spark Gap with 4.65 mm Arc Length; 3) Spark Gap with 2.4 mm Arc Length

4.2 Optics

The flashlamp can be placed in the same location as the steady state lamps, behind the double monochromator. Electrical hookups have been built for this setup, but it was not used to gather the data in this thesis. For very precise selection of the exciting wavelength, the double monochromator is helpful, but the maximum bandpass is 1.6 nm, which cuts out most of the spectrum of Fig. 10. In addition, the optics are not optimized for maximum collection of light, due to the monochromator. The resulting flash is so weak that another setup, without monochromators, was used. The cell is rotated 90° (see Fig. 5), and a filter is employed to select the exciting wavelength. Enough light is then available to measure the lifetimes of even the weakest phosphors whose spectra we can record (e.g., those in Part 3). The setup with monochromator will not be discussed further.

Both lamps require the same optics to excite samples. Pressure cells I and II can be used, at RT and LT. The small liquid cell can also be used, though this has not been tried. Each lamp is enclosed in its aluminum box, which helps reduce radiation of radio frequency interference (RFI). A two inch Schoeffel f/1 quartz lens fits in front of the box close to the arc. The lens (and the flashlamp tube) should be cleaned with spectral grade toluene if contaminants accumulate. From Fig. 7, it can be seen that a one inch well has been drilled in the copper tube to expose the spark gap. The well was flared out to allow a cone of light from the flash to fill the two inch lens.

The optical design is determined by the slow f/10 speed of the cell; only a narrow cone of light can enter the cell. In addition, one wants to

collect the maximum amount of light, so the lens should be as near to the flash as possible while still converging the beam. The setup in Fig. 11A, then, would seem to be ideal: The lens is placed so that the point source is just beyond its focal length. Focussing of the source is far away, converging in a narrow cone.

One consideration counts against this design. The farther the cell is from the lens, the greater the image magnification. Since the arcs are wandering line (not point) sources, and the beam must be focussed through a 1 mm aperture in the cell, much of the light will be lost on magnification. Assuming a 5 mm stable arc length and a lossless lens, the fraction of light L that reaches the sample is the fraction collected times the fraction put into a narrow enough cone times the magnification loss times the ratio of aperture size to arc length. Designate the source to lens distance as s and lens to image as s'. The lens diameter is d and the cell speed is k. Then if s'<dk,

$$L = \frac{\pi d^2/4}{4\pi s^2} \times \left[\frac{s'}{kd}\right]^2 \times \frac{s}{s'} \times \frac{1\ \text{mm}}{5\ \text{mm}} = \frac{s'}{80sk^2} \quad .$$

If s'>dk, the second factor becomes one (no attenuation). Then $L = d^2/(80s's)$. A graph of L versus s' yields a maximum value for L of $d/(80sk)$ at $s' = dk$.

Hook [43] has drawn the cells in the optical path domain (correcting for the refractive index of NaCl). Depending on where the beam is focussed, values for k range from 6.5 to 10 for the two cells. (A value of 6.5 was used to design the apparatus, but $k \approx 10$ seems more likely now; k is the cell's optical speed or the length of the window cone divided by

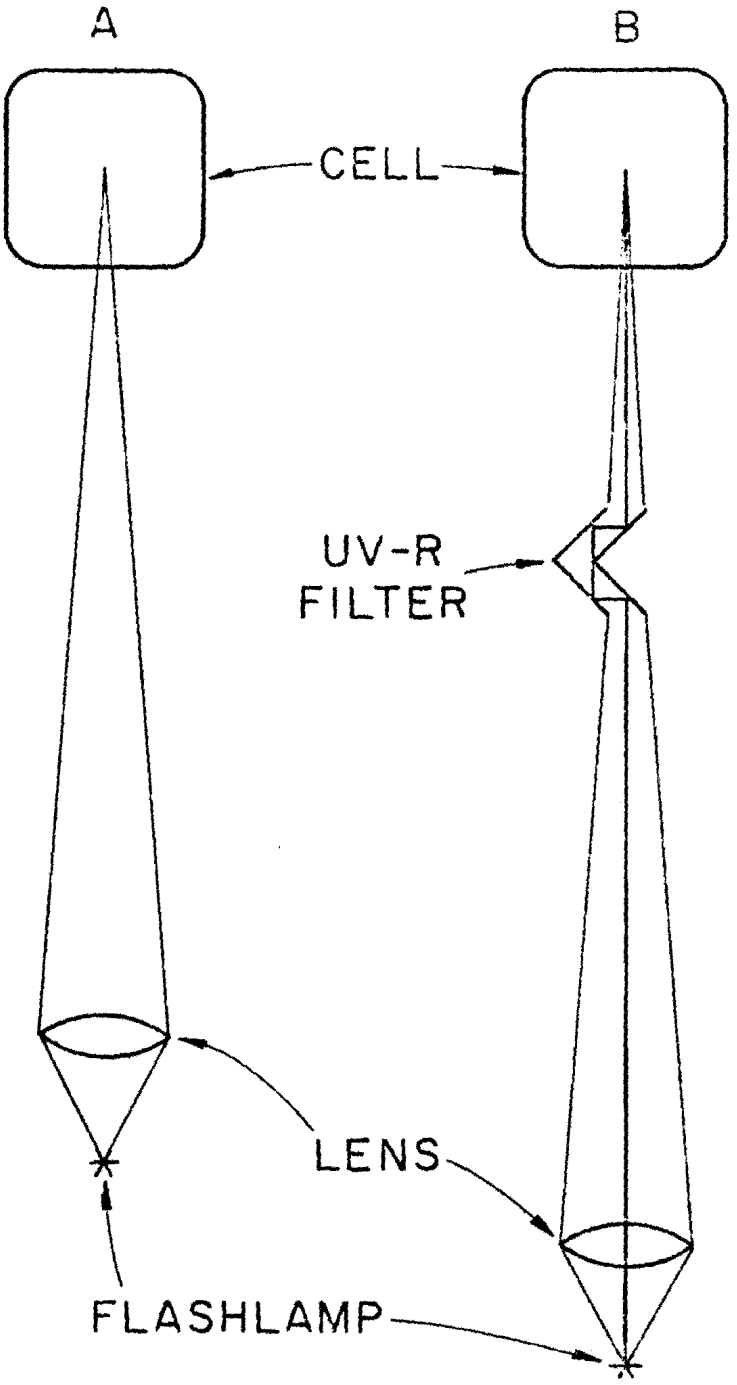

Fig. 11 Scale Drawing of Excitation Optics:
A) Without and B) With UV-R Filter

its base diameter.) The lens diameter d is 2" and s can be no less than the focal length, measured as 2.05" ± .1". Then at s' = dk = 13", L = .002. Only .2% of the flash enters the cell under the best conditions!

Such a performance is not impressive, but other optical designs are no better. Two lens or three lens (including field lens) systems are slightly worse. A cylindrical lens could focus the line source to a point, but this was not tried. Certainly what is needed is a linear beam--a laser. The possibilities and limitations of a laser rig are discussed in Appendix B.

Since the length of the spark gap is adjustable, what is the optimum setting? According to theory [42], the total gap intensity increases with the square of the arc length A. As A increases, less of the total intensity enters the cell, so the usable intensity should rise linearly with A. Fig. 12 shows the usable uv output versus arc length of the spark gap. The mesurement involved finding the emission intensity of $CdWO_4$ (excited at 250 nm) in cell I, under normal run conditions. There is a rise in intensity with A that is approximately linear. At small A, however, the intensity drops as A rises. (The abrupt drop in intensity at smallest A is probably due to misalignment of the minute source.) Since a long arc is easier to align and brighter, the recommended setting is A = 4 mm. For continuous high speed flashing, however, a 1-2 mm gap is used to avoid straining the equipment.

The theory [42] also predicts that the flash width rises linearly with A. This was not checked, so the time profile of Fig. 9 (where A = 1 mm) may be degraded by the use of longer arcs. A radiant power of 10^4 W was claimed [42] for the spark gap (probably over a spherical solid angle).

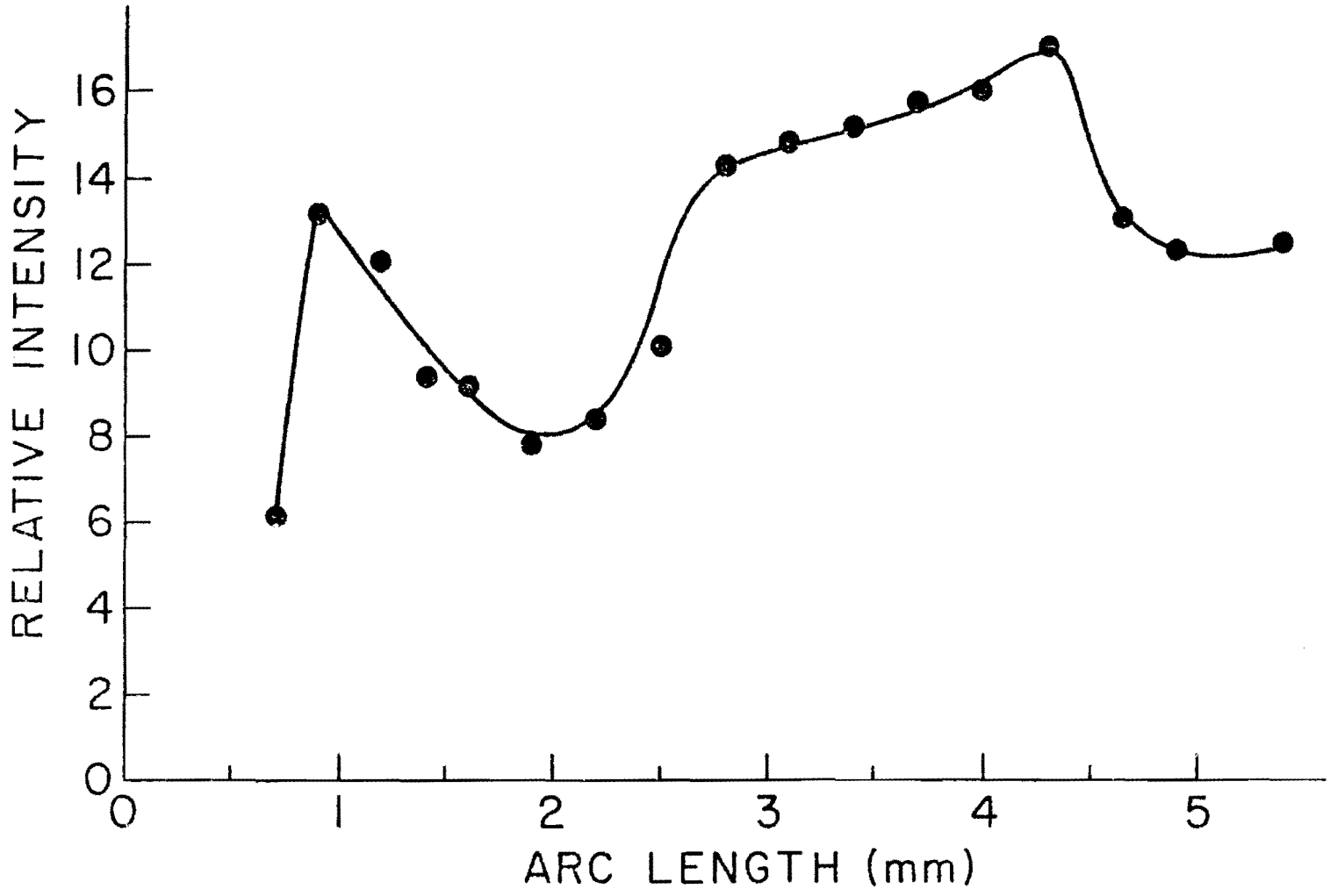

Fig. 12 Spark Gap Ultraviolet Intensity at Sample vs. Arc Length

This translates to 2×10^{-4} Joules of light, to be compared with one Joule of electrical energy for the flashlamp. Apparently a gain of 100 in speed produces a loss of 1000 in intensity. The rated power translates to 5×10^{14} photons per flash, which means that the spark gap excites the sample with 10^{12} photons.

Exciting-wavelength selection is by filter, since the entire excitation peak of a sample can be encompassed by the broad filter bandpass, with maximum throughput. (Peak transmission is typically >80%.) Schott and Corning uv-pass colored glass filters are available in the near uv. For deep-uv excitation, Schott UV-R interference reflectance filters are used, centered at four wavelengths: 220, 250, 280, and 310 nm. These have 40 nm halfwidths and excellent blocking at long wavelengths. As shown in Fig. 11B, light rays have to reflect inside the filter, but a converging input beam will produce a converging output beam. The UV-R filter simply acts as an extender of the optical path.

The filters must be far enough from the cell to be used for LT operation. They are mounted in a box that also contains a trigger (or reference) PM, which provides an initiate pulse when the lamp flashes. The trigger PM is separated from the lamp to avoid RFI. Stray reflection of light is adequate for the trigger pulse, and an iris (adjustable from 1 to 30 mm) sets the pulse voltage level. The RCA 1P28 was chosen because it is fast (2 nsec), inexpensive, and available. Fig. 13 shows the dynode chain (recommended [44] for high current pulses) that shapes the trigger pulse. Unmarked resistors are 100 KΩ and capacitors are .01 μF. Cathode voltage ranges from -600 v to -1000 v (-1250 v maximum) depending on the application.

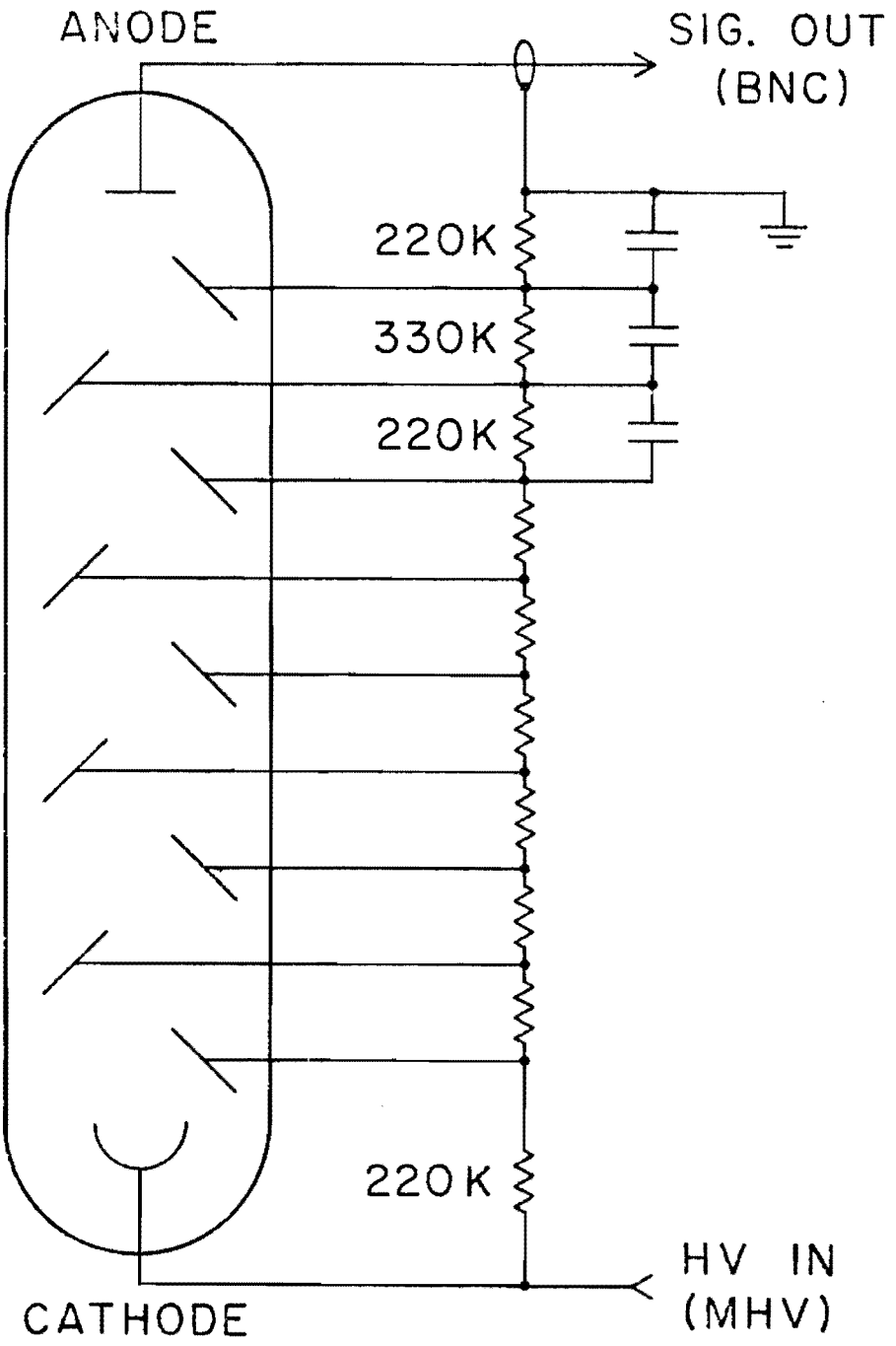

Fig. 13 Pulse Dynode Chain for RCA 1P28 Trigger Photomultiplier Tube. Unlabelled Resistors are 100 KΩ and Capacitors are .01 μF

The decay apparatus was constructed using the above optical calculations and the published measurements of the UV-R filter. On receiving the filter, it was found that the actual dimensions are different, but no effort was made to reconstruct the apparatus. Also, the positions of optical components that optimized sample illumination were slightly different from those calculated. In fact, the optimum source to lens distance s is less than the measured focal length, which would lead to a diverging beam! (Probably invalidity of the thin lens assumption leads to this paradox.) A careful re-optimization of the setup could be helpful. The designer of the laser emission rig (Appendix B) should be aware of the optical parameters given in Table 3, and allow for experimental adjustment of calculated design parameters.

4.3 Transient Digitization

Two instruments were built to detect decay curves. Both use the lamps, optics, pressure cells, and PM tubes already described. The PM outputs, however, are connected to different components. Transient digitization can measure lifetimes from 1 μsec to 5 sec. Single photon counting measures lifetimes from .1 μsec to 50 μsec. The two methods were overlapped frequently in the 1 to 5 μsec range for the study described in Part 4, and they always agreed within 20%. In this section the transient digitizer will be explained, and in the next section, single photon counting.

Fig. 5 shows a block diagram of the transient digitizer. Fig. 14 is a more detailed view of the electronics. If the phosphor is bright (case

Table 3

Measured Optical Design Parameters for the Decay Apparatus

Lens:	diameter = d = 2" focal length = f = 2.05" ± .1"
Pressure cells:	aperture ≃ 1mm speed = k ≃ 10
Flashlamp:	arc length = 6.4 mm (vertical) little arc wander
Spark gap:	arc length = 1-4 mm (horizontal) much arc wander
UV-R filters:	actual length = 40 mm optical path length = 72 mm front aperture = 15 mm back to sample distance = 133 mm
Optical path lengths (inches):	s = source to lens' optical center s'= lens' optical center to sample

	flashlamp	spark gap
Fig. 11A (no UV-R)	s = 1.91 s'= 13.35	1.85 13.25
Fig. 11B (UV-R in)	s = 1.75 s'= 18.76	1.90 18.46

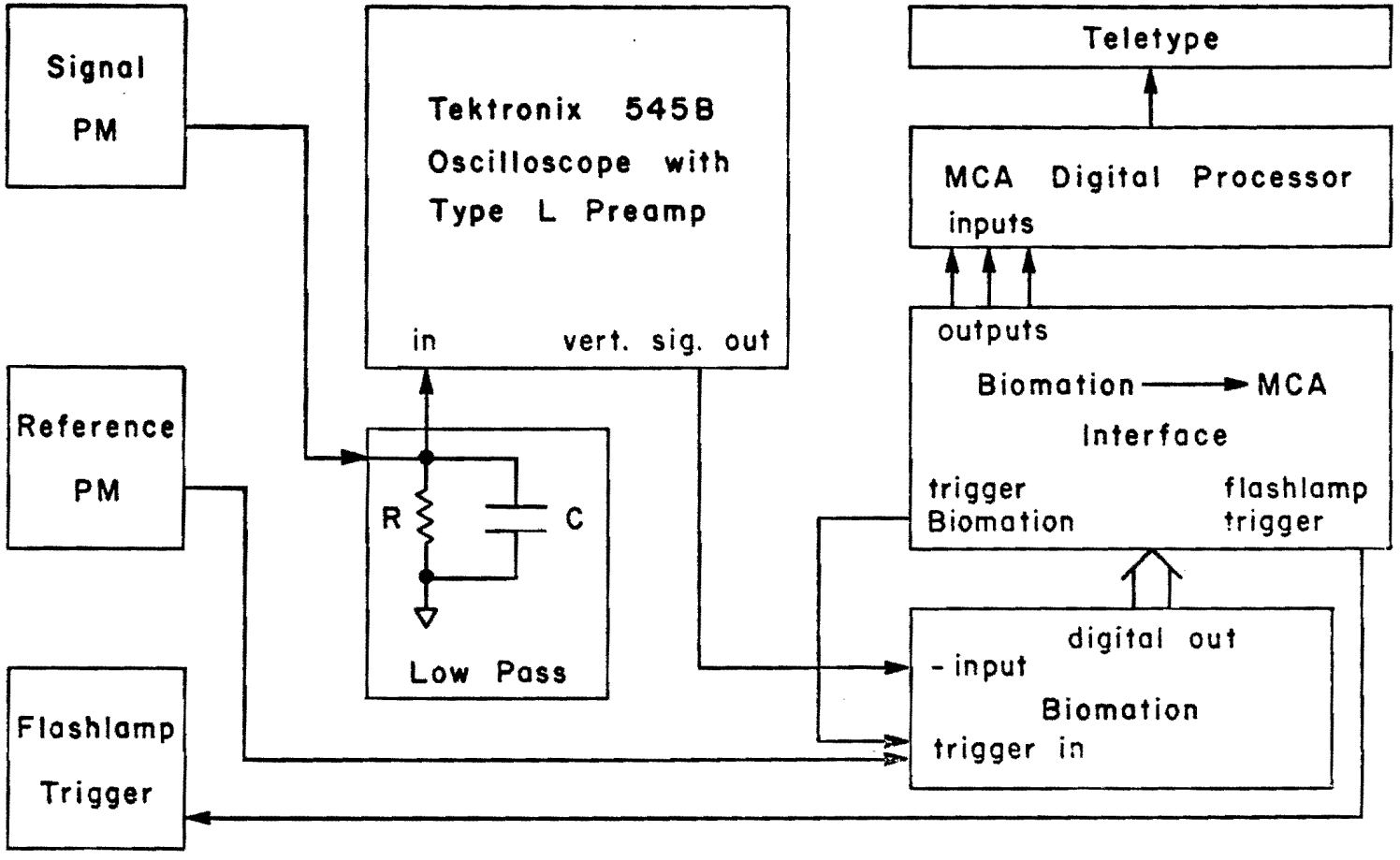

Fig. 14 Transient Digitizing Apparatus Block Diagram

1), the PM signal is a noisy but recognizable decay curve. For a weak phosphor (case 2), individual photons do not overlap, and the "decay" information is in the decreasing number of photons per unit time. In either case, the signal is to be amplified and digitized.

The signal PM is connected through a 1' cable to an adjustable RC low pass filter. The filter smooths the signal and produces a voltage. In case 1, the PM signal is a current; when dropped across R, it becomes a voltage proportional to R. In case 2, the PM signal consists of packets of charge; when applied to C, they become pulses of voltage proportional to C. In either case, the instrumental time constant is RC. RC is set to be less than or equal to the sampling interval of the digitizer. The idea is to make each photon count by stretching it to as long as the sampling interval. (The digitization takes place only during .1 μsec of each sampling interval.)

Amplification (of gain up to x200) by a Tektronix 545B oscilloscope is sufficient to raise the voltage of an individual "photon" to five volts. The Type L preamp has a 30 MHz bandwidth, but the VERT. SIGN. OUT of the scope had a highly degraded frequency response. An isolation amplifier was inserted into the scope and the result is a ~3 MHz amplifier. Only the vertical gain controls on the scope affect the output, and they are continuously variable.

The scope gain is generally varied and the Biomation (610B transient recorder or digitizer) gain is left at five volts full scale. The Biomation's frequency response is 2.5 MHz on the 5 v or higher scales, but is degraded at higher gain settings. (It drops to 100 KHz in the 50 mv range.)

Because a PM produces a negative signal, the "-input" is used to invert the curve. Typically, the Biomation input offset and the scope gain are adjusted so that the decay curve nearly spans the 64 quantizing levels of the 6-bit A to D converter. (The decay curve's tail is subject to quantizing error, as is the baseline.) Sometimes in case 2, the individual "photons" are amplified to 5 v and the baseline is set below zero; then the baseline fluctuations do not contribute to the background.

The Biomation has a 256-channel (or word) memory. Each channel is as long as the sample interval, which can be varied from .1 μsec to 50 msec. Thus, the horizontal full scale can be as small as 25.6 μsec to as large as 12.8 sec, allowing lifetimes of from 1 μsec to 5 sec to be measured. For best results, the entire decay curve is digitized, including a long tail. It is best to know the background, so 50 channels at the beginning or the end of the curve should be devoted to background.

Triggering must occur reproducibly at the moment of the flash, within .1 μsec. The reference (or trigger) PM is hooked directly to "trigger in," and controls are adjusted to obtain reliable triggering. For slow decays, the trigger signal can be derived from a digital step that is synchronized with the flash. Sliding the decay curve horizontally in the memory is accomplished by the "trigger delay" control.

The decay curve after a single flash is usually too noisy to analyze, since the pressure cell restricts light levels. Thus an averaging system was built to add repetitive curves. A curve is digitized and placed in memory; then the lamp flashes again and a new curve is added to the previous one. The process is repeated until a smooth curve is built up.

Acting as the memory is a Hewlett-Packard 5401A multichannel analyzer (MCA). One quarter of the 1024-channel memory is used. For comparison, the other quarters can store smooth curves taken at previous pressures. Each MCA channel has a memory capacity of 10^6, which is more than adequate.

The memories of Biomation and MCA are incompatible; that is, the 6-bit word in the Biomation memory is not easily added to the MCA memory. Therefore an instrument was built which transforms the 6-bit word to a proportional number of counts, which are counted by the MCA in the multiscaling mode. The MCA then accumulates a number of counts in each successive channel proportional to the size of the signal at each successive time (i.e., a decay curve). In Appendix C is a detailed description of the Biomation→MCA Interface.

The Interface also acts as a sequencer for the events of the averaging process. This process is continued automatically until a sufficiently smooth decay curve is built up. For the flashlamp, 100 flashes are usually adequate, taking one minute. For the spark gap, 4000 flashes (taking 10 minutes) are usually sufficient.

When a smooth curve is obtained, the MCA outputs the correct quarter of its memory to a Teletype (model 33), storing it on paper tape (readout takes three minutes). The paper tape is transformed to a set of punched cards on the IBM 1800. The data cards are then run through program DECAY [36] on the MRL computer. DECAY performs a least square fit to the data of a decay function (one or two exponentials, energy transfer, or Becquerel), and outputs a linear or log plot. Deconvolution is possible, to remove the effect of the finite flash width from the data.

In this study, deconvolution was not used, and the single-exponential fit was employed exclusively. The fit was started at a point late enough, such that the flash had ended, and a long tail was included in the fit. Best results were obtained when the background was well known and its average was a fixed parameter in the fit. The background is sometimes disturbed by RFI from the lamp, or (for very long decays) by 60 Hz interference. A checklist explaining how to set up the transient digitizing decay apparatus is reproduced in Appendix D.

4.4 Single Photon Counting

In Appendix E is found a checklist for setting up the single photon counting (SPC) apparatus, as far as it differs from the apparatus of Appendix D. SPC is a method of transient measurement that is capable of very high resolution (say .1 nsec). The apparatus to be described here is limited by the relatively slow spark gap to measuring decays of lifetime longer than 100 nsec. (In compounds that obeyed Eq. (15), it was found [25] that efficiency and lifetime decreased proportionally with pressure until $\tau \simeq 120$ nsec was reached, when the lifetime levelled off. Perhaps with deconvolution of the lamp flash, lifetimes below 120 nsec could be measured.) The longest measurable lifetime is about 50 μsec. (This limitation is an arbitrary cutoff in the electronics, not inherent in the SPC method.) The full range of lifetimes from .1 to 50 μsec was covered in the study found in Part 4.

Aside from the SPC method's speed, it is especially useful in these pressure studies because it can monitor dim decays. For proper operation, the electronics should detect just one emitted photon for every ten flashes

of the spark gap. The flashlamp cannot be used, since one typically flashes the spark gap 5×10^4 times for one decay curve. (Then each curve contains about 5×10^3 counts spread over 256 channels. The average channel has 20 counts, so the standard deviation is a constant $20^{1/2} \simeq \pm 5$ counts throughout the curve.) Considering the rated life of a pair of spark gap electrodes, one can record ten curves before changing electrodes (which is not difficult). At the typical repetition rate of 50 Hz, each curve takes 15 minutes.

SPC measures the time between a "start" signal from the reference PM and a "stop" signal from the signal PM. This time is converted to a pulse height, which is sent to the MCA pulse height analyzer (PHA). The MCA displays number of counts versus pulse height. After many counts, one has a smooth decay curve.

Since the SPC system can only process the first stop photon after the start signal (which occurs at the flash), subsequent photons are lost, and the decay curve is biased toward shorter times. Thus, one can either correct this bias, or make sure that few flashes produce more than one photon. By allowing only one stop every five flashes, 11% of the flashes produce more than one photon; if one in ten, 4% are lost. Or, one can use optimum light levels (an average of one photon for every flash), and correct for double photons. Such a correction program has been written, using the method of Donohue and Stern [45]. (Other references on SPC are [41,46-48]).

For the data of Part 4, the monochromator slits were adjusted so that one emitted photon was detected for about every ten flashes. The number of starts was noted and fed into the correction program. Corrected liftimes were typically one to five percent longer than uncorrected lifetimes. The

correction program worked for lower ratios of starts to stops, but in order to keep the correction small, a ratio of ten was used. To avoid correcting entirely, a prohibitively large ratio of 100 must be used [46,47]. The correction depends on an assumption that the number of photons detected by the PM after a flash is given by a Poisson distribution. In a rudimentary fashion, this assumption was checked by us and found to probably be good to 10%. Variation of the intensity into the cell from flash to flash would lead to a non-Poisson distribution (or equivalently, a changing ratio of starts to stops). The spark gap has noticeable arc wander, so its intensity must be quite variable. It is not known how much this affects the data. One quirk in the correction program should be noted: The last few channels sometimes do not converge. In this study, points 251 to 255 were weighted zero in the fits.

Fig. 15 shows a block diagram of the SPC apparatus. The reference PM (1P28) puts out a start pulse derived from many photons in the flash. The signal PM (9558) detects the first emitted photon. Both pulses are shaped by discriminators into fast negative-logic pulses to be sent to the Ortec 467 time to pulse height converter (TPHC). The stop pulse from the signal PM passes through an Ortec 425A nanosecond delay, a passive device that delays the pulse from 0 to 63 nsec. Delaying the stop pulse avoids using the nonlinear low-amplitude region of the TPHC output pulse. The number of starts is counted by the photon counter.

In the TPHC, the start pulse begins the charging of a ramp from 0 to 10 volts on a capacitor. A stop pulse ends the charging, and a pulse of height equivalent to the ramp voltage is output to the PHA. The TPHC pulse

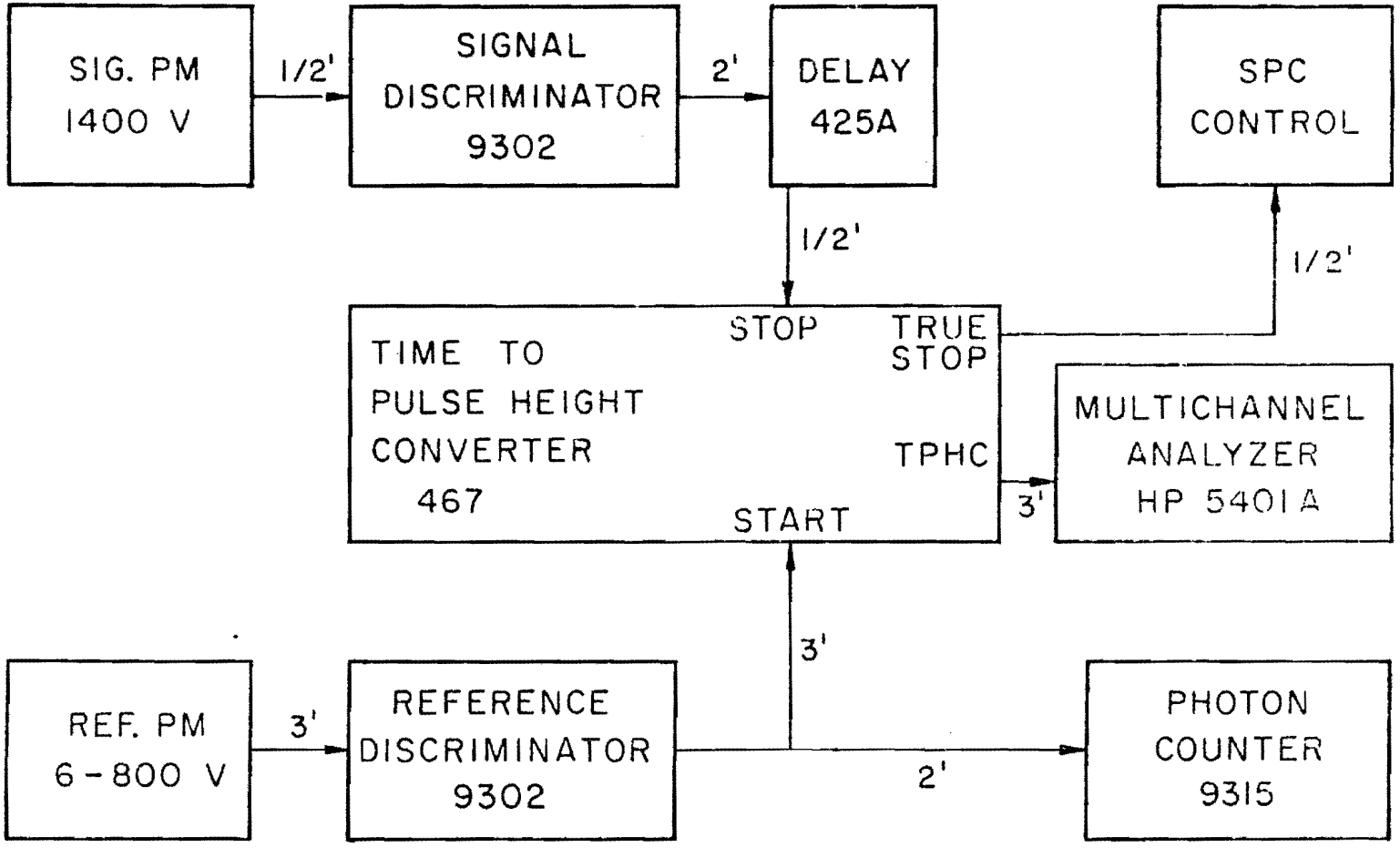

Fig. 15 Single Photon Counting Apparatus Block Diagram

width is >1 μsec so that PHA is set for a time to peak of 1 μsec. An analog to digital conversion occurs in the PHA, transforming the pulse height to a corresponding channel number. That one of the 256 channels is then incremented. After some time, the curve of number of pulses per unit pulse height versus pulse height is recognizable as its equivalent, a decay curve (intensity vs. time).

A calibration of channel number versus time must be made for each range of the TPHC. The nanosecond delay provides a precise time interval. In Fig. 15, START is connected to the signal discriminator output, and stray light hits the signal PM. Counts then accumulate in a single channel which depends on the delay time. This method calibrates the four fastest TPHC ranges, and the calibration is simply extrapolated to the eleven slower ranges. The necessity for extrapolation and the slight discrepancies between two independent calibrations limit confidence in the calibration to ±5%.

The SPC Control (also called the counter/oscillator or pulse generator-counter) was built in this laboratory to control the SPC system. It contains an oscillator to externally flash the Nanopulser at up to 160 Hz (instead of 50 Hz). It also counts digital (TTL) signals. The TRUE STOPS output of the TPHC gives a 5 v pulse for each count sent to the MCA. With the SPC Control monitoring TRUE STOPS and the photon counter totalizing starts, the starts to stops ratio is known. The SPC Control's capability to run the lamp was not used because RFI fed back from the lamp. However, it would be worthwhile to run the Nanopulser at 160 Hz or higher (to reduce the correction, or speed data-taking). One simply needs to plug an external oscillator (e.g., the one described in Appendix F or the SPC Control isolated

by the optical coupler of Appendix C) into the Nanopulser's REMOTE AUTO TRIGGER input. A quirk of the system should be noted here: The number of stops totalized by the SPC Control is always slightly less than the total number of counts in the MCA memory. This occurs because the largest pulses from the TPHC overrange the PHA and are lost. The latter number is used in the correction program.

In the development of the SPC apparatus, a major problem was RFI. The early parts of fast decay curves contained spurious oscillations. A solution seemed so remote that a digital filter [25] was incorporated into program DECAY, to remove spikes found in the Fourier transform of the decay curve. The digital filter did not work well and was not used here. Eventually, several steps seemed to lead to a virtual disappearance of the RFI problem: 1) All cables were shielded with braid. 2) The high-voltage cable from Nanopulser to lamp was lengthened and the Nanopulser was set apart. 3) The cable from signal PM to discriminator was minimized in length. 4) Normally -1200 v, the signal PM bias voltage was maximized at -1400 v. 5) The signal discriminator level was set as high as possible without affecting the lifetime.

Two miscellaneous facts should be added: A feature of the TPHC was found very useful in this study; the "stop inhibit mode" ignores stop pulses in the first .1 to 1 μsec. Thus a large fast component or reflected flash can be eliminated from the data with no further concern. Also, while not very important here, the fact that light and pulses traverse only a foot in one nsec means that great care must be taken with optical path and cable lengths in trying to measure very fast lifetimes by SPC.

3. EFFECTS OF PRESSURE ON THE OPTICAL PROPERTIES OF ALKALI HALIDES DOPED WITH Cu^+ AND Ag^+

1. Background and Theory

1.1 Absorption

When the noble metal ions Cu^+ and Ag^+ are substituted for a small fraction of the cations in most alkali halides, relatively weak optical absorption and emission bands appear. The absorption bands, labelled A through G, lie on the low-energy side of the fundamental absorption edge. The low-energy bands, A to F, have highly temperature-dependent oscillator strengths f(T). Band G is a charge-transfer band with a temperature-independent f(T) stronger than that of bands A-F [49]. In addition, there is an A* band, lying at lowest energy, that is concentration-dependent. Since this band is attributed to pairs of noble-metal ions, we are interested in it only insofar as it may obscure the single-ion effects.

The A through F manifold is assigned to the forbidden d^{10} to d^9s transition of the free ion because of the large increase in f(T) with temperature. In the free ion, this transition is parity forbidden by the Laporte rule. (Photons, which have odd parity, cannot cause a transition between two even states in the dipole approximation.) At low temperature in the centrosymmetric O_h environment of the alkali halides, the Laporte rule continues to hold. However, as T rises, lattice vibrations intermittently destroy the inversion symmetry, and the optical transition becomes partly allowed. In other words, odd lattice distortions can mix electronic states of odd parity with the even initial and final levels, making the transition vibronically allowed.

It is not certain which odd configurations mix most strongly with the even initial and final levels. Only mixing with the upper d^9s level is considered by most workers. The two odd configurations with close enough energy to interact with the upper level are the d^9p level and the charge transfer state which results in the G band. Fowler [16] gives a review of the evidence for Ag^+ and concludes that the charge transfer state mixes most strongly with the d^9s level. The question of configuration interaction will become important in the discussion of results.

No more certain than the assignment of mixing levels is the exact nature of the lattice distortion responsible for mixing. The distortion may be dynamic (lattice vibrations) or static, and the electron-lattice (EL) coupling may be carried to all orders [50]. In the simplest case of linear electron-phonon coupling, the oscillator strength is given by

$$f(T) = f(0) \coth (h\Omega/4\pi kT) \quad , \tag{23}$$

where $f(0)$ is the oscillator strength at $T = 0$, and Ω is the frequency of an odd phonon or group of phonons of similar frequencies [51]. For the ions Ag^+ and Cu^+ (and others), the most prominent odd phonon is the T_{1u} resonant mode, which shows up in low temperature ir absorption measurements as a strong, sharp peak at the low frequency Ω [52]. In this local normal mode, the nearest neighbors move one way, while the impurity ion moves in the opposite direction with large amplitude. At high temperatures, Eq. (23) gives an $f(T)$ that is linear with temperature, because $\coth (1/x) \to x$.

More- or less-than-linear behaviors with temperature are attributed to higher-order terms in the EL interaction. The EL interaction Hamiltonian for a parity-forbidden transition is given by [50]

$$H^{EL} = ArQ^- + BrQ^-Q^+ + \ldots$$
$$+ ArQ_d^- + BrQ_d^-Q_d^+ + \ldots \qquad (24)$$
$$+ BrQ^-Q_d^+ + BrQ_d^-Q^+ + \ldots \ ,$$

where Q^- is an odd vibrational coordinate, Q^+ is even, Q_d is a static distortion, r is an electronic coordinate, and the A's and B's are coupling coefficients. We have considered the first term in Eq. (24), which results in Eq. (23). Such an approximation is not adequate for absorption in the phosphors considered here. To explain the f(T) data, one must include a Q^-Q^+ term for Ag^+ in KH (the potassium halides); a Q_-^4 quartic anharmonicity term for NaCl:Ag, KCl:Ag and KBr:Ag; a Q_d^- term for KH:Cu, NaCl:Cu and KCl:Ag; and a $Q_d^-Q_d^+$ term for KCl:Ag and NaCl:Cu [50].

The static distortions are, for many workers, the most interesting aspect of this field. For a small ion like Cu^+ (.96 A ionic radius) or Ag^+ (1.26 A), it can be shown [52] that the attractive and repulsive forces between the impurity and the nearest neighbors are nearly equal, so that the force constant is small and the frequency of the resonant mode is quite low. In fact, the balance of forces may be such that the impurity ion is unstable at the center of symmetry and so moves to an off-center position (or rather, tunnels among several equivalent off-center positions). An off-center ion is effectively in an odd-parity static lattice distortion, so that the Laporte rule is continuously broken. One would expect the oscillator strength to be large and nearly temperature-independent, and such is the case in KH:Cu [53] and NaI:Cu [54].

The attractive force due to anion polarizability increases the off-center effect in the sequence Cl<Br<I. The tendency for the impurity to go off-center is encouraged if it has room to do so. Thus the smaller the impurity, and the larger the cation which it replaces, the more likely

is an off-center position. It is not surprising, then, that the large Ag^+ ion is off-center only in some Rb and Cs halides, while the smaller Cu^+ ion is off-center in the K and Rb halides and in NaI:Cu [53,54]. (Note that cation ionic radii are Na^+ - .95 A, K^+ - 1.33 A, and Rb^+ - 1.48 A.) In Table 4 are given oscillator strengths at 80° K and 300° K. On-center ions have small but increasing f(T), while off-center ions have large and constant f(T). The uv absorption measurements have been supplemented by ir absorption [52], electrocaloric and ionic thermocurrents [53] studies, confirming the off-center interpretation.

1.2 Emission

Emission measurements stand alone, since the sort of alternative experiments that can corroborate absorption data (ir or thermal studies) are not possible. That is, investigations of the ground state are much easier than studies of the short-lived relaxed excited state (RES). This is one reason the section on absorption was long and complicated, while the emission section will be simpler. Only recently have a number of emission studies (featuring lifetime measurements) appeared [55-61]. The majority of research on noble metal ion-doped alkali halides has involved uv or ir absorption. In some ways the absorption and emission processes are similar, but one must be careful in using findings about the ground state in studies of the RES.

It is not even true that the state to which the optical center is excited in absorption is very similar to the RES from which emission occurs. An indication of the difference is given by the large Stokes' shift ($>10^4$ cm^{-1} for AH:Cu and smaller for AH:Ag). In addition, it will be shown in section 2 that the center increases in volume by an unusually large amount ($q_0/V \sim 20\%$) upon excitation. The increase in size predicts that the ion

Table 4

Transition Probability as a Function of Temperature[a]

	absorption - $f(x10^{-3})$		emission - $1/\tau$ (msec)	
crystal	80°K	300°K	80°K	300°K
NaCl:Cu	1 (4)	1.6 (6.4)	15	30
NaBr:Cu			4	9
NaI:Cu	240	240	14 (50)[b]	50 (50)
KCl:Cu	26 (26)	27 (32)	29	40
KBr:Cu	60	68	9	12
KI:Cu	56 (100)	60 (176)	45 (40)	100 (67)
NaCl:Ag	1	5	29	50
KCl:Ag	5	20	48	63
KBr:Ag	4	17		

[a] Compiled from numerous sources. Numbers in parentheses are different measurements by still other workers.

[b] For NaI:Cu, Mack and van Sciver [60] found that $1/\tau$ has a temperature dependence given by Eq. (25), so they label it on-center. Piccirilli and Spinolo [61] find that τ is constant with T, and they call NaI:Cu off-center. Both experiments seem careful, though the latter makes no mention of special handling procedures for the highly deliquescent NaI:Cu. From a theoretical standpoint, too, one must favor the on-center experiment, since if NaI:Cu is off-center, all the KH:Cu would probably be off-center in emission, and only KI:Cu is.

is less likely to be off-center in the RES, and this is found to be the case. Whereas KH:Cu and NaI:Cu are off-center in the ground state, only KI:Cu (and perhaps NaI:Cu) is off-center in the RES.

Another difference between absorption and emission is that off-center and on-center phosphors behave similarly in high-temperature emission, which is not true in absorption. Looking at Table 4, one notices that the temperature dependence of the lifetime for off-center KI:Cu and all the on-center phosphors is identical ($1/\tau$ doubles from 80° K to 300° K [61]). The great rise in τ for on-center emission occurs lower than 100° K. In absorption, on the other hand, f(T) increases by a factor of four in on-center phosphors but is quite steady in off-center phosphors over the temperature range 80-300° K [50]. At 80° K, the off-center oscillator strength is an order of magnitude higher than for an on-center phosphor. The same is true for $1/\tau$ in emission only if it is assumed that the off-center effect causes the iodides to be out of the sequence I<Br<Cl [61]. This assumption may be disputed. In any case, a convincing demonstration of the unimportance of the off-center effect in room temperature emission is the convergence above 250° K of $\tau(T)$ at about 25 μsec in the four Cu^+-doped iodides, only half of which show an on-center temperature dependence. The conclusion is that the off-center effect cannot dominate these room temperature emission studies because there are few off-center phosphors, and the effect is minor at 300° K.

It is shown by Fowler and Dexter [22] that one cannot always predict $1/\tau$ from the oscillator strength (see part 1). This is especially true for Ag^+ and Cu^+-doped alkali halides, because of the dissimilarity of the ground and relaxed excited states. The lifetime predicted from the oscillator strength can be orders of magnitude faster than the measured lifetime

if an off- to on-center transition occurs upon excitation (as in KCl:Cu, KBr:Cu, and perhaps NaI:Cu). Even when both ground and excited states are on-center, the optical transition can be 10-100 times more allowed in absorption than emission [59]. (This cannot be seen from Table 4, since it is necessary to multiply $1/\tau$ by factors that vary through the table, in order to compare f and $1/\tau$.)

In analogy with Eq. (23), an on-center ion that obeys linear electron-phonon coupling is expected to have a lifetime $\tau(T)$ given by

$$\frac{1}{\tau} = \frac{1}{\tau_0} \coth \frac{h\Omega}{4\pi kT} \quad , \tag{25}$$

where τ_0 is the T = 0° K lifetime. In contrast to the absorption case, several of the phosphors follow Eq. (25) exactly, namely NaCl:Ag [57], LiI:Cu, and NaI:Cu [60]. In other cases, an off-center distortion appears to disrupt the agreement with Eq. (25) at low temperatures, as in KH:Cu and NaH:Cu [61]. (There is a controversy over NaI:Cu, which is explained in Table 4.) The net judgment is that the Ag^+-doped AH are probably on-center obeying Eq. (25), KI:Cu is off-center at room temperature, and the other Cu^+-doped AH have excited potential wells that are slightly distorted by off-center effects. These distortions might necessitate corrections to a simple, harmonic configuration-coordinate model.

In summary, while the absorption process and the ground state are well characterized for the noble metal ion-doped alkali halides, the findings must be applied with care to the more poorly-characterized emission process involving the RES. Internal conversion and thermal relaxation after excitation mean that the RES has a much larger volume and perhaps even a different symmetry than the ground state. Thus the temperature dependence and absolute magnitude of the transition probability are dissimilar in

absorption and emission.

Fortunately, the EL coupling, particularly as it concerns the off-center effect, takes a simpler form in the high temperature excited state. Linear electron-phonon coupling appears to be adequate where static distortions play no part. And at 300° K, the off-center distortions seem not to determine the transition probability. (At such a high temperature, even "on-center" ions spend most of their time off-center.) The next section incorporates the effect of pressure into the theory of the linear EL interaction. From the results of this section, we expect such a modified theory to adequately explain $\tau(p)$ results, and this is found to be the case.

2. Results

Excitation in any of the uv absorption bands leads to visible emission from the same state, following internal conversion. In this study, the Ag^+-doped crystals were excited in the A, B, and C bands, while the Cu^+-doped crystals were excited in the D band. A single emission peak results, except that at lower energy, a peak due to ion pairs sometimes appears. According to the explanation to follow, which will invoke quadratic EL coupling, the single emission peak should be a skewed Gaussian. However, light levels were so low that the peak shape could not be well determined, and data were fit with a symmetric Gaussian.

The emitted intensity greatly decreased with pressure, but quantitative measurements of intensity vs. pressure were not possible. Emission peak positions and half-widths were measured as functions of pressure for nearly all the sodium and potassium halides doped with Cu^+ and Ag^+ (see Appendix G). Missing are NaI:Ag, KI:Ag (which does not emit), and NaCl:Ag (whose excitation energy is too high). Figures 16 and 17 display typical data. Peaks always shifted to higher energy, except at the potassium

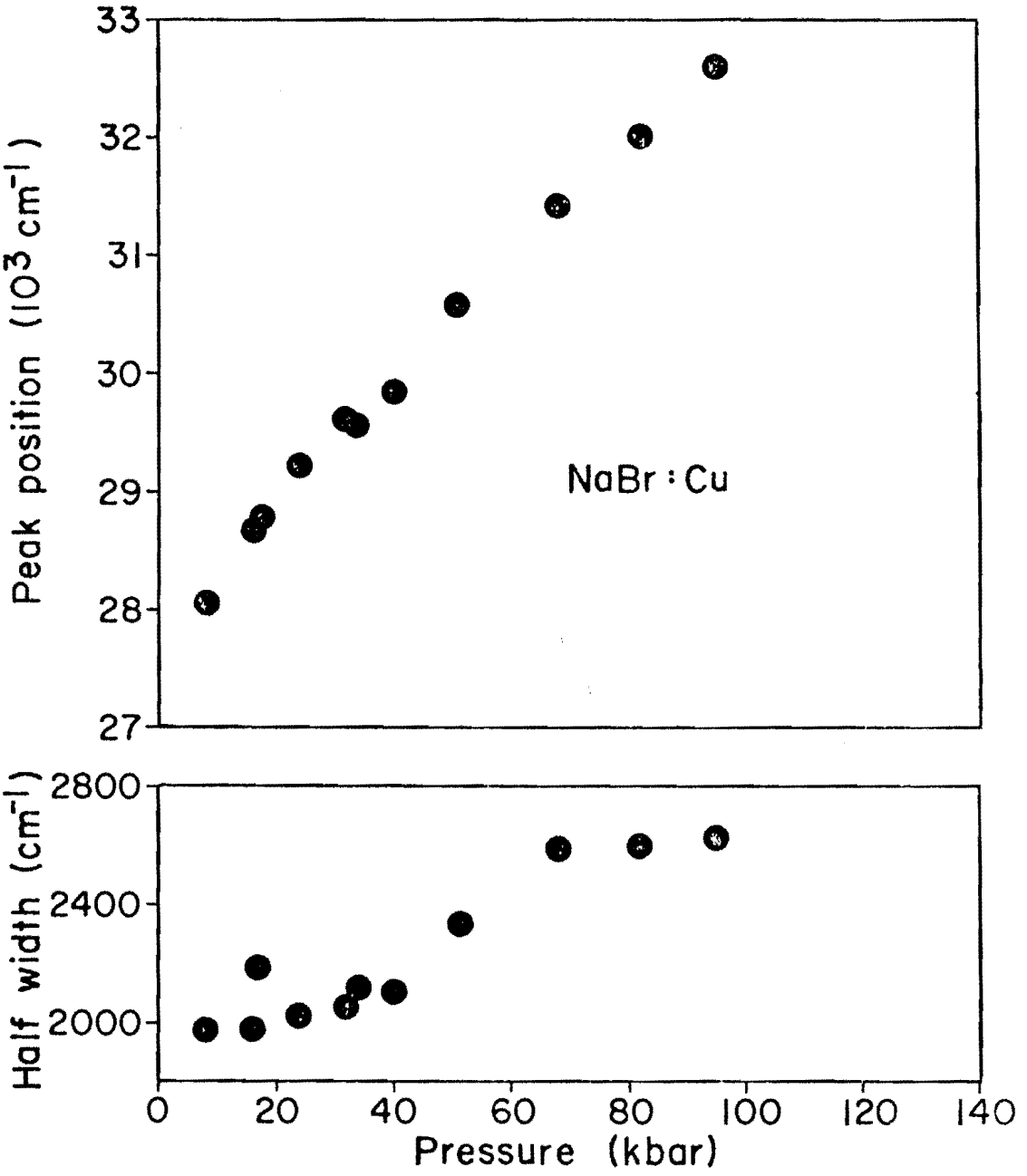

Fig. 16 Emission Band Shift and Halfwidth Change with Pressure for NaBr:Cu

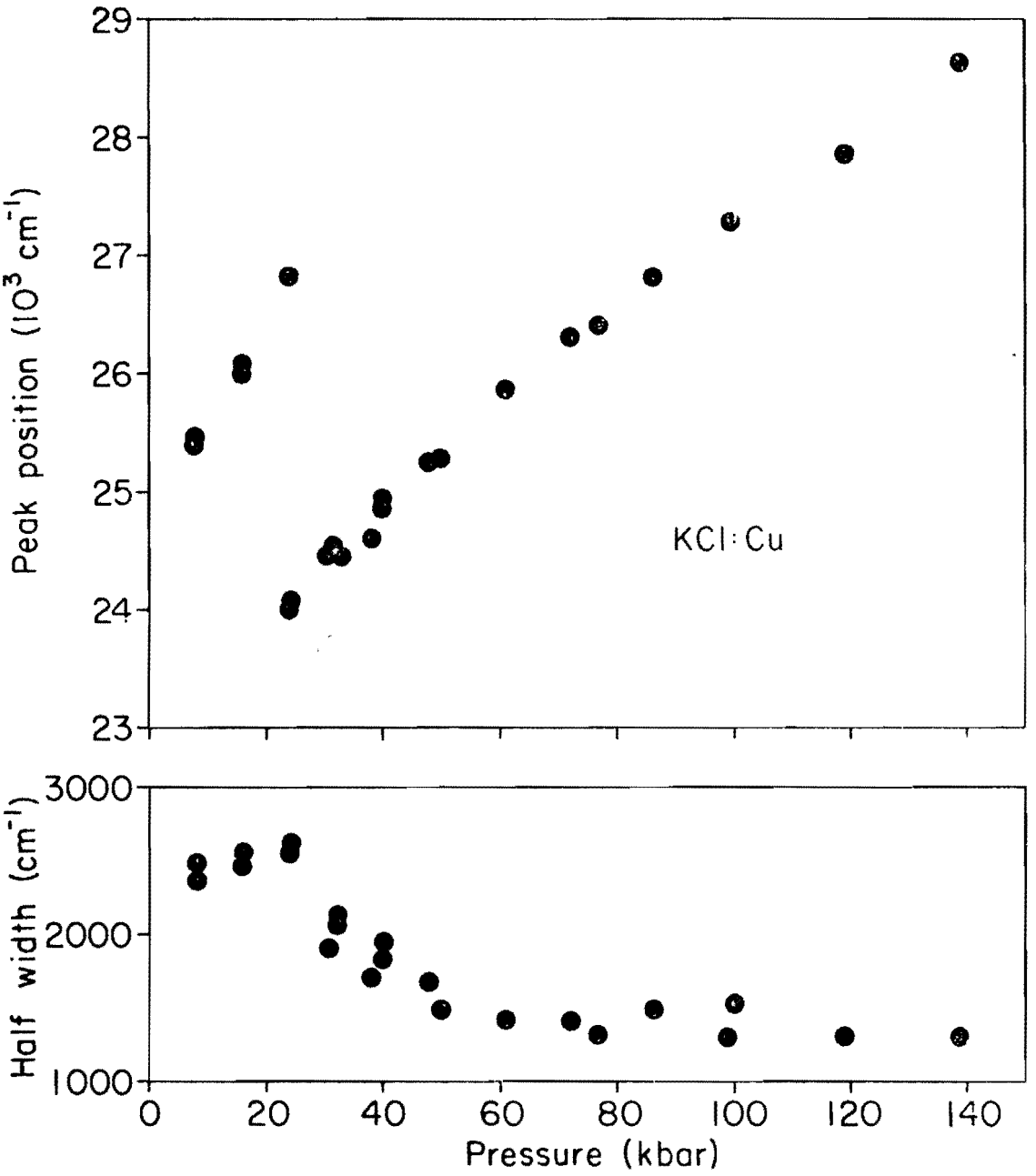

Fig. 17 Emission Band Shift and Halfwidth Change with Pressure for KCl:Cu

halide phase transition (from the fcc to the simple cubic or sc structure) near 19 kbars. The values in Tables G1 and 2 are from linear or quadratic fits, depending on the data. For instance in Fig. 17, the fit to the peak shift is linear below the phase transition and quadratic above. Over a wide pressure range, a quadratic fit could be employed, as for NaH:Cu and sc KH:Cu. But only a linear fit to the peak shift data was justified for fcc KH:Cu and the Ag^+-doped crystals. A linear fit to the change with pressure of the halfwidth was used throughout Table G2.

Lifetimes were single exponentials in all cases. The transient digitizing apparatus was used exclusively here. For decays longer than 20 μsec, the flashlamp excited the sample, while the spark gap was employed for shorter decays. Fig. 18 shows decay curves at two different pressures for NaI:Cu; the early background and long tail were found to be useful in fitting the curves, when they became noisier at higher pressures in Cell II. The change of the lifetime with pressure is pronounced in Fig. 18; the curves are reduced to data points and plotted in Fig. 19.

Luminescent lifetime as a function of pressure $\tau(p)$ is plotted in Fig. 19 and 20 for some phosphors. From least squares fits to such data, Table G3 is constructed. A quadratic (linear) fit was employed for sodium (potassium) halide data. Due to reduced intensity, it was sometimes impossible to reach the highest pressures. While the lifetime (except in sc KCl:Ag) always increases with pressure, as does the emission peak shift, there are two noteworthy differences: 1) At all pressures, the energy of the Cu^+ peak position (except in fcc KCl:Cu) changes in the sequence I<Br<Cl. However, the Cu^+ lifetime increases in the sequence I<Cl<Br. In both Ag^+ and Cu^+-doped potassium halides, the peak position drops at the phase transition, whereas the lifetime rises in KCl, remains constant in KBr, and drops in KI.

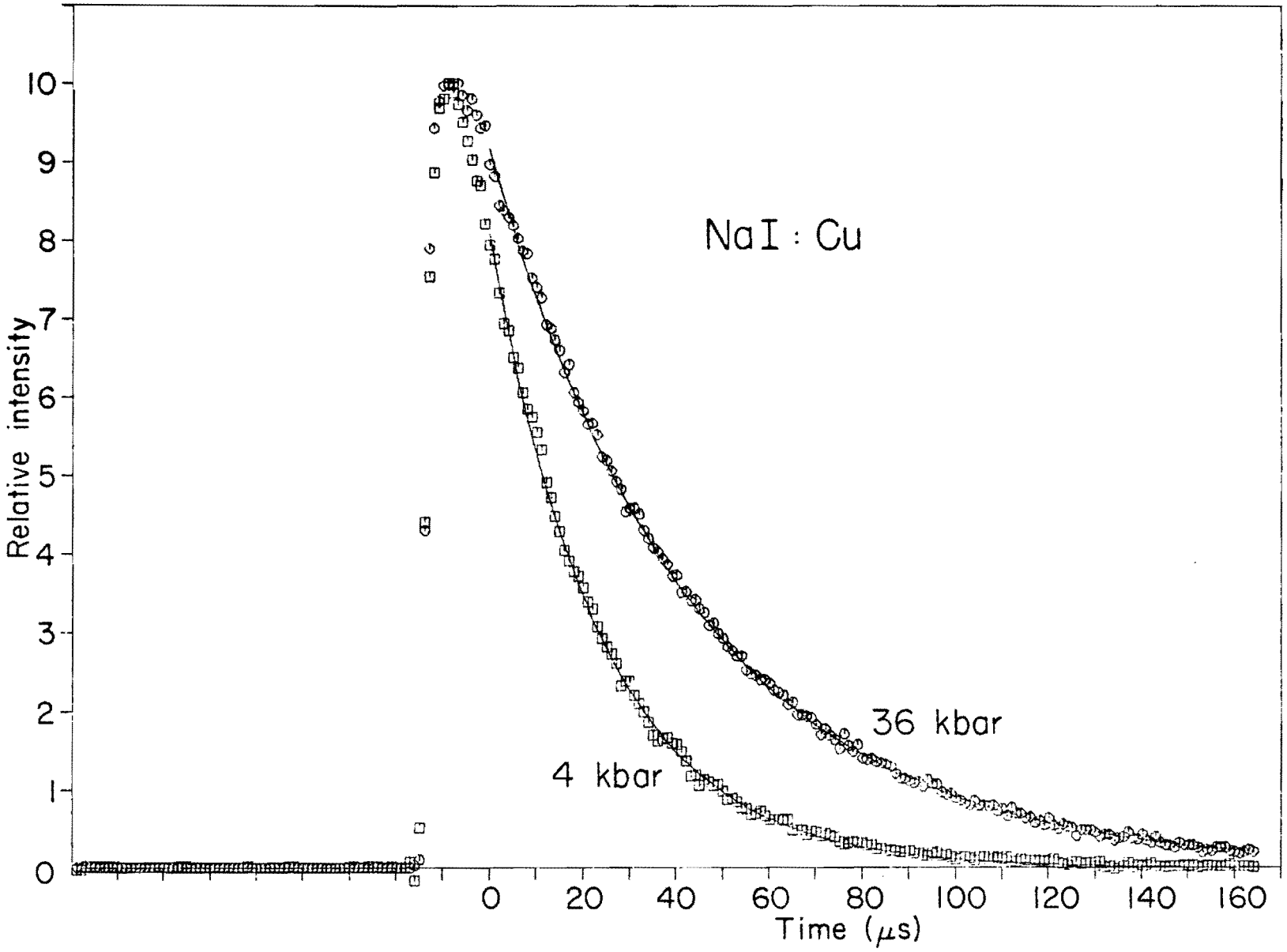

Fig. 18 Typical Decay Curves from Transient Digitizer (NaI:Cu at 4 and 36 kbar)

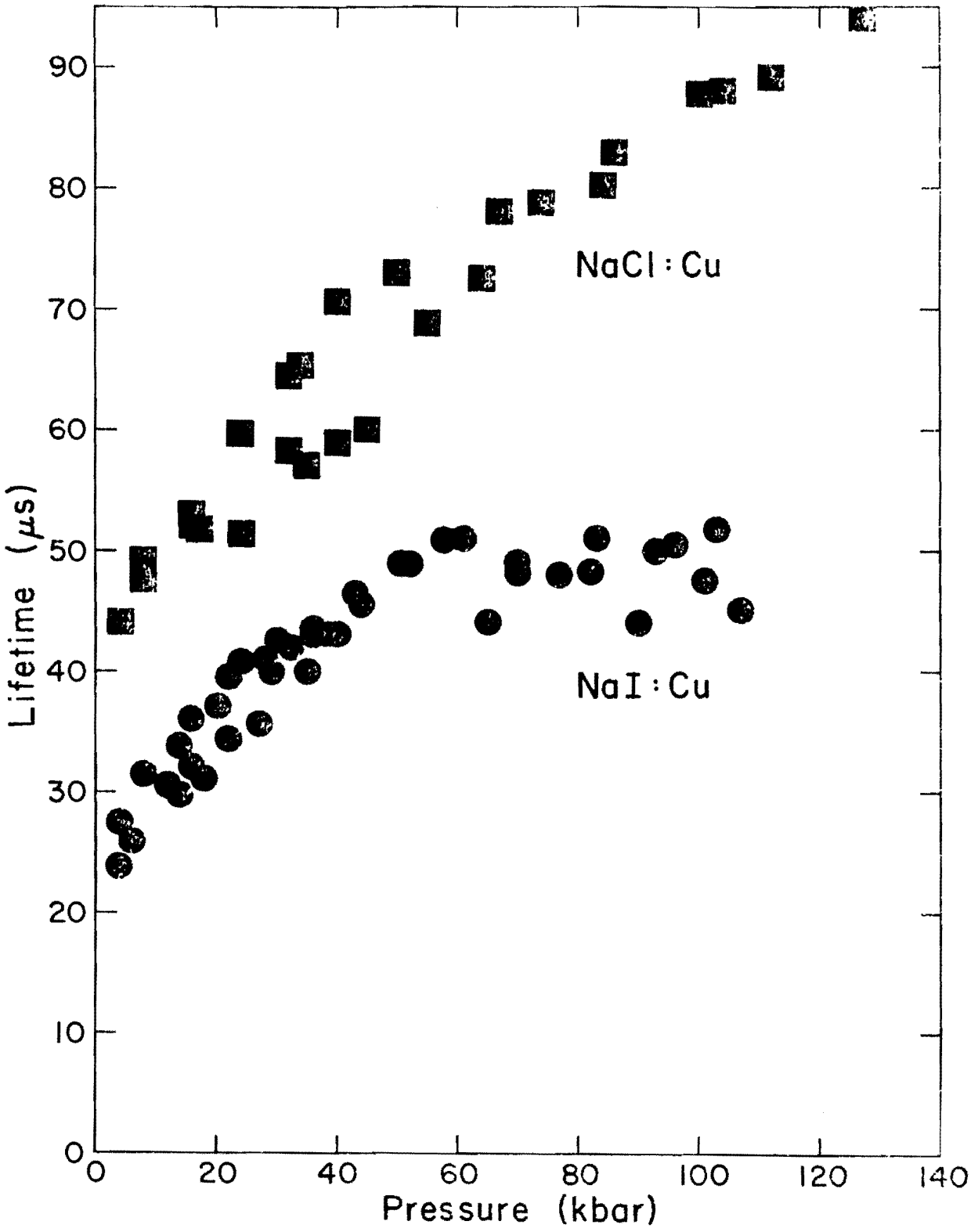

Fig. 19 Lifetime Change with Pressure for NaCl:Cu and NaI:Cu

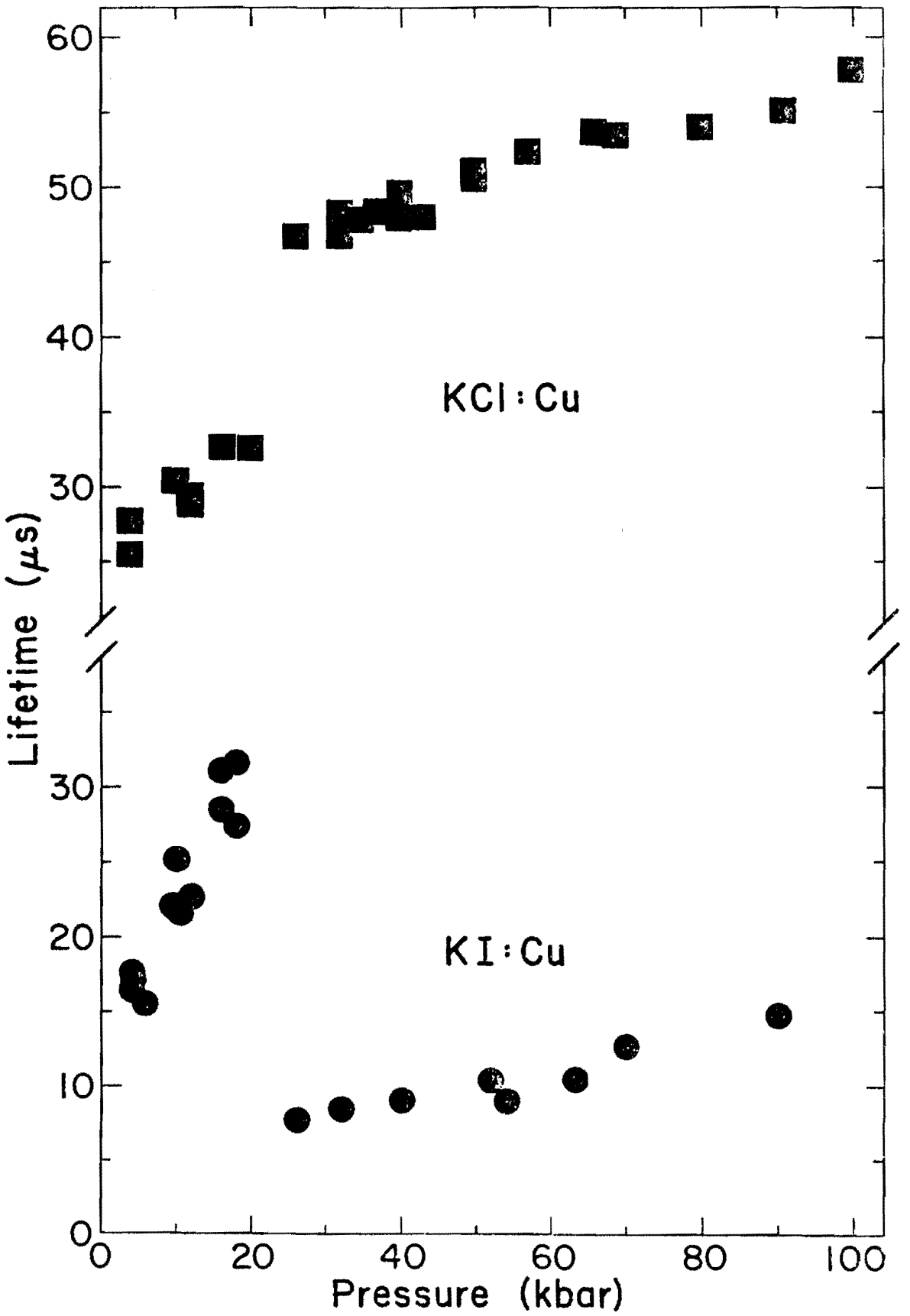

Fig. 20 Lifetime Change with Pressure for KCl:Cu and KI:Cu

In a solid of optical refractive index n, an allowed transition of a localized luminescent center will have a lifetime τ given by Eq. (16). If M is constant with pressure for e.g. NaCl:Cu, the known peak shift and refractive index change with pressure allow a calculation of the lifetime change in 60 kbar: τ should drop by 30%. Instead, it rises by 70%. It is thus clear that M must be pressure dependent.

There have been a number of studies of very high-pressure lifetimes (see part 1). In many organics and some simple inorganics, Eq. (16) appears to describe the effect of pressure (that is, small). In our experience, the majority of luminescent systems are more complicated than Eq. (16) allows, and the dynamics are strongly pressure-dependent. Among the doped alkali halides, such systems include sensitized phosphors [34] and Jahn-Teller split centers (see part 4). For the centers discussed here, Eq. (16) is adequate if a pressure-dependent M is used.

The Cu^+ and Ag^+-doped alkali halides display large lifetime changes with pressure. In general agreement with our results, lifetimes and peak shifts have been measured [55] for some of these phosphors to 6 kbar. This hydrostatic study rules out the possibility of shear strain effects in our data. Furthermore in other studies in this laboratory [33] involving measurements of peak shifts, peak shapes, and intensities, measurements in the quasihydrostatic NaCl pressure-transmitting medium have been reproduced to 12 kbar by measurements in a truly hydrostatic medium.

3. Discussion

The effect of pressure on localized luminescent centers in solids can best be described by a single-configuration coordinate model, where the coordinate of interest is the A_{1g} breathing mode. Applying pressure to this model leads to a set of equations [33] describing emission peak shifts

and half-width changes. By comparing these equations with fits to the data, the parameters of the model are obtained. Four parameters link the ground and excited harmonic potential wells: q, the relative horizontal displacement of the wells along the configuration coordinate of interest; ω^2 or $(\omega')^2$, the force constants of the ground and excited states; $R = (\omega'/\omega)^2$; and E_{th}, the vertical energy difference between the well bottoms (see part 1).

As a first approximation, we assume that ω^2 and R are independent of pressure. The pressure dependences of E_{th} and q are given by Eqs. (19) and (20), rewritten as

$$E_{th} = E_o + (q + q_o)\frac{P}{2} \tag{26}$$

and

$$\frac{q - q_o}{q_o} = \frac{(R - 1)}{q_o\omega^2 R} P = \alpha_b P \quad , \tag{27}$$

where E_o and q_o are atmospheric pressure values. It can be seen that vertical relative motion of the wells depends on the horizontal well displacement. Horizontal motion depends on unequal force constants (quadratic coupling). The large positive peak shifts of Figs. 16 and 17 imply that q_o is large. (The luminescent center expands upon excitation.) The small negative curvature shows that R is a little less than one. (The excited state has a weaker force constant than the ground state.) From Eq. (27), therefore, the volume difference is large but decreasing with pressure. The volume difference q is a measure of the linear electron-lattice coupling, and it is the parameter that will affect the probability of a phonon-assisted transition.

From steady-state emission data, the model parameters R, $(\omega')^2$, and q_0/V have been compiled in Table 5. V is the molecular volume of the alkali halide at atmospheric pressure for the fcc phase and at 20 kbar for the sc phase. When q_0 is on the order of 20% of V as seen here, the electron-lattice coupling is quite strong, and the ground and excited states can have very different properties. For the sc phase of KI:Cu and KBr:Ag, q_0/V is so small that the values of R and $(\omega')^2$ are not reliable.

The equations used to calculate the parameters of Table 5 from peak shift and halfwidth data are [33]

$$h\nu_{em} = (h\nu_{em})_0 + pq_0/R + p^2(R - 1)/(2\omega^2R^2)$$

and

$$HW = N\omega/R^{1/2} \left| q_0 + p(R - 1)/\omega^2R \right| \quad ,$$

where $N = (8kT\ \ln 2)^{1/2}$. For the sc phase of the potassium halides, pressure is measured from a reference pressure p_0 of 20 kbar, and the equations are so modified. (For the fcc phase, $p_0 = 0$.) Where a linear and a quadratic term for the peak shift are known, only the p_0 intercept of the linear fit to the HW change is used. Otherwise, the linear peak shift, linear HW change, and HW intercept determine the three parameters q_0, ω, and R.

The optical transition $d^{10} \leftrightarrow d^9s$ is parity forbidden by the Laporte rule in free Cu^+ and Ag^+ ions. The transition energy rises as the ion enters a solid, and continues to rise upon further compression, as we have seen. The lifetime remains in the millisecond range at low temperature, but as T rises, odd phonons mix electronic states of odd parity with the initial and final states, making the transition vibronically allowed. For

Table 5. Configuration coordinate model parameters R, ω^2, and q_o are used to calculate the lifetime change, which is compared to experiment.

Compound	phase	R	$(\omega')^2$ $\frac{(kbar^2)}{cm^{-1}}$	q_o/V	$\tau(p_o + 20 \text{ kbars})/\tau(p_o)$[b] calculated	measured
NaCl : Cu	fcc	.808	1.00	.223	1.17	1.26
NaBr : Cu	fcc	.865	.832	.196	1.14	1.15
NaI : Cu	fcc	.799	.743	.139	1.27	1.50
KCl : Cu	fcc	1.33[a]	.668	.360	.85	1.32
KBr : Cu	fcc	1.0	.659	.223	1.0	1.41
KI : Cu	fcc	.774	.702	.136	1.25	2.60
KCl : Cu	sc	.804	1.30	.150	1.17	1.06
KBr : Cu	sc	.646	1.58	.108	1.33	1.12
KI : Cu	sc	.406	7.2	.023	1.49	1.27
NaBr : Ag	fcc	.849	1.31	.228	1.10	1.40
KCl : Ag	fcc	.620	.856	.215	1.33	1.57
KBr : Ag	fcc	.439	.751	.156	1.85	67. (2.)[c]
KCl : Ag	sc	1.034	2.90	.199	.99	.90
KBr : Ag	sc	.337	78.	.011	1.11	1.22

[a]The value of R for the fcc phase of the potassium halides depends on small changes in half-width established over a short pressure range and may not be reliable.

[b]All fcc values use a reference pressure p_o = 0 kbars. For the sc phase, p_o = 20 kbars.

[c]Using linear extrapolation from 8-18 kbar to discount a thermal quenching effect.

a phonon of frequency Ω, the lifetime's temperature dependence is given by Eq. (25) in linear EL coupling, which is expected to be adequate. The pressure dependence, if any, is contained in the factor τ_0.

Kubo and Toyozawa [62] have described a phonon-assisted transition in terms of a configuration coordinate model. If the phonon assistance is dominated by a mode of coordinate Q_a, the dipole matrix element M is expanded

$$M(Q_a) = M_0 + M_1 Q_a + M_2 Q_a^2 + \ldots \quad . \tag{28}$$

Say this mode mixes an odd level ℓ with the excited state ℓ''. Then their Eq. (4.14) reduces in first order to

$$M(Q_a) = M_1 Q_a = \frac{u_{a\ell''\ell}}{E^{(o)}_{\ell''} - E^{(o)}_{\ell}} M^{(o)}_{\ell\ell'} Q_a \quad , \tag{29}$$

where u is the EL coupling and E is an energy level. ($M_0 = 0$ for a transition that is strictly forbidden at the center of symmetry.) Expanding Eq. (29) linearly in pressure, one finds that

$$M(Q,p) = M(Q,p_o) + M(Q,p_o) \left[\frac{1}{u_{a\ell''\ell}} \frac{\partial u_{a\ell''\ell}}{\partial p} + \frac{1}{M^{(o)}_{\ell\ell'}} \frac{\partial M^{(o)}_{\ell\ell'}}{\partial p} - \frac{1}{\Delta E} \frac{\partial \Delta E}{\partial p}\right] (p-p_o) \quad .$$

The last term involves $\Delta E = E^{(o)}_{\ell''} - E^{(o)}_{\ell}$, which could very well change with pressure, as do other energy splittings. However, as will be discussed, the value of the last term is completely unknown. The second term involves the intrinsic matrix element between two levels, and unless their symmetry changes, there should be no pressure dependence. The first term, involving the change with pressure of the EL coupling, can (we believe) be calculated from steady state data. Assuming that the first term is dominant, we find

$$\frac{M(p)}{M(p_o)} = 1 + \frac{(p - p_o)}{u_{a\ell"\ell}} \left.\frac{\partial u_{a\ell"\ell}}{\partial p}\right|_{p=p_o} = 1 + \alpha_a(p - p_o) \quad . \qquad (30)$$

The breathing mode parameter α_b of Eq. (27) is defined similarly to α_a of Eq. (30). Kubo's Eq. (4.12) is expanded to first order in pressure with the result (assuming ω^2 is pressure independent)

$$\alpha_b = (u_{b\ell"\ell"} - u_{b\ell'\ell'})^{-1} \frac{\partial}{\partial p}(u_{b\ell"\ell"} - u_{b\ell'\ell'})\Big|_{p = p_o} \quad .$$

Using Eq. (30), the pressure dependence of the lifetime is

$$\frac{\tau(p)}{\tau(p_o)} = \left[\frac{M(p)}{M(p_o)}\right]^{-2} = \left[1 + \frac{\alpha_a}{\alpha_b} \frac{(R - 1)\ (p - p_o)}{q_o\omega^2 R}\right]^{-2}$$

$$\simeq \left[1 - \frac{(1 - R)\ (p - p_o)}{q_o\omega^2 R}\right]^{-2} \qquad (31)$$

where we have assumed that $(\alpha_a/\alpha_b) \simeq 1$. Such an assumption will be shown to be consistent with the data, and will be more fully explained later in this section.

In Table 5 the change in lifetime over a 20 kbar pressure range (from p_o to p_o + 20 kbar) calculated from Eq. (31) is compared to the measured change. In the Cu^+-doped potassium halides, the theory consistently underestimates the lifetime increase in the fcc phase, and overestimates the change in the sc phase. Absolute agreement is only fair, but note that within each group of phosphors, the calculated values show the same trend as the measured values. Two anomalies are found in the table, KBr:Ag (fcc) and KCl:Ag (sc), for which graphs of lifetime vs. pressure are found in Fig. 21. The lifetime of KBr:Ag increases enormously from the atmospheric value [16], which was not predicted. Others have found that at room temperature and atmospheric pressure, the emission is quenched [63]. According

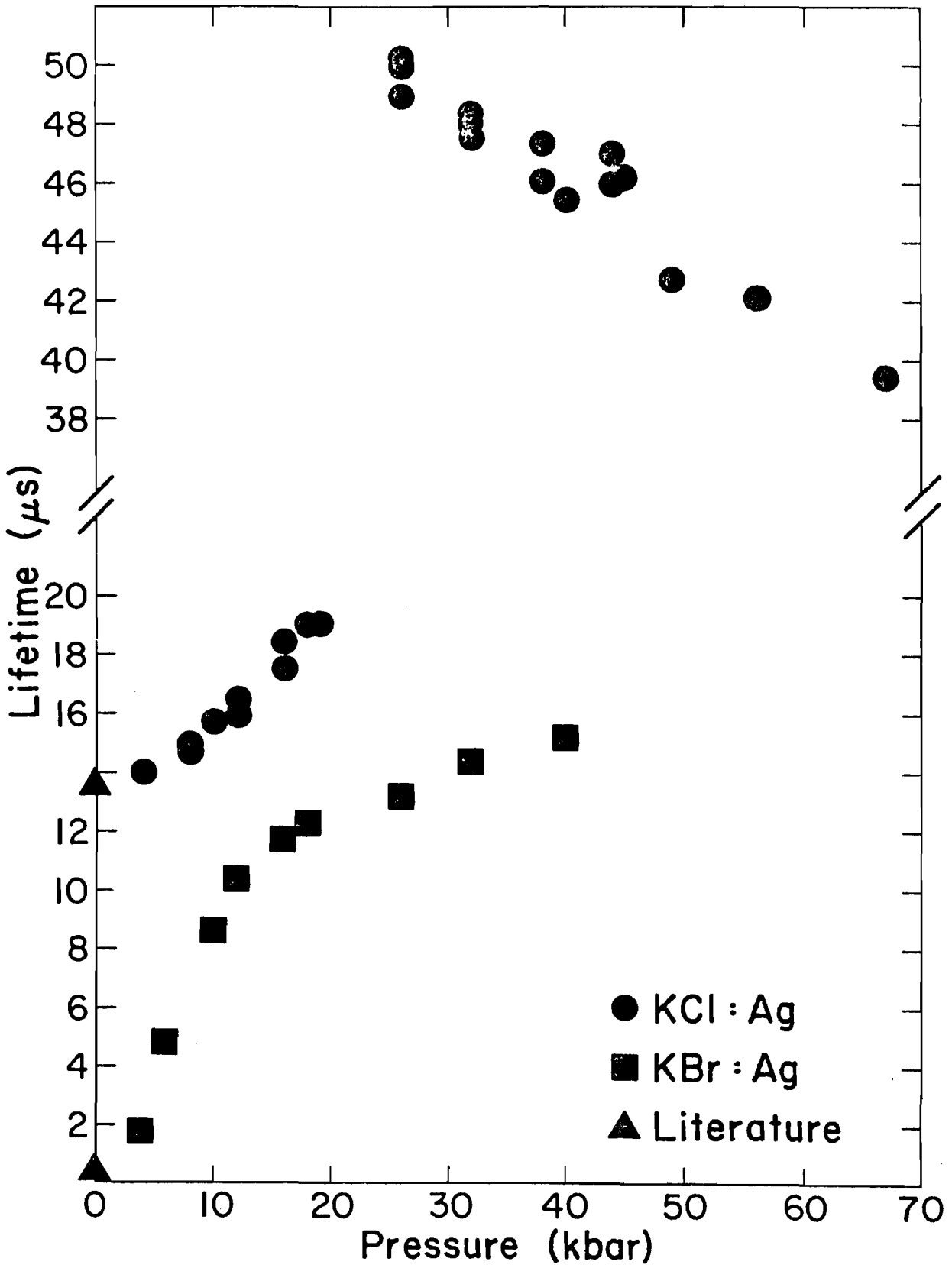

Fig. 21 Lifetime Change with Pressure for KCl:Ag and KBr:Ag

to steady-state data, as pressure rises, the wells move vertically so as to increase the quenching temperature, which would raise the lifetime. An extrapolation is made in Table 5 which brings the measured and calculated values into agreement. Potassium halides doped with Cu^+ were found to quench at 600° K [56], so that room temperature quenching does not appear to be common in these crystals. In the other anomaly, KCl:Ag (sc) is the only compound where τ decreases with pressure. A small decrease was predicted from the phonon-assisted theory, but it is interesting to note that the measured drop in τ is exactly predicted by Eq. (16). This equation ties the lifetime change to the peak shift, for a simple allowed transition.

There are a number of problems with the configuration coordinate model of a phonon-assisted transition (to be referred to as the Kubo theory), and a host of other theories that might explain the data. Some background is necessary before these can be discussed. Only recently have a number of luminescent studies featuring decay measurements appeared. The majority of research in noble metal-doped alkali halides has involved uv or ir absorption. The uv oscillator strength typically has the same temperature dependence as $1/\tau$ in Eq. (25). The odd phonon of frequency Ω that assists the transition is thought to be the T_{1u} resonant mode that dominates the ir absorption spectrum. In this mode, the nearest neighbors move one way, while the impurity ion moves in the opposite direction with large amplitude. One might not expect hydrostatic pressure to couple to such a nontotally symmetric vibrational mode, but the force constant of the T_{1u} mode in NaCl:Cu was found to nearly double in 6 kbar [52]. (The force constant Ω^2 should be linearly related to τ at room temperature through the mean square displacement $\langle Q^2 \rangle$ by [64]

$$\frac{1}{\tau} \propto \langle Q^2 \rangle = \frac{kT}{\Omega^2} \quad ,$$

so that the lifetime should increase with pressure. The increase is observed, though for NaCl:Cu τ certainly does not double in 6 kbar.) It is clear then that pressure couples to the T_{1u} mode. A measure of the coupling is the ratio (α_a/α_b) of Eq. (31), which must be approximately unity in order to achieve the consistent results of Table 5. From the definition of α, the ratio is unity if the logarithmic derivatives with pressure of u_{jmn} are equal for both normal modes j = a and b, independent of the electronic states m and n; that is, if the change with pressure of the electron-phonon interaction of a mode is proportional to the strength of the interaction, and the breathing and resonant modes have the same proportionality constant. That $\partial(\ln u_{jmn})/\partial p$ does not depend on the symmetry of the j^{th} mode is a surprising result that should be investigated further.

It has been theorized [65] (and confirmed in KCl:Li [52]) that the application of pressure, by decreasing the volume available to the substituted ion, will cause off-center to on-center transitions. At low temperature, such a transition would cause a large rise in the lifetime. However, on- and off-center ions have similar lifetimes at room temperature (e.g., the Cu^+-doped iodides [60]), and similar temperature dependences down to 100° K, so that the off-center effect does not dominate room temperature emission studies. (This is not true for absorption.) It can only explain the unusually large increase in τ with pressure in KI:Cu (fcc), which is off-center at atmospheric pressure and might be going on-center with pressure. It is not clear whether the potassium halide phase transition favors an on- or off-center position, since the lattice constant increases by 5% while the volume drops by 13% as the coordination number changes from 6 to 8.

Though the other compounds are on-center at room temperature, some exhibit off-center distortions at low temperature, so that the assumption of harmonic potential wells in the Kubo theory is not strictly true. In addition, the higher than linear terms in Eq. (24), which are sometimes necessary to describe the temperature dependence of τ [61], are not included in the Kubo theory. The Kubo theory predicts $\tau(p)$ to have an upward curvature, while the observed curvature is frequently downward. This discrepancy can be attributed to the linear approximation. Indeed, if there were no quadratic electron-lattice interaction, R would be one.

Another problem, more severe in Jahn-Teller studies (see part 4) is that the state to which the center is excited in absorption is not necessarily quite the same as the state from which emission occurs. The large values of q ($q_o/V \sim 20\%$) and large Stokes shifts ($> 10^4$ cm^{-1} for Cu^+-doped alkali halides) demonstrate this fact. Because of the increased volume of the relaxed excited state, an off-center position is only stable in KI:Cu, whereas in the ground state NaI:Cu and the Cu^+-doped potassium halides are all off-center. Thus the lifetime predicted from the oscillator strength can be orders of magnitude faster than the measured lifetime if an off- to on-center transition occurs upon excitation. Even when both ground and excited states are on-center, the optical transition can be 10-100 times more allowed in absorption than emission.

The configuration coordinate model, which considers two similar harmonic states, must therefore be employed cautiously. Model parameters were found from emission data, since equations using excitation or Stokes shift data yielded inconsistent parameters. This paper, then, is a pressure study of the excited state. With all its pitfalls, the configuration coordinate model produces reasonable and smoothly changing parameters (see

Table 5). And the Kubo theory, which incorporates these parameters, predicts lifetime changes with pressure that correlate with the measured changes.

One final problem with the configuration coordinate model introduces some alternative theories of the effect of pressure on lifetimes. For an allowed transition, the Condon approximation is generally made, setting $M(Q) \approx M_0$ in Eq. (28). This allows one to eliminate the Franck-Condon factors and arrive at Eq. (16). In this case, one cannot relate lifetime changes to changes in vibrational overlap integrals, as is sometimes done [35,55]. For a forbidden transition, however, the Condon approximation may be invalid, since M depends strongly on the odd coordinate Q. An equation was derived [21] to predict $\tau(p)$ for this case:

$$\frac{1}{\tau} = \frac{1}{\tau_0} \coth \frac{h\Omega}{4\pi kT} + \frac{M_1^2 p^2}{\omega^4} \quad .$$

Unfortunately, this predicts a decrease in τ, as does a consideration of Franck-Condon factors, whereas τ was found to increase with pressure.

In other theories, the effect of pressure on lifetimes is ascribed to shifting energy levels. If the lifetime in Cu^+-doped potassium halides is governed by a metastable level [66], pressure would change τ through the trap depth. However in the Ag^+-doped alkali halides, where there is no metastable level, the lifetime has the same pressure dependence. In another theory, the amount of configuration interaction (mixing) caused by odd phonons is determined solely by the energy difference between configurations. The lifetime is proportional to the square of the energy difference, which would change with pressure. There is no direct measure of energy differences in the relaxed excited state. One must rely on levels measured by absorption as a function of lattice constant [49,67],

since there is no pressure study of uv absorption. Then if the d^9s state mixes primarily with the d^9p state, τ would decrease with pressure, while if mixing with charge-transfer bands were predominant, τ would increase with pressure. One cannot place much faith, however, in such an extrapolation of absorption to emission and composition to compression.

In summary, we have shown here that the intrinsic radiative lifetime can change with pressure. Compression of the breathing mode couples to the odd phonon which assists the forbidden transition in Cu^+- and Ag^+-doped alkali halides. Steady-state emission measurements are interpreted by a configuration coordinate model, which predicts that pressure will decrease the phonon assistance. The measured lifetimes are found to increase, in agreement with the predictions. While the model has a number of limitations, other theories are found to be inadequate to explain the data.

4. JAHN-TELLER EFFECTS IN DOPED ALKALI HALIDE PHOSPHORS

1. Background, Theory, and Method

1.1 General Background and Theory

The Jahn-Teller effect is an example of a configuration instability which can exist in a non-linear molecule or complex. In general, a non-linear molecule or complex with electronic degeneracy (orbital or spin, but not Kramer's) will distort to remove as much degeneracy as possible. The resultant (perhaps instantaneous) reduction in symmetry will split the degeneracy of the electronic system, and stabilize one electronic state with respect to another, both of which were degenerate before the distortion occurred. This is a statement of the Jahn-Teller effect (JTE). Clearly the distortions which reduce the local symmetry are the non-totally symmetric ones; it is these which give rise to the JTE. Detailed descriptions of the Jahn-Teller effect in its many forms may be found in the review article by M. C. Sturge [68] and the monograph by R. Englman [69].

In this part we discuss the effect of pressure on Jahn-Teller (JT) split luminescence of heavy metal ions in alkali halides. The failure of a simple configuration coordinate model in describing the optical transitions of localized centers in heavy-metal doped alkali halides is essentially due to three interrelated effects. First, the assumption that a single configuration coordinate, the totally-symmetric A_{1g} coordinate, can describe the relevant electronic states is incorrect. Secondly, in the simplest description, the Born-Oppenheimer approximation cannot include electronic degeneracy. The p-like excited electronic state contains such electronic degeneracy.

Third, the Tl^+ ion has a large spin-orbit coupling parameter, and the ion's interaction with its environment must be treated in the intermediate coupling regime; the configuration coordinate description for localized states is intended to describe impurity or defect systems which couple fairly weakly with the host environment. These three conditions are important to a complete description of the electronic states of KCl:Tl-type phosphors.

The single CC model will be used only for schematic purposes, not to calculate parameters. As in Part 3, the effect of interest is due to an interaction between the impurity electronic system and nontotally symmetric lattice distortions. To visualize the effect of pressure (which couples primarily to the totally symmetric mode) on these systems, may be difficult, but the pressure effect is real and quite useful.

There are two major experimental observations which indicate the presence of Jahn-Teller interactions in the relaxed excited state from which luminescence occurs in heavy-metal doped alkali halides. First, Klick and Compton [70] observed that, at liquid helium temperatures, the luminescence from KI:Tl phosphors was partially polarized when excited with polarized A-band light. This implies that a static Jahn-Teller distortion occurs at low temperatures. The polarization of the exciting light is partially transferred to the emitted light through the lattice distortion. These polarized emission studies showed that the distortions were tetragonal. Second, it was observed by Edgerton and Teegarden [71] that A-band excitation in KBr:Tl and KI:Tl results in an emission doublet. Since that study, the emission doublet from A-excitation has been observed at various temperatures in a number of the NaCl-structure alkali halides, doped with Tl^+, In^+, Ga^+, Sn^{++},

and Pb^{++}, all of which have outer electron configurations (ns^2). A review of the temperature phenomenology of the doublets in the various materials is given by A. Fukuda [72].

In 1970, Fukuda [72] gathered the known experimental evidence relating to the emission structure in the KI:Tl-type phosphors, and examined these data in terms of the various theoretical explanations which had been advanced. He proposed a model which described most of the observed features of the luminescence excited in the A-band. This model predicts the coexistence of two types of minima on the $^3T_{1u}$ excited state adiabatic potential energy surface (APES) in the subspace of tetragonal lattice distortions. (The designation $^3T_{1u}$ is the symmetry representation of the molecular orbital description for the $^3P_1$ electronic state.) The coexistence of the two minima is a result of both the JTE and the spin-orbit interaction, which may be rather large for Tl^+ (Z=81).

These minima lead to an emission doublet, which can be resolved into two bands, labelled A_T (high energy) and A_X (low energy). The so-called T-minimum on the excited state APES represents a tetragonal lattice distortion and results in the A_T emission band. The A_X emission is from the (doubly-degenerate) X minima, which are probably of rhombic symmetry (nearly tetragonal). The complicated temperature dependence of these bands is discussed by Fukuda. Luminescent lifetimes of the two bonds can be quite different. There have been a number of lifetime studies at atmospheric pressure [72-75]. As several temperature regimes are involved, the temperature dependence of the decay can be quite complicated.

Fukuda's original model has been extensively modified by Ranfagni, Viliani, et al. [76-82]. Initially, they correctly pointed out the

inadequacy of RS coupling, and the importance of intermediate spin-orbit coupling. Their later works extended the treatment to include quadratic Jahn-Teller interactions and anharmonicity [78,82]. Strong differences in curvature of the surfaces may exist between the T and X minima, as well as between the ground and excited states. Another result of the quadratic JTE is the prediction that both T and X minima can be accompanied by a trap level (essentially due to the $^3P_0$ free ion level of symmetry representation A_{1u}). This trap has important effects on the emission lifetimes.

Drotning [83] performed an extensive high-pressure study of the spectral properties of JT-split systems. Independently Fukuda [84] has published KI:In spectra taken at hydrostatic pressures to ten kbar, in agreement with Drotning's quasi-hydrostatic and hydrostatic results. Niilisk [85] has measured lifetimes in KBr:In and KI:In hydrostatically to 6 kbar, confirming the quasi-hydrostatic results presented here.

Drotning found that peak X dominates the spectrum at low pressures. However, the T peak grows in with pressure until at high pressures only the T peak is seen. Since excitation is to the T minimum Drotning explained his result in terms of the barrier between the T and X minima. At low pressure, he postulated, the barrier is small, allowing emission from the more stable X minimum. At high pressure, the barrier height is high enough to freeze the excitation in the T minimum.

The barrier model explains the room temperature intensity measurements performed by Drotning. Typical of these data are those in Fig. 22. Here the fraction of emission intensity in the low energy X peak (to be referred to as "%X"), is plotted versus pressure. The low energy fraction invariably

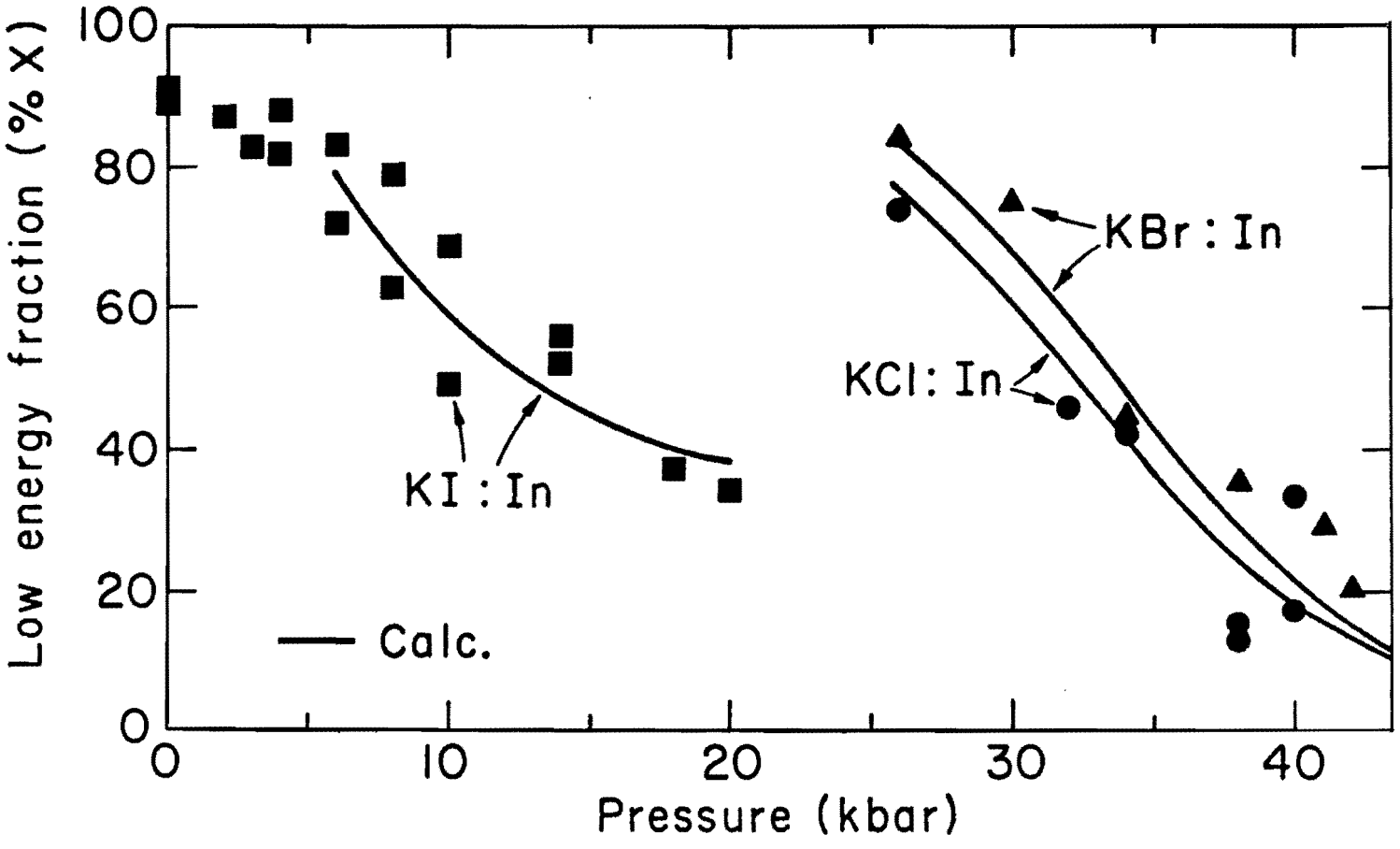

Fig. 22 Fraction of Emission in Low Energy Peak of Indium-doped Potassium Halides at Room Temperature vs. Pressure. Drotning's Points and Curves Calculated from Independent Data Presented Here.

drops with increasing pressure. The calculated curves through Drotning's points are, however, derived from a different model that will be presented here.

After the pressure work appeared, theorists began to take the A_{1g} breathing mode into account [82,86] by an arbitrary coupling to the non-totally symmetric modes. Thus one can draw the cross section of the excited state surface along the A_{1g} coordinate as two wells with minima at different Q. The assignment of symmetry and degeneracy to the wells and their associated traps is more than ever in dispute, and it appears to this author that there is no one general assignment that can explain all the data, particularly the data presented here.

1.2 Experimental Method

Since the work of Drotning, which involved only room temperature spectra, two techniques have been developed that enable a more thorough investigation of the effect of pressure on Jahn-Teller splitting. These are low temperature (100 to 300°K) optical studies [25] and lifetime measurements. Both new methods are described in Part 2 of this thesis.

A typical low temperature (LT) spectrum of an In^+-doped compound (KCl: In at 31 kbar) is shown in Fig. 23. Tl^+-doped compounds have similar spectra, as seen in Fig. 24 (KBr:Tl at 4kbar). The two Tl^+ peaks are generally closer in energy than the two In^+ peaks, and the difficulty in resolving them made an LT spectral study of Tl^+-doped compounds (other than KBr:Tl) impractical. In both figures, the low energy (X) peak gains at the expense of the high energy (T) peak as the temperature drops. As we will

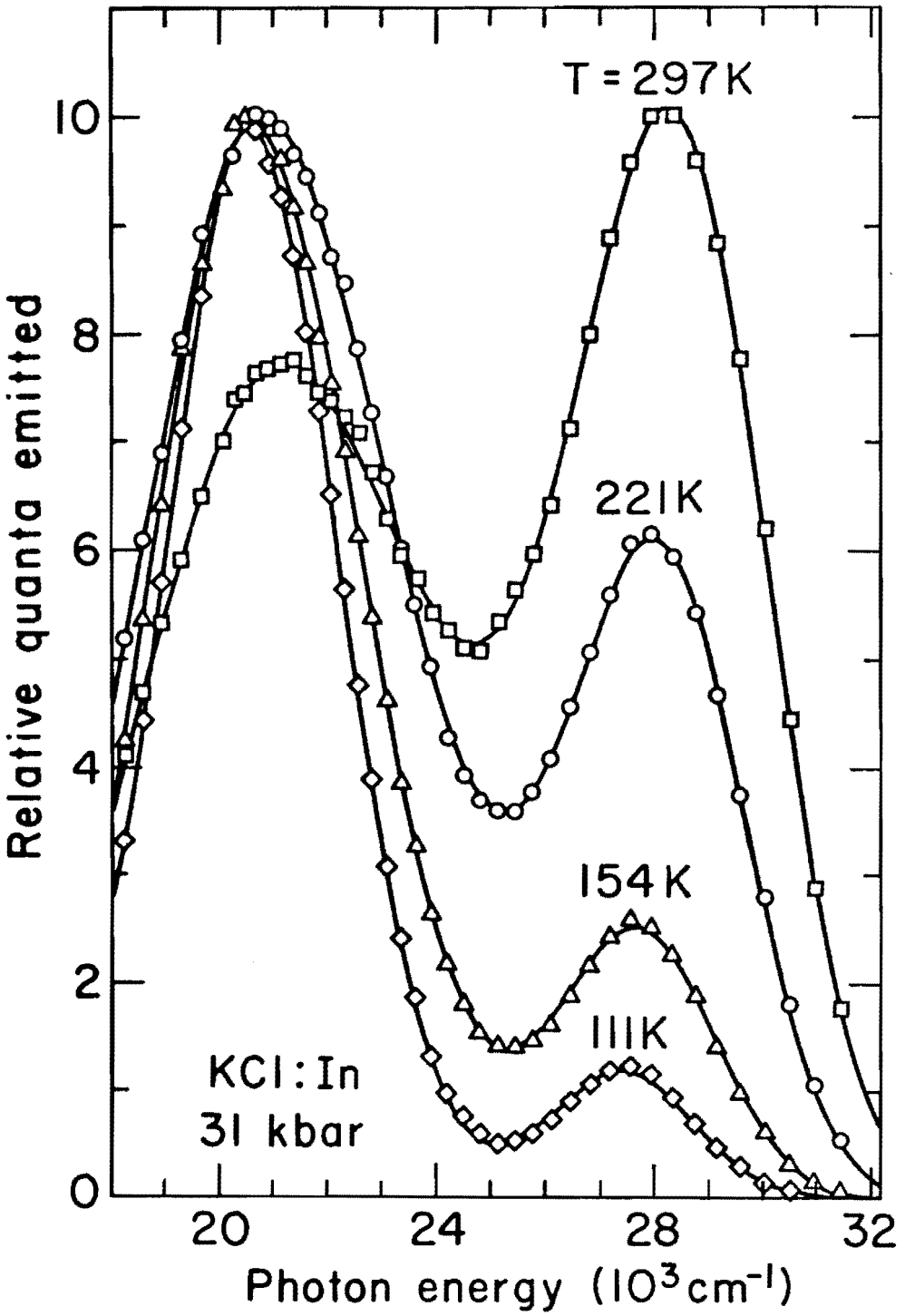

Fig. 23 Spectrum of KCl:In at 31 kbar for Several Temperatures

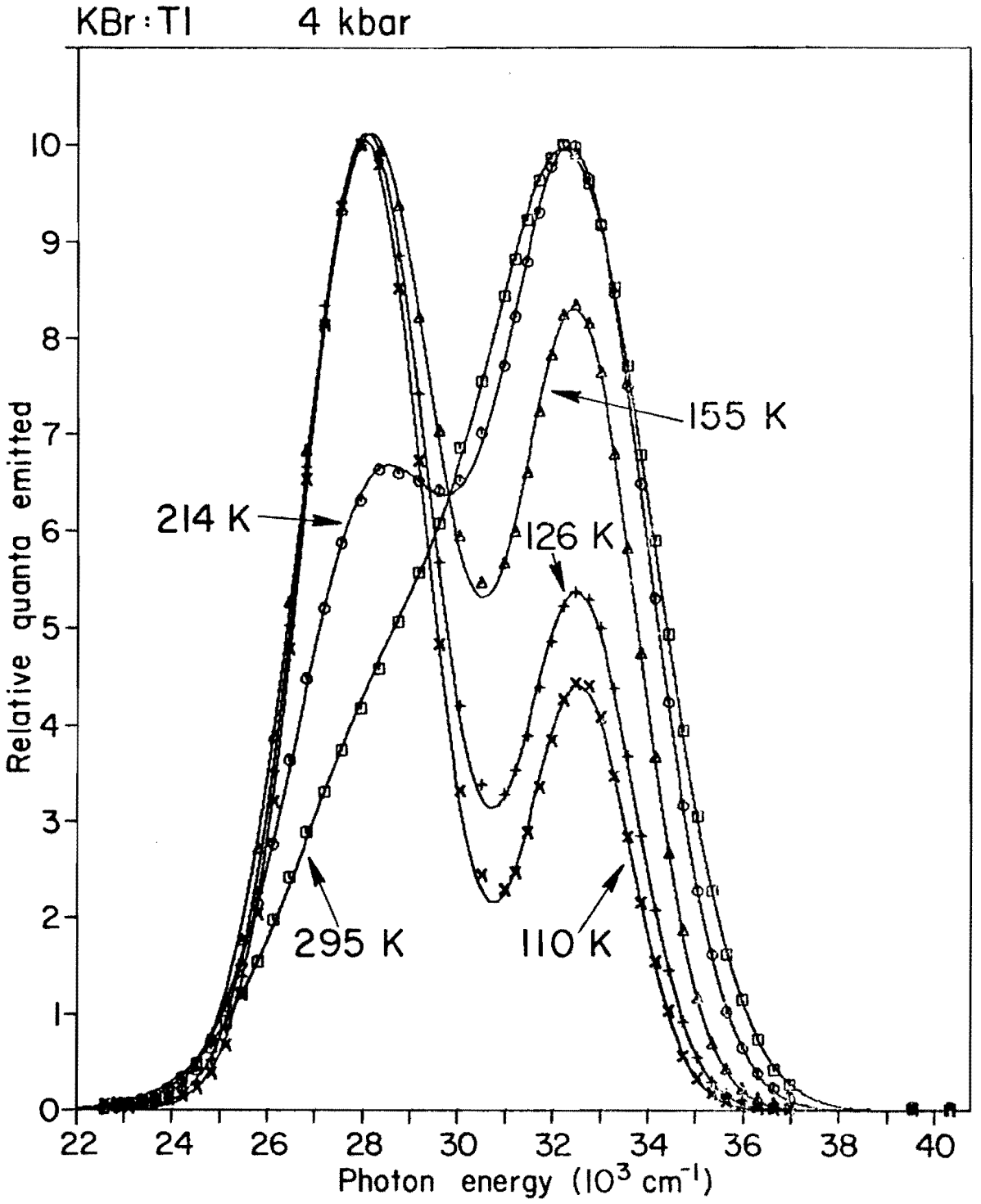

Fig. 24 Spectrum of KBr:Tl at 4 kbar for Several Temperatures

show, this occurs simply because the X level is lower in energy than the T level at these pressures.

The procedure for taking and analyzing spectral data was explained in Part 2, but methods specific to this study will now be enumerated. In order to resolve the two peaks well, the slit width of the emission monochromator was set smaller than usual. Resolution was typically set at the wavelength spacing between data points. For instance, in Fig. 23, it was about 400 cm^{-1}, while for the spectrum of Fig. 24, instrumental resolution was about 200 cm^{-1}.

Cell I was used for all steady state runs, and only low temperature work was done, since Drotning had taken the room temperature (RT) measurements. The temperature was reduced along an isobar, and great care was taken to maintain a constant pressure, since the JT properties are very pressure-sensitive. Each spectrum was taken at a constant temperature, within at most ± 2°K. Excitation was by Hg line, which was also used to align the grating for each run. A small wavelength shift could result in a substantial change in the ratio of the two peak's areas, after the spectral correction was applied. The computer program SKEW can shift all the wavelengths of a curve by a given amount, and this was occasionally used to correct for a misaligned grating after the fact. Specifically, for KBr:In and CsI:Tl, all the spectra at a given pressure were shifted the same amount in wavelength, until the RT peak shift with pressure agreed with Drotning's. For the other compounds, the wavelength shift was unnecessary or insignificant. The peak shift and halfwidth change with temperature were monitored. These contain little useful information for us.

(Peaks shift slowly to lower energies and halfwidths decrease as the temperature drops.) However, the quality of the fit could be evaluated by using these parameters. Often one peak was much smaller, lying on the shoulder of the other, which caused the ratio of areas to be disturbed by an artifact of the fitting process. Then by varying the background and skewness within small limits, the plots of peak position and halfwidth change versus temperature were brought into line with each other. This procedure was followed for all five compounds studied here, but only for KBr:In was there enough change in the final parameters to warrant using the skewed fits. For KBr:In, then, the peaks are fit by Gaussians with skewness $|b|<.1$. All the other peaks are symmetric Gaussians, except for peak 3 in CsI:Tl, which is heavily skewed because of quadratic coupling, not because of an artifact [23].

Low temperature spectral studies tell us about the size of the JT level splitting. The ratio of peak areas is regulated by a Boltzmann factor that depends on the splitting. In Drotning's barrier model, X emission always rises with increasing temperature, since the barrier to X emission can be more easily overcome at higher temperature. We have just seen in Figs. 23 and 24 that this is sometimes not the case; the model proposed here has a Boltzmann factor dependent not on a barrier height but on the level splitting.

The other new technique is the measurement of lifetimes. In conjunction with LT studies, lifetimes versus pressure can determine the level degeneracies and the radiative rates of the two states. Measurements of lifetimes versus temperature provide checks of the parameters already derived or, when there are nonemitting levels, determine trap depths.

All decay curves were single exponential, except when traps appeared. In that case, there is a nonequilibrium fast component of exceedingly short lifetime; the fast component was blocked during data-taking (see Part 2), and the slow component was fit with a single exponential. All lifetimes for the Tl^+-doped compounds were taken by the single photon counting (SPC) method. Both SPC and transient digitization were used for the In^+-doped compounds, the latter method not below 1 μsec. The two methods gave the same lifetimes within 20%. When either method could be used, SPC was usually preferred as it is comparatively foolproof. SPC lifetimes were always corrected [45] for "double photons." Because most of the decays were faster than 20 μsec, the spark gap was used exclusively in this JT study. The shortest lifetime measured was 180 nsec, which is well over the shortest measurable lifetime (120 nsec). Fig. 25 shows a typical decay curve (KI:In at 15 kbar and RT) taken by the SPC method and corrected.

1.3 Analysis

Decay curves (except at very low temperature or when traps appear) are the same for both emission peaks. That, with the fact that they are single exponentials, implies that the two levels are in "dynamic equilibrium" (in quotes because an excited system cannot be in true equilibrium). In words, rearrangement of excitation between the two levels is much faster than de-excitation. Therefore decay measurements, as well as LT studies, indicate that there is no thermal barrier to X emission.

If there is no thermal barrier, the population ratio (n_T/n_X) of the two states (where n is the occupation of a state) is simply given by a Boltzmann factor involving the level degeneracy g and the splitting $\Delta E = (E_T - E_X)$:

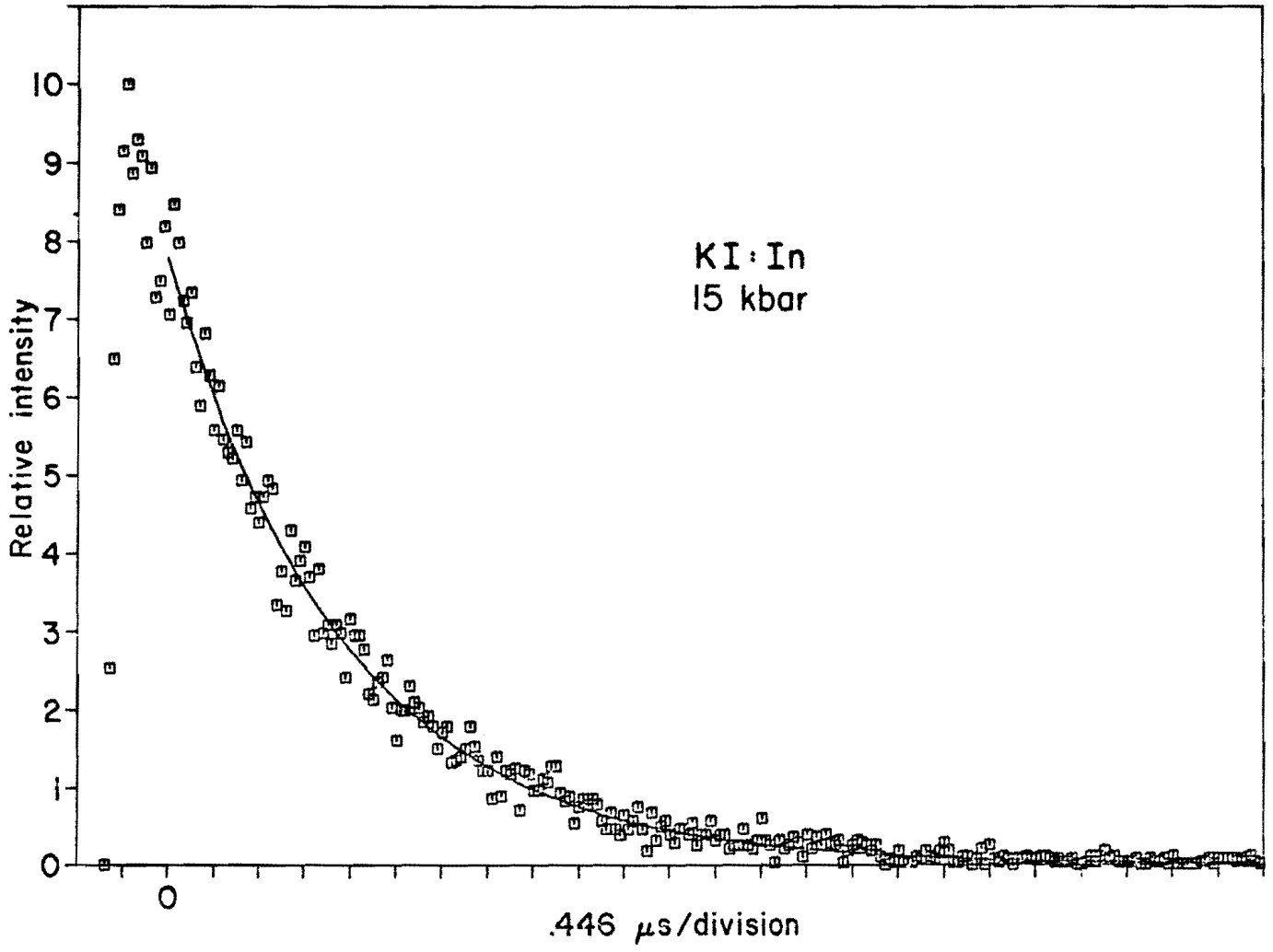

Fig. 25 Typical Decay Curve from Single Photon Counting Apparatus (KI:In at 15 kbar)

$$\frac{n_T}{n_X} = \frac{g_T}{g_X} \exp \frac{-\Delta E}{kT} = K \quad , \tag{32}$$

where k is Boltzmann's constant. K is not a constant, but a function of temperature and pressure (through ΔE). If N is the total excited population ($n_T + n_X$), it is easy to show that

$$n_X = N(1 + K)^{-1} \qquad \text{and} \qquad n_T = N(1 + K^{-1})^{-1} \quad . \tag{33}$$

De-excitation is from both levels:

$$-dN/dt = n_X k_X + n_T k_T \ , \tag{34}$$

where k_X and k_T are radiative rate constants intrinsic to each level ($k_X^{-1} = \tau_X$). Combining Eqs. (33) and (34), we find that the time derivative of N is proportional to N; that is, the decay curve is a single exponential for both peaks:

$$-\frac{dN}{dt} = \left[\frac{k_X}{1 + K} + \frac{k_T}{1 + 1/K} \right] N \quad . \tag{35}$$

The quantity in brackets is the inverse measured lifetime τ; simplifying, we find

$$\tau = \frac{1 + K}{k_X + K k_T} \quad . \tag{36}$$

If, as one hopes, the intrinsic rates k_X and k_T are constant, the temperature and pressure dependence of the lifetime is contained only in K.

In a similar manner, one can solve for the ratio of steady state peak areas. This ratio is expressed here (and by Drotning) as the low energy fraction, %X,

$$\%X = \frac{I_X}{I_X + I_T} = \frac{n_X k_X}{N\tau^{-1}} = \left[1 + \frac{k_T}{k_X} K\right]^{-1} , \qquad (37)$$

where I denotes intensity. Again, the temperature and pressure dependence of %X is contained in K. Decay and steady state measurements are linked by Eqs. (36) and (37) and therefore one measurement can predict the other.

In room temperature (RT) studies, Drotning proved that an X-dominated spectrum invariably becomes T-dominated at higher pressures (unless, say, a phase transition intervenes). He postulated that the T level was stabilizing with respect to the X level. We retain this postulate, as shown in Fig. 26, and extend it to argue that the T level actually drops to a lower energy than the X level at high pressure. The evidence, which will be shown later, is that at high pressure, %X drops as the temperature is lowered.

The schematic of Fig. 26 shows the excited state with a larger volume than the ground state, as found by Drotning. Excitation from the ground well bottom is to the T state (as is known from ultra-LT studies), and emission is from both excited wells, with peak energy maxima, $h\nu_T$ and $h\nu_X$. Due to the Stokes' shift as illustrated in Fig. 26, $(h\nu_T - h\nu_X)$ is on the order of 5000 cm^{-1}. The T-X level splitting is minute in comparison (less than 500 cm^{-1}), so that even when the T level is lower than X level, the T emission is at higher energy.

Note that ΔE is defined as $(E_T - E_X)$, which is negative at high pressure. By Eq. (32), then, K can vary from about zero to very large as the pressure is increased. At some pressure p_0, $\Delta E = 0$ and the levels are no

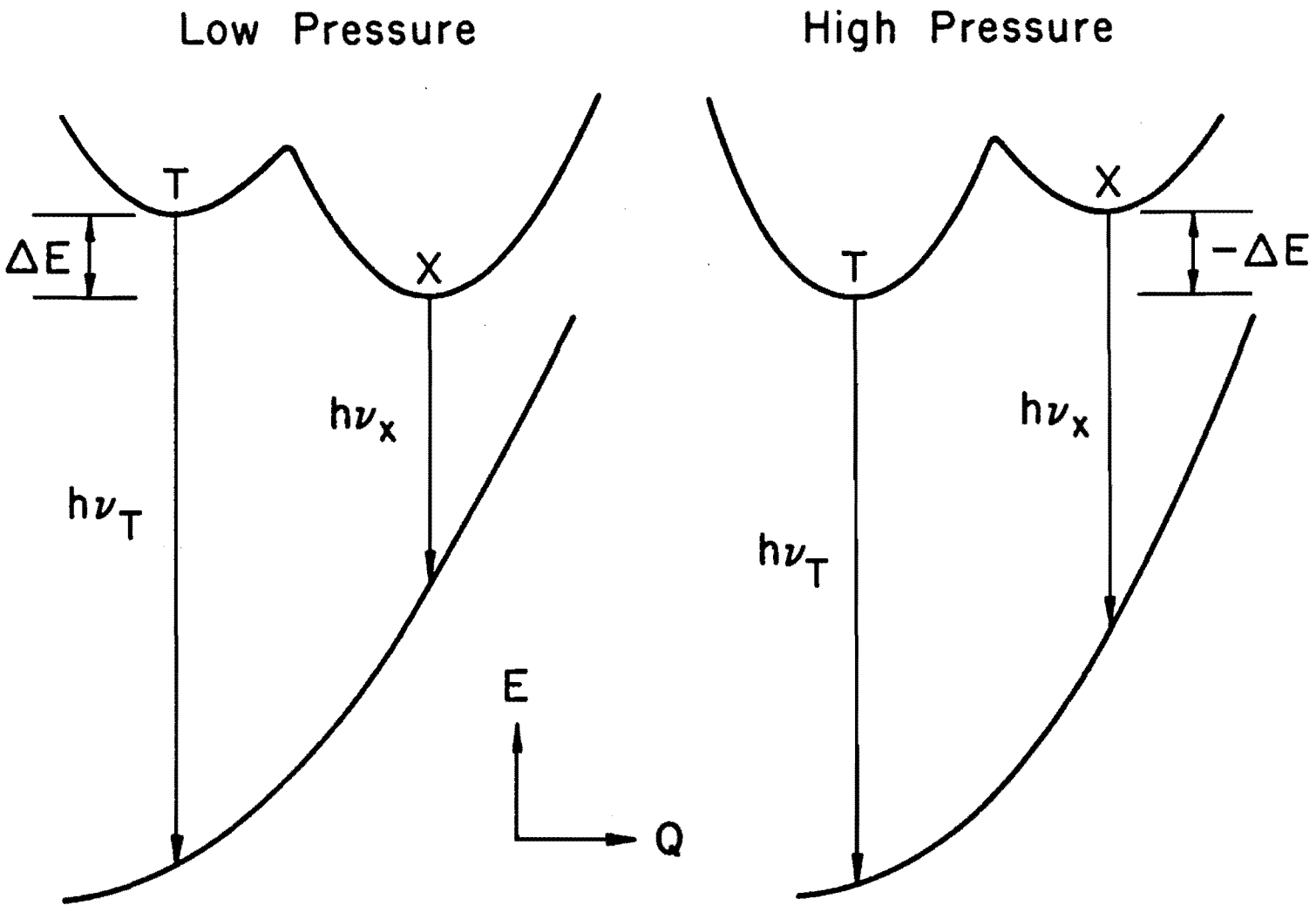

Fig. 26 Schematic Diagram of Jahn-Teller Split Excited State at Low and High Pressures

longer split. By Eq. (32), K is g_T/g_X and the temperature dependence disappears from the equations for τ and %X, at this pressure. A good check of the theory and assumptions on which it rests, is to measure τ (p_0) and %X (p_0) as functions of temperature to prove that they are constant. This was done with good results, as will be shown.

Let us examine the limiting behavior of Eqs. (36) and (37). As pressure increases at room temperature, K can vary from zero (at low pressure) to infinity (at high pressure). Then at low pressure, $\tau = \tau_X$ and %X = 1, while at high pressure, $\tau = \tau_T$ and %X = 0. Drotning already found that %X drops from one to zero. It will be shown that the lifetime does vary (in fact drop) from τ_X to τ_T as pressure rises.

The behavior of K with temperature depends on ΔE. At pressures below p_0, ΔE is positive, so K rises with increasing temperature. Then by Eq. (37), %X drops as the temperature rises (as in Figs. 23 and 24). At p_0 K is constant with temperature, and so are τ and %X. Above p_0, ΔE is negative and K drops with increasing temperature. Then %X actually rises with the temperature. The behavior of the lifetime depends on the ratio k_T/k_X, but since k_T was greater than k_X throughout this study, it turns out that below p_0, τ drops, while above p_0, τ rises, as temperature increases. This kind of limiting behavior with temperature and pressure predicted by the theory is seen in all the In^+-doped potassium halides (KH:In).

The assumptions behind the theory are as follows: 1) There is "dynamic equilibrium," which is supported by decay measurements. 2) The barrier height between the T and X states is negligible in our temperature range. Fukuda [72] claims that the barrier generally becomes important only below

about 80°K. In KBr:In and CsI:Tl, strange LT (below 130°K) behavior in our data (see Appendix G) could be due to barrier effects. 3) The excited system consists of just two emitting states. Trap levels, nonradiative de-excitation, and three-peak phosphors will be taken up in the section on Tl^+ compounds (section 2.2). 4) The splitting ΔE is constant with temperature. 5) Intrinsic radiative rates k_X and k_T, and level degeneracies g_X and g_T are constant with temperature and pressure.

These assumptions turned out to hold true for the three indium-doped potassium halides tested. Indirect proof lies in the fact that the model is in excellent agreement with the data. Experiments to test the assumptions directly were also performed; these will be noted at the end of section 2.1. It has been refreshing to work on a project where pressure affects only one variable (ΔE), which is orthogonal to temperature. To be able to say almost without reservation that the assumptions hold true and that the theory explains independent sets of data (without forcing) is unusual in high-pressure experiment.

Before the data are displayed, the method of presentation that best fits the theory must be decided. The major steady state measurement is that of low energy fraction %X versus temperature. Eq. (37) gives its theoretical variation, which can be rearranged as

$$\log[(1/\%X) - 1] = -\Delta E \log e \, (kT)^{-1} + \log \left[\frac{g_T k_T}{g_X k_X}\right] , \qquad (38)$$

where log means common log. If the quantity on the left is plotted against $(kT)^{-1}$, a straight line of slope $(-\Delta E \log e)$ and intercept $\log (g_T k_T / g_X k_X)$

should result. Such a graph (which, like an Arrhenius plot, decomposes the Boltzmann factor) will be called a "steady state plot." If assumptions one to five are true within a particular crystal phase, lines at different pressures will meet at a common intercept, and their slopes will increase systematically with pressure as ΔE drops. When $\Delta E = 0$ at p_0, the line is horizontal. The equations derived to this point are collected in Table 6.

The procedure is to take LT data at several pressures and draw a steady state plot. Lines having a common intercept are drawn (by eye) through the data. The slopes show what ΔE is as a function of pressure, and by interpolation, which pressure is p_0. The intercept gives the ratio of degeneracies times the ratio of intrinsic radiative rates of T to X. The literature is divided on the subject of degeneracy assignments, so the g values that best fit the lifetime data are used.

If the degeneracies are known, the intercept of the steady state plot gives the ratio of intrinsic radiative lifetimes. Then one need only determine either τ_X or τ_T to know the other. At RT, one can go to very low pressure, where $\tau = \tau_X$, or very high pressure, where $\tau = \tau_T$. If the extreme pressure where emission is pure X or T cannot be reached at RT, it can often be reached at LT. With k_X and k_T determined, and ΔE (p) known from a steady state plot, one can use Eq. (36) to generate curves τ (p) and τ (T) corresponding to the three most likely degeneracy assignments (g_X/g_T = 2, 1, or .5). One of these three sets of curves will typically fit the data much better than the other two, so that the degeneracy assignment is obvious. Finally, a curve %X (p) is generated from Eq. (37), and fit to Drotning's completely independent data as in Fig. 22. If the model predicts all four

Table 6

Equations for a Two Level Jahn-Teller System

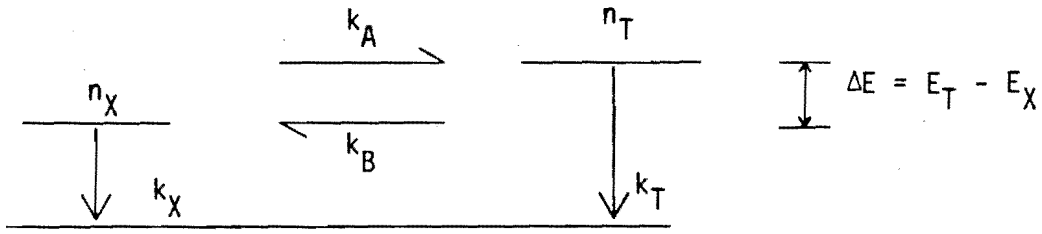

"dynamic equilibrium": $k_A, k_B >> k_X, k_T$

$$\frac{k_A}{k_B} = \frac{n_T}{n_X} = \frac{g_T}{g_X} \exp(-\Delta E/kT) = K$$

$$\frac{1}{\tau} = \frac{k_X + Kk_T}{1 + K} \qquad \%X = \frac{1}{1 + Kk_{T/k_X}}$$

$$\log[(1/\%X) - 1] = -\Delta E \log e\,(kT)^{-1} + \log\left(\frac{g_T k_T}{g_X k_X}\right)$$

sets of data %X (T), %X (p), τ (T), and τ (p) within reasonable accuracy, one can be confident that one has the right set of parameters g_T, g_X, k_T, k_X, and ΔE (p).

2. Results and Discussion

2.1 Indium-doped Potassium Halides

The two level "dynamic equilibrium" model was applied (following the procedure just described) to sc KCl:In, sc KBr:In, and fcc KI:In, with very good results. KCl:In is probably the best example, so application of the model to KCl:In will be fully explained, and any differences for KBr:In and KI:In will be mentioned.

Fig. 27 shows a steady state plot of sc KCl:In. The abscissa is $(KT)^{-1}$ in units eV^{-1}. Temperature (°K) is given at the top of the plot. The ordinate is $\log_{10}$ [(1/%X) - 1]; for reference, the values of %X corresponding to ordinate marks will be given: (1.2, 6%), (.8, 14%), (.4, 28%), (0, 50%), (-.4, 72%), (-.8, 86%), and (-1.2, 94%). Measurement of %X<15% or 85%<%X is difficult because of small peaks. Therefore the steady state plot can only contain data from pressures close to p_0, for which %X does not reach extreme values at low temperatures. Because of the strong dependence of ΔE on pressure (reflected in the swiftly increasing slopes of Fig. 27), great care was taken in setting the pressure. A steady state plot such as Fig. 27 would be difficult at pressures above 44 kbar, where Cell II (in which pressures are less accurate) must be used. This was not attempted.

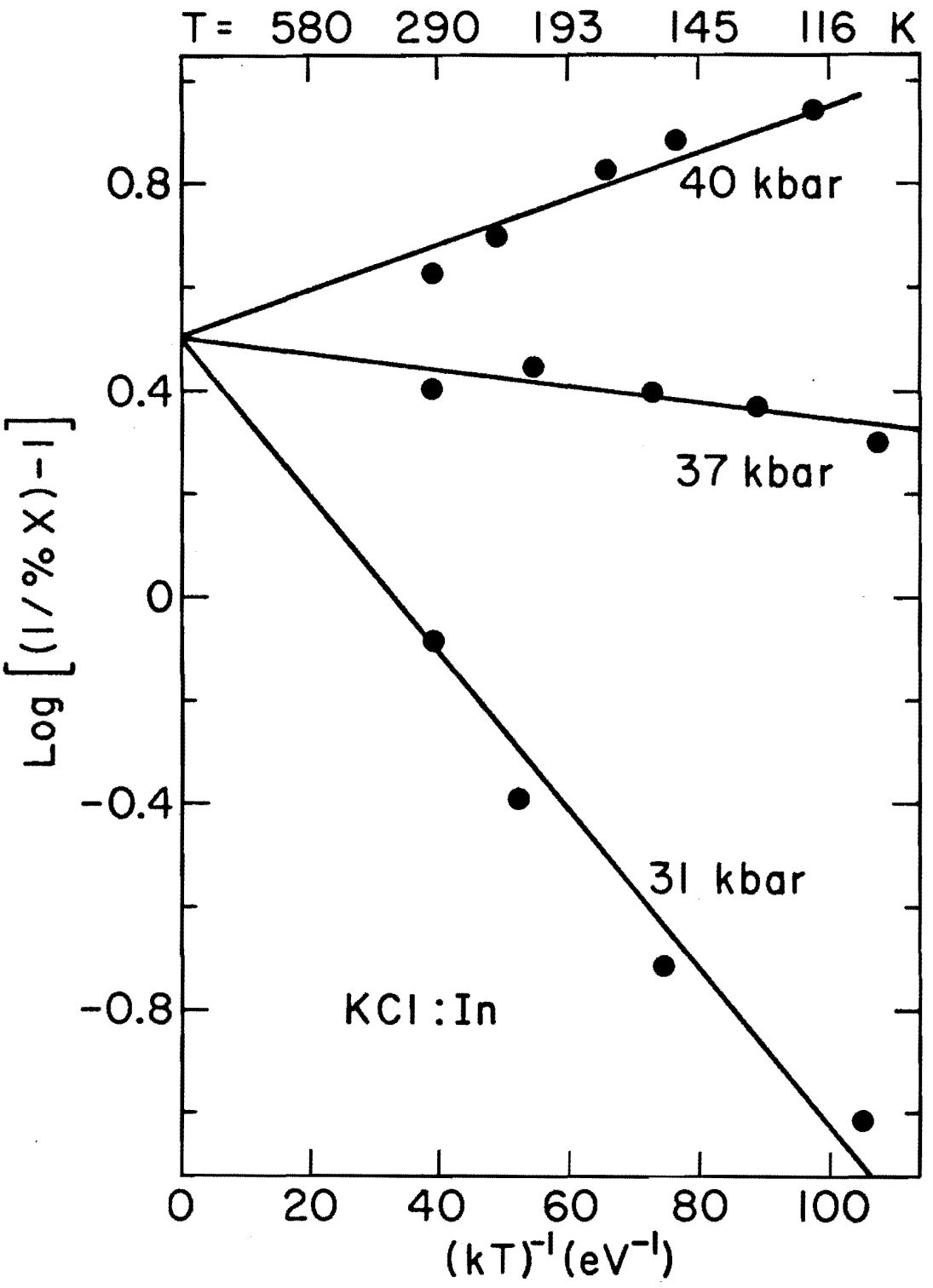

Fig. 27 Steady State Plot of KCl:In Above the Phase Transition

Some lifetimes were measured in Cell II, but only to find the asymptotic value of τ at high pressure. Such a case is shown in Fig. 28, a graph of the room temperature lifetime versus pressure.

From Fig. 27 are found the level splittings ΔE at three pressures (see Table 7). Splittings are on the order of tens of milli-electron volts or hundreds of wavenumbers. The three values of ΔE are fit with a line, giving an equation for the function ΔE (p). The pressure p_0 at which $\Delta E = 0$, is found to be about 38 kbar, where %X = 24% (as calculated from the intercept). From the intercept (.5), $(g_T\tau_X/g_X\tau_T)$ is found to be 3.16. Since at high pressure, τ (p) levels off to about one μsec (see Fig. 28), and at lower pressures the lifetime rises higher than 3.16, it is clear that $g_X/g_T = 2$. Then $\tau_T = 1$ μsec and $\tau_X = 6.32$ μsec (see Table 8). If sc KCl:In extended below the phase transition at about 20 kbar, τ (p) would presumably level off at 6.32 μsec, giving a sigmoid-type curve.

These values for k_X, k_T, g_X, g_T and ΔE (p) were inserted in Eq. (36) and the curve in Fig. 28 was generated. This curve is not a fit to the data, but a calculation based mainly on parameters from the steady state plot. Discrepancies can be attributed to some uncertainties in k_X and k_T and especially the linear approximation to ΔE (p). Since ΔE was measured only at 31, 37, and 40 kbar, the agreement between theory and experiment as low as 26 kbar and as high as 52 kbar is surprisingly good.

Fig. 29 shows data for τ (T) in KCl:In, along with calculations from the model. Agreement between experiment and calculation is good at 31 kbar. At higher pressures, it can be seen from Fig. 28 that the model overestimates the lifetime (ΔE (p) may drop faster than the linear approximation allows)

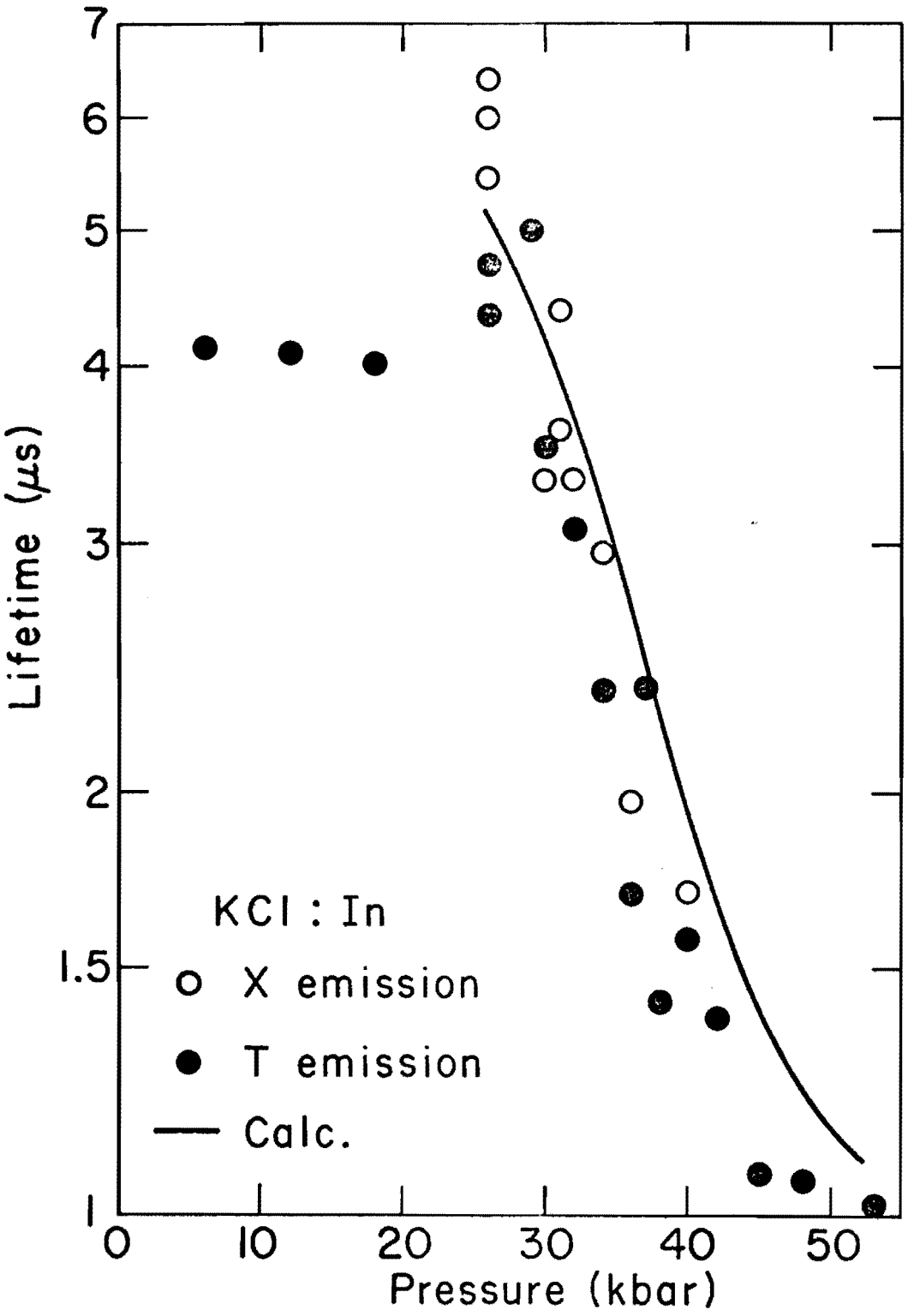

Fig. 28 Lifetime Change with Pressure for KCl:In at Room Temperature

Table 7

Jahn-Teller Level Splitting (ΔE) as a Function of Pressure

Compound	Pressure (kbar)	ΔE (meV)
KCl:In	31	35
	37	3.7
	40	-10.1
KBr:In	34	43
	37	21.0
	40	6.9
	43	-5.6
KI:In	6	66
	10	42
	15	27.5
	20	20.0
KBr:Tl	4	24.9
	10	-4.4
CsI:Tl	32	38.5
	37	16.1

Table 8

Measured Jahn-Teller Parameters

Crystal	Structure	$\log\left[\frac{g_T\tau_X}{g_X\tau_T}\right]$	τ_X(μsec)	τ_T(μsec)	g_X/g_T	p_0(kbar)[c]	%X(p_0)[c]	$\tau(p_0)$[c]
KCl:In	sc	.5	6.32[a]	1.0	2	38	24	2.28
KBr:In	sc	.72[a]	4.37	.837	1	42	16	1.40
KI:In	fcc	.55	2.9	.82[a]	1[b]	>20	22	1.28
KBr:Tl	fcc	.7	.10	.010	2[b]	9	17	
CsI:Tl	sc	.87	τ_2/τ_3 = 7.4		1[b]	41	%2 = 12	

[a] This one of the three [τ_X, τ_T, or log ($g_T\tau_X/g_X\tau_T$)] was calculated from the two that were measured.

[b] Degeneracy assignment is not certain.

[c] Calculated from Eq. (36) or (37).

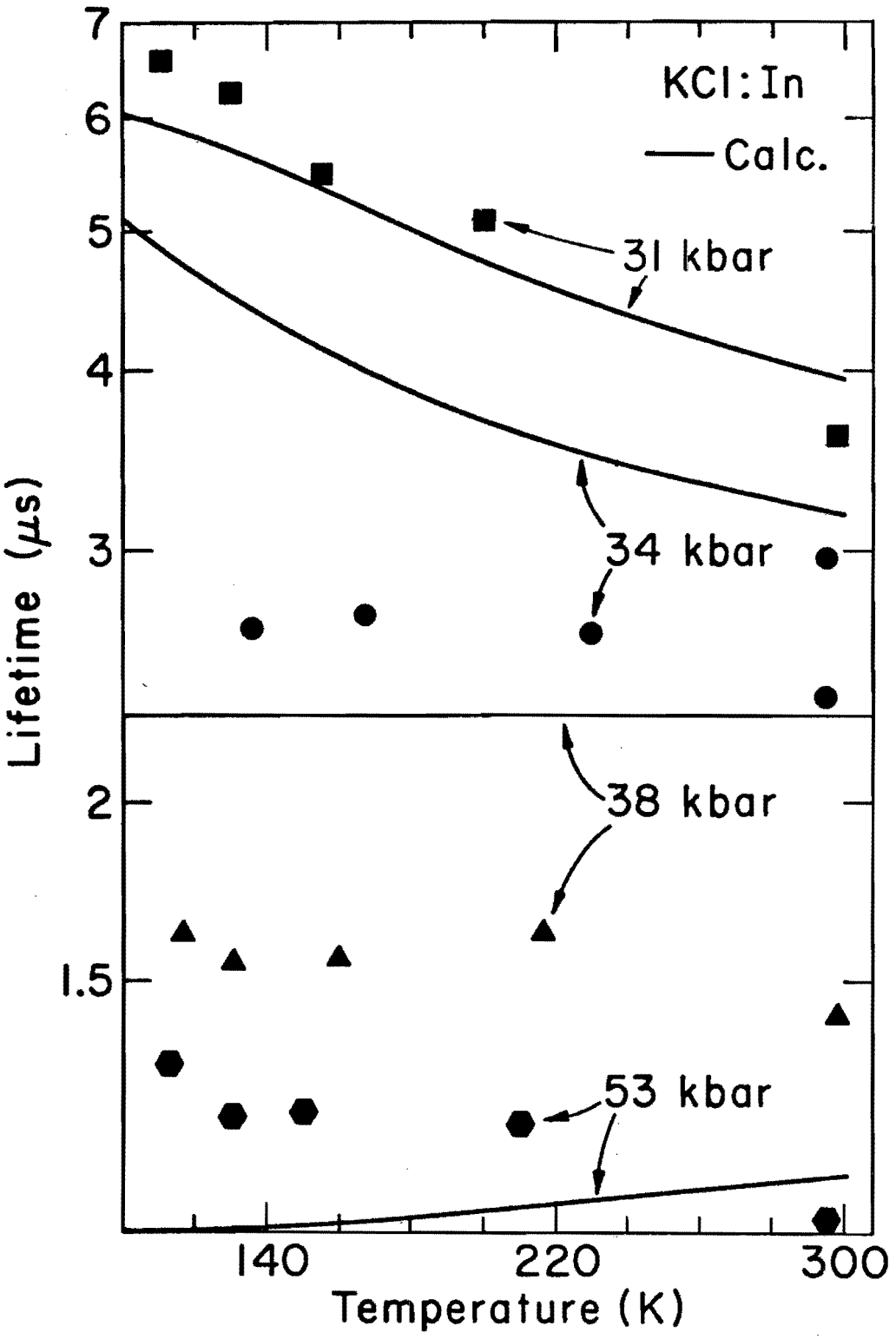

Fig. 29 Lifetime Change with Temperature for KCl:In at Several Pressures

at room temperature. Therefore, the calculated τ (T) will be offset at lower temperatures as well. At 34 kbar, agreement between theory and data is not good, and in addition, at the lowest temperatures, the lifetime of peak X becomes much longer than that of peak T (see Table G7). Apparently, the barrier effect appears.

Since p_0 = 38 kbar, one expects τ (T) to be constant at 38 kbar; the data points do lie on a horizontal line which is a direct confirmation of the assumptions behind the theory. Also, at a pressure as high as 53 kbar, one expects τ (T) = τ_T to be constant. In fact, τ (T) rises 30% as the temperature drops, for unknown reasons. The assumption that τ_T is constant with temperature is thus good to 30%, which is small compared to changes induced by the JTE.

Other assumptions of the model are clearly confirmed for KCl:In in Fig. 28. Below the phase transition, Drotning found only one emission peak (T). Since the JTE plays no part in emission from fcc KCl:In, one expects the lifetime to be constant with pressure. In Fig. 28, it is. The "dynamic equilibrium" assumption is supported, at least for RT emission, by the fact that lifetimes measured at the X and T peaks give the same value throughout the pressure range in sc KCl:In (see Fig. 28).

Similar sets of data were taken for KBr:In and KI:In. In these two compounds, the X and T peaks are found in both phases, but in only one phase is a complete treatment of the problem possible. In fcc KBr:In, p_0 is at about 4 kbar, so that emission has almost completely converted to the T peak in our pressure range. Steady state and lifetime measurements were taken to low temperatures at 4 kbar: %X (p_0) was found to be constant at

30%, and τ (p_0) was constant (within 10%) at 2.37 μsec (see Appendix G). This again supports the model, which predicts an absence of temperature effects at p_0. Emission is completely converted to peak T by 18 kbar; τ_T was measured to be 2.0 μsec at 18 kbar and to be constant within 5% to low temperatures as expected (Table G7). The RT lifetime drops with pressure slightly in fcc KBr:In, indicating that the emission is converting to peak T and that $\tau_X > \tau_T$. It can sketchily be determined that $\tau_X/\tau_T = 2.6 \pm .3$ and $g_X/g_T = 1$

A complete treatment of fcc KBr:In was impossible since p_0 is so low. However in sc KBr:In, p_0 was found to be about 42 kbar, so that a steady state plot was readily made (Fig. 30). Lines with a common intercept were not as easily fit to the data as with KCl:In. The main problem is a bending at low temperatures, probably due to barrier effects. (This was also seen in CsI:Tl steady state plots.) One cannot have much confidence in the value of the intercept in Fig. 30.

Fortunately, the intercept parameters g_X/g_T, τ_T, and τ_X are all determinable from lifetime measurements (see Fig. 31). At a very high pressure (59 kbar), τ_T was found to be .837 μsec. Low temperature lifetimes at 26 kbar (where %X ≃ 100%) yielded a constant value of $\tau_X = 4.37 \pm .1$ μsec (Table G7). Thus $\tau_X/\tau_T = 5.22$ and $\log(\tau_X/\tau_T) = .72$. The intercept of the steady state plot, given by $\log(g_T\tau_X/g_X\tau_T)$, must be near .72, so it is clear that $g_X/g_T = 1$. In this case, then, direct measurements of τ_X and τ_T determine the steady state intercept. Lines are fit to the steady state data, giving four values for ΔE (p). These are again joined by a best-fit line for purposes of extrapolation, and a curve of τ (p) is generated from ΔE (p). As

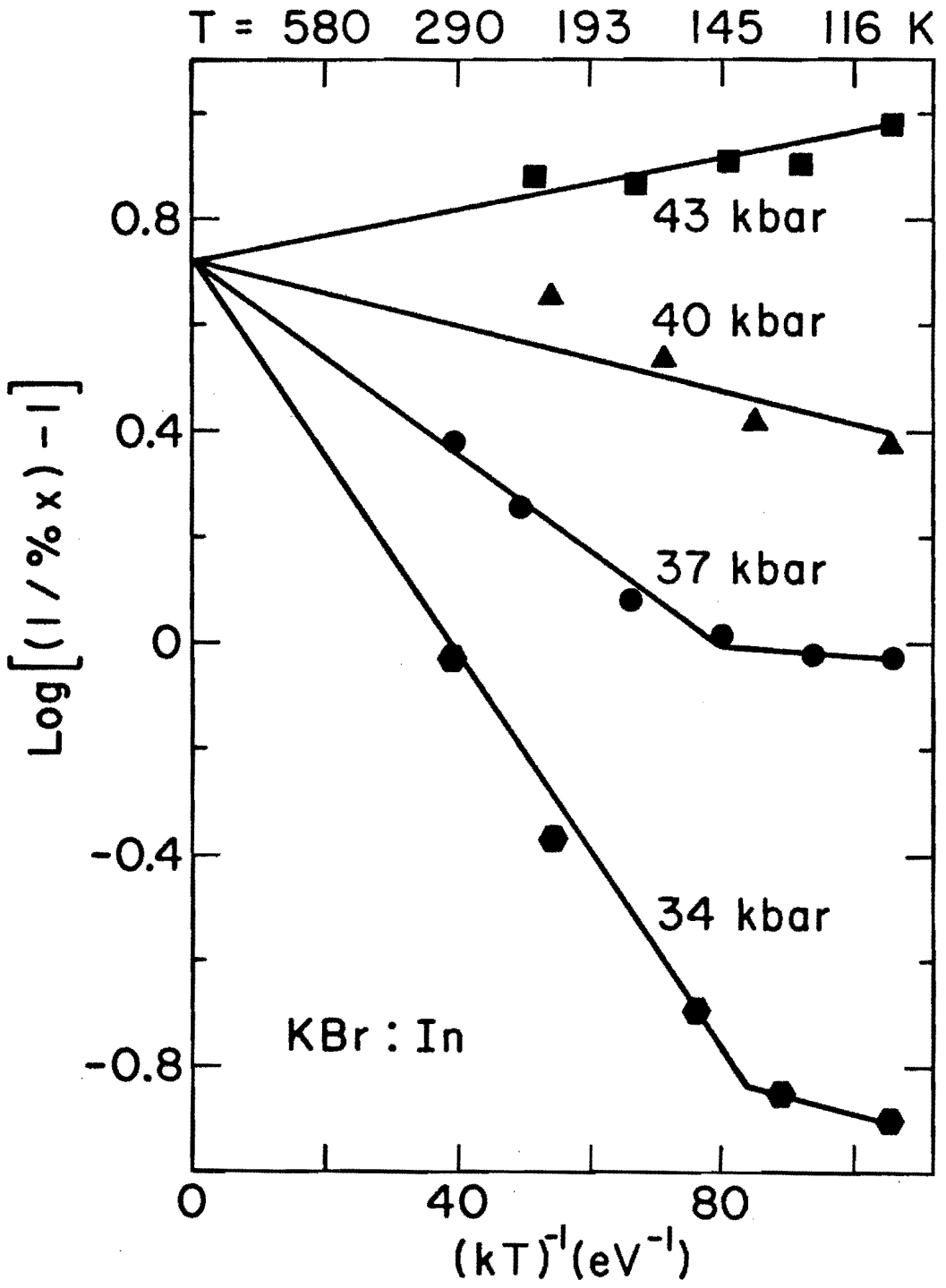

Fig. 30 Steady State Plot of KBr:In Above the Phase Transition

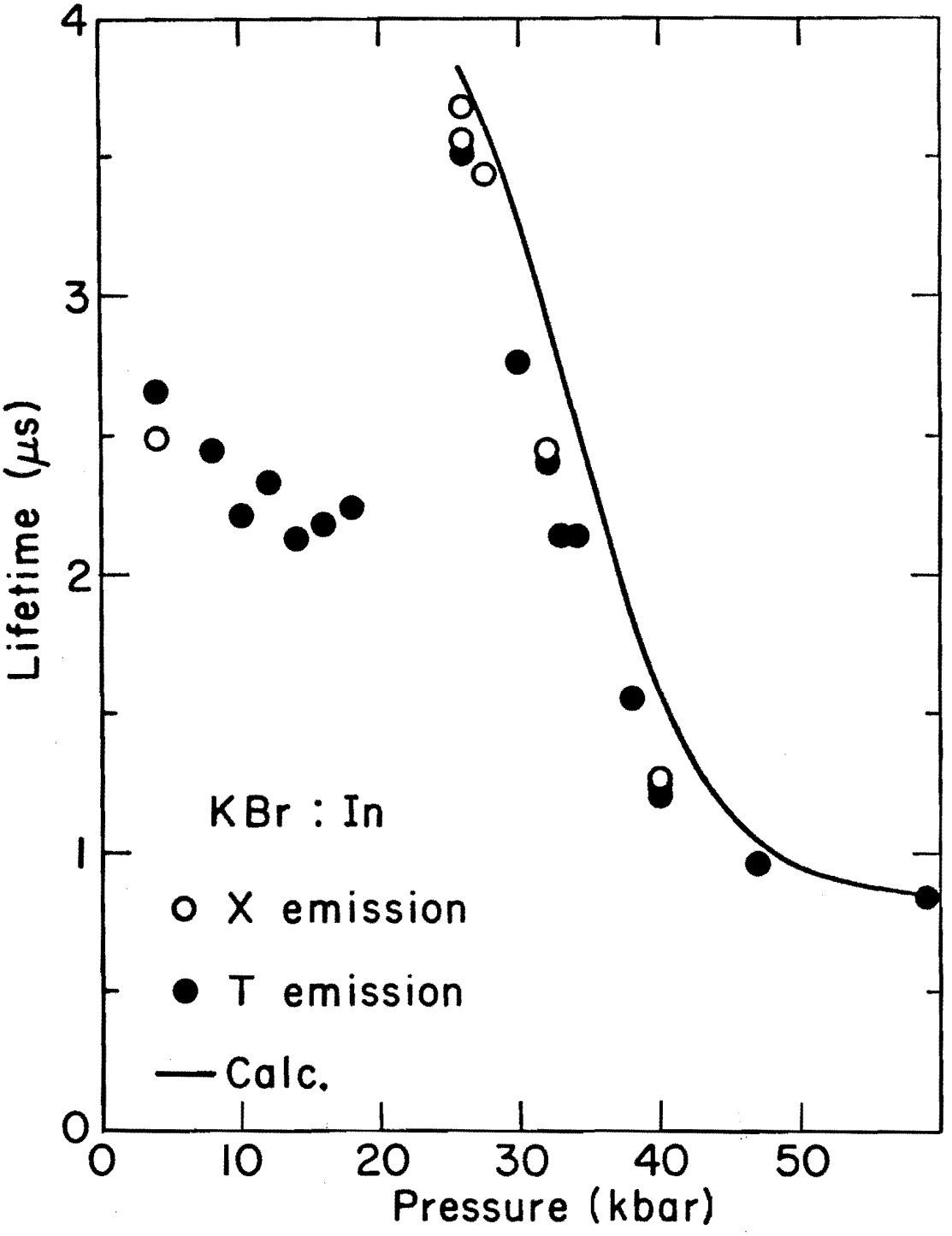

Fig. 31 Lifetime Change with Pressure for KBr:In at Room Temperature

seen in Fig. 31, calculation deviates from experiment by a small, constant amount; it appears that if our value of p_0 were one kbar lower, the curve would lie right on the data!

For sc KI:In, p_0 is too far above 44 kbar to make a steady state plot. A complete study, however was performed on fcc KI:In, despite the fact that p_0>20 kbar (above the phase transition). The steady state plot is shown in Fig. 32. An intercept of .55 means that $(g_T\tau_X/g_X\tau_T) = 3.55$. Degeneracies of $g_X/g_T = 1$ best fit the lifetime data (τ (p) and τ (T)), but the improvement over other degeneracy assignments was not as obvious as in KCl:In and KBr:In. The slopes of Fig. 32 give ΔE (p) at four pressures; unlike KCl:In and KBr:In, ΔE (p) was clearly nonlinear (see Table 7). Therefore, all calculations involving ΔE were done at four pressures and the results were then joined by a smooth curve.

The curve in Fig. 33 is such a smooth curve. Agreement with experiment is good. To calculate τ (p), either τ_X or τ_T had to be found. From Table G4, at 6 kbar %X ≃ 1 for low temperatures, so that $\tau \simeq \tau_X$. Fig. 34 shows τ (T) at 6 kbar; the lifetime appears to approach an LT limit of about τ_X = 2.9 μsec, in agreement with Fukuda's atmospheric pressure value of τ_X = 3 μsec [72]. This value was used with the steady state intercept to calculate τ_T = .82 . With all parameters known, theoretical curves were generated for Figs. 33 and 34. Agreement with the data in Fig. 34 (especially the independent set at 15 kbar) is quite good.

To summarize the In^+-doped potassium halides, they all are subject to the JTE in both phases, except for fcc KCl:In. The pressure p_0 at which the JT splitting is zero rises in both phases in the sequence $p_0(Cl)<p_0(Br)<p_0(I)$. The intrinsic lifetime of peak X (τ_X) is always greater than that

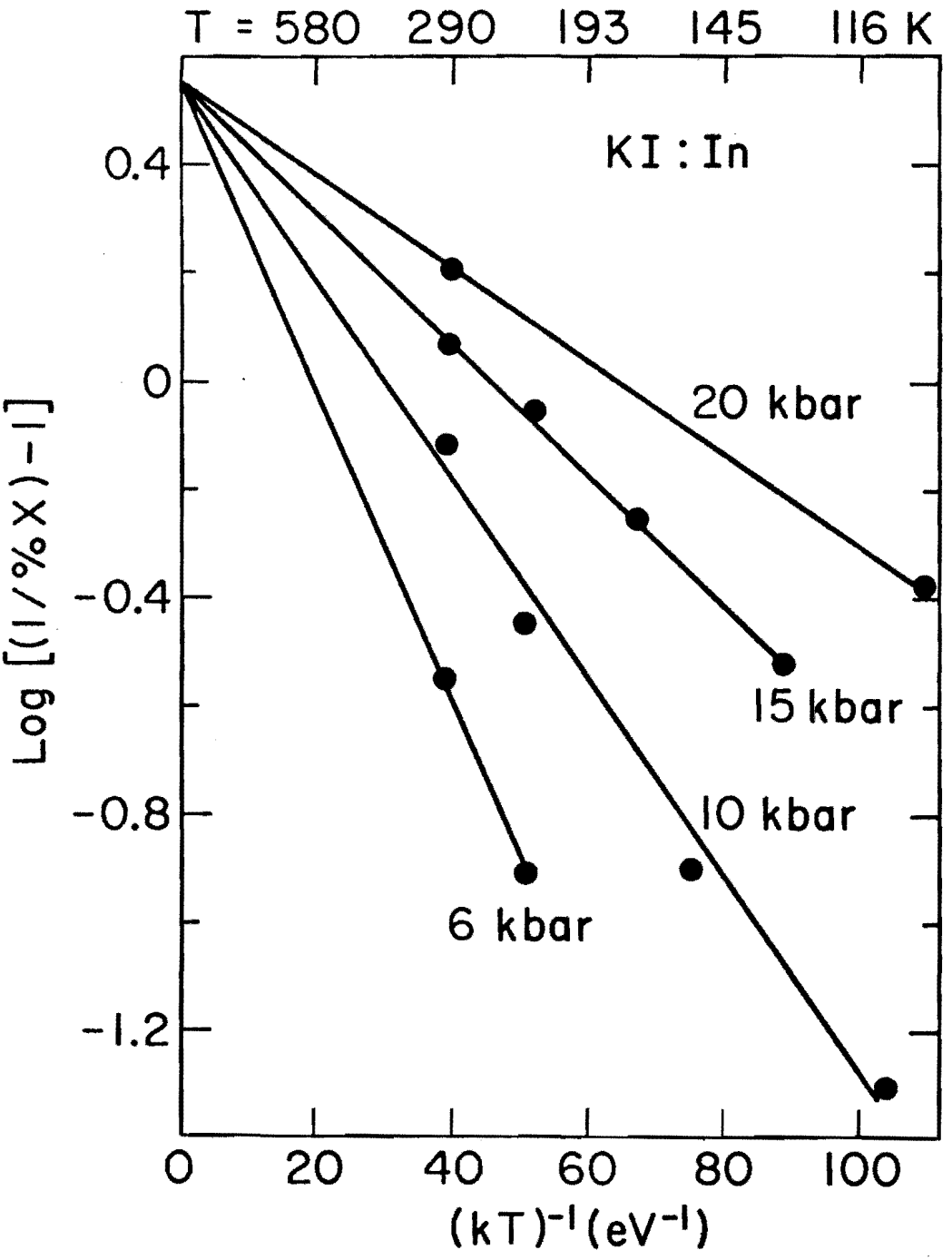

Fig. 32 Steady State Plot of KI:In Below the Phase Transition

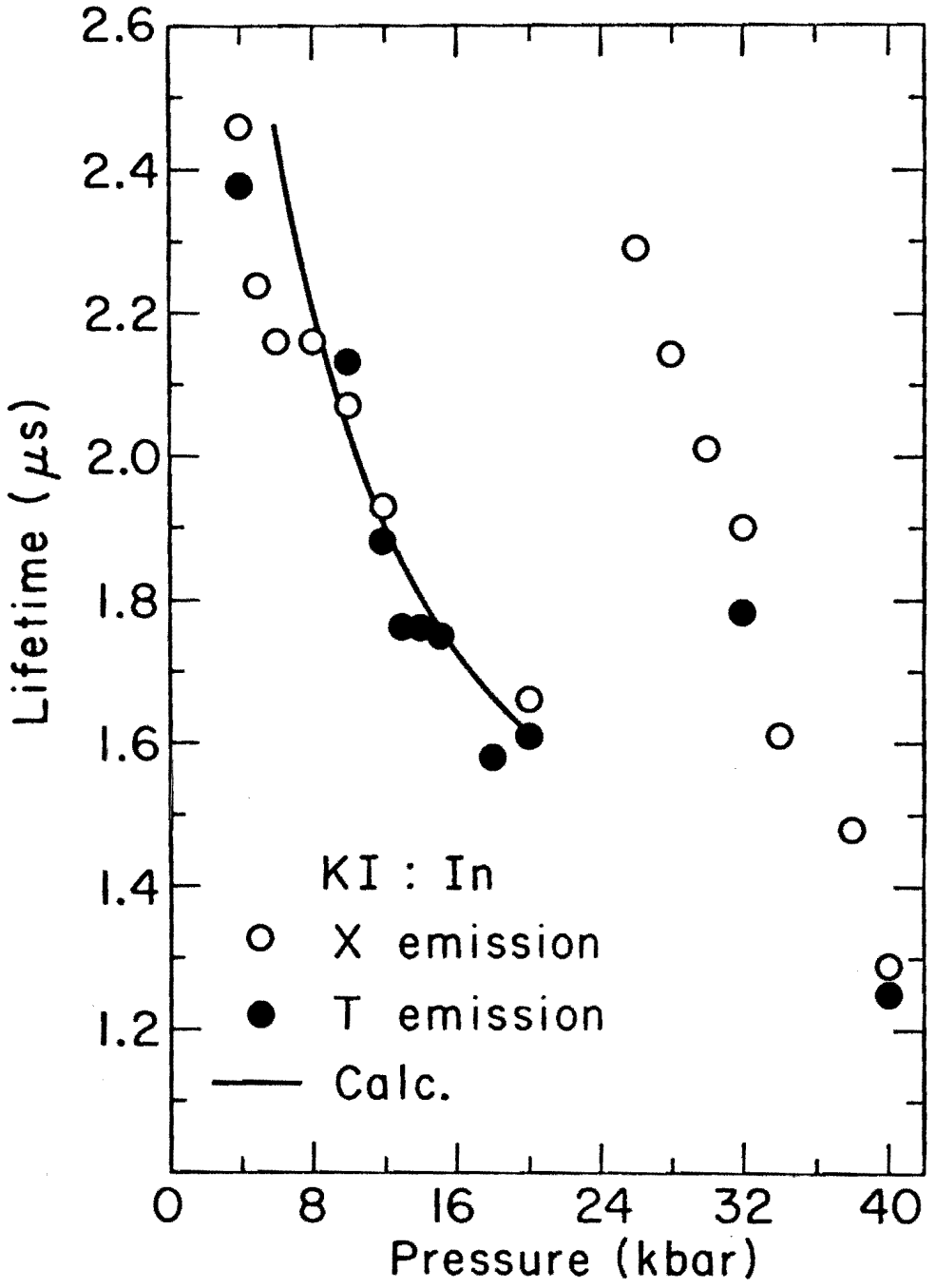

Fig. 33 Lifetime Change with Pressure for KI:In at Room Temperature

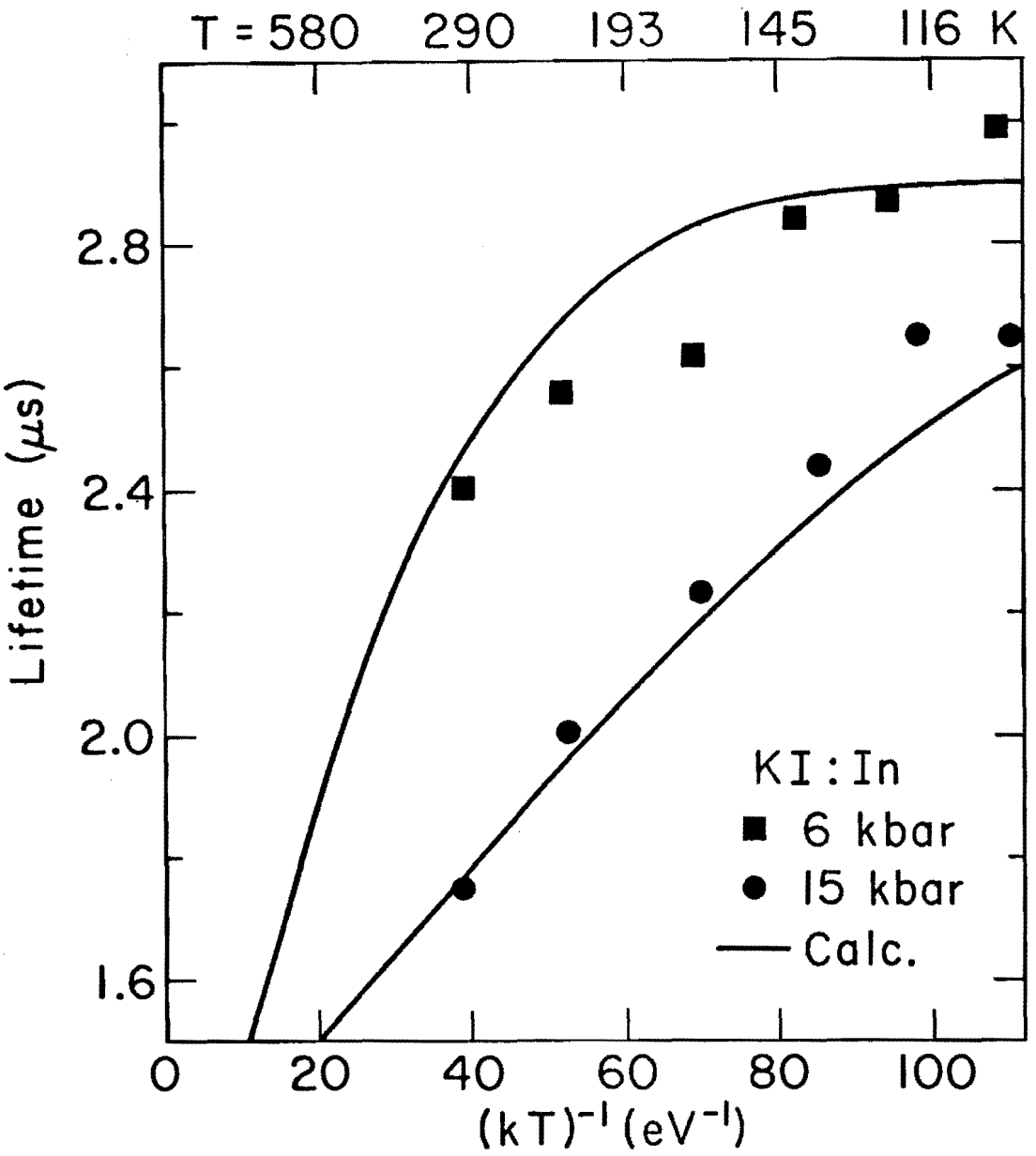

Fig. 34 Lifetime Change with Temperature for KI:In at 6 and 15 kbar

of peak T (τ_T) by a factor of three to six. Lifetimes are longer in the fcc phase than in the sc phase, as can be seen in Table 9.

Table 9

The Lifetime at Pressure p_0 in the Two Phases of KH:In

Phase	τ (p_0)(μsec)		
fcc	(>4)	~2.37	1.28
sc	2.28	1.40	<<1.2
Crystal	KCl:In	KBr:In	KI:In

Otherwise, the two phases give similar results. In all cases, X emission gives way to T emission with pressure according to the model proposed. This is due to a stabilization of the T minimum with pressure, to the point where the T level is lower than the X level at high pressures. At the same time, the measured lifetime changes rapidly from τ_X to τ_T with pressure. The major difference among the crystals is the degeneracy assignment, where without doubt, $g_X/g_T = 2$ for KCl:In but $g_X/g_T = 1$ for KBr:In. It is generally thought [72] that the X level is doubly-degenerate and the T level is non-degenerate. This would explain KCl:In. However, recent work that split the degeneracies with a magnetic field [87], insists that the X and T levels are both doubly-degenerate. This would explain the KBr:In result. Both schemes are theoretically allowed [81].

At this point, the direct evidence supporting the assumptions within the model will be summarized. The assumption of "dynamic equilibrium" holds at RT for the three KH:In; this can be seen from the equivalence of lifetimes

measured at peaks X and T in τ (p) plots. And as the temperature is lowered, whichever level is more stable (X below p_0, T above p_0) emits more and more of the light. (If the barrier were important, peak T would always rise as the temperatures fell. Barrier effects are occasionally seen at very low temperatures.)

The two-level model works well for KH:In. The level splitting is found to be constant with temperature, giving straight lines on the steady state plots. Intrinsic radiative rates were found to be constant with temperature (as τ_T (T) was constant in sc KCl:In and fcc KBr:In, and τ_X (T) in sc KBr:In), and pressure (as τ (p) was constant in fcc KCl:In, NaCl:In, and sc KBr:Tl (see Table G6) where there is no JTE). The constancy of τ_X and τ_T with temperature was also proven in fcc KBr:In and sc KCl:In by monitoring %X and τ at p_0 to low temperatures. Thus, the assumptions behind the model can be considered proven in KH:In, and one could expect them to hold true in other JT-split systems, such as the Tl^+-doped crystals to be discussed next.

2.2 Thallium-doped Alkali Halides

The criteria for choosing crystals to be studied in this work were as follows: 1) There must be an X and a T peak, according to Drotning. 2) Peaks X and T must be sufficiently separated in energy to be easily resolved. 3) Most of the conversion from X to T emission should occur within the pressure range (4 to 40 kbar) of Cell I. Of the thallium $(Tl^+)^-$ doped crystals, only KBr:Tl and CsI:Tl meet these criteria. CsI:Tl is, in addition, the one case where Drotning found three emitting peaks, so its study was a particular challenge.

It is known from the literature [72,75] that the Tl^+ lifetime is dominated even at room temperature (RT) by the metastable $^3P_0$ levels (also JT-split) that underlie the emitting levels. These traps had no effect on In^+ lifetimes for two reasons: 1) Trap depths appear to be quite small (e.g., 2.2 meV in KI:In [72]). 2) Intrinsic In^+ lifetimes are slow (on the order of 1 μsec), so the temperature must be very low (e.g., 40°K for KI:In) before detrapping, and not emission, is the rate-limiting step. In contrast, Tl^+ trap depths are tens of millivolts and intrinsic lifetimes are on the order of ten nsec.

Before dealing with a JT-split emitting level underlain by a trap or traps, let us consider a single emitting level with a trap. If the two levels are in "dynamic equilibrium" one has a special case of the model just described. The lifetime is given by Eq. (36) with one of the k's equal to zero.

However, in our case the wells cannot be in "equilibrium," since the decay is not single-exponential. A fast and slow component are usually seen, even at temperatures as high as room temperature. After excitation to the emitting level (absorption to and emission from the metastable level are forbidden), some emission occurs immediately (faster than the very fast Tl^+ intrinsic radiative rate). This fast component is quenched (speeded up and reduced in intensity) by the ability of most of the excitation to surmount an energy barrier and reach the trap. Detrapping occurs slowly, at a rate dependent on the ability of the excitation to surmount a higher barrier back to the emitting level, and not be trapped again before emission. The resulting decay curve is a sum of two exponentials, called the fast and slow components.

One can write the rate equations for this system. They yield a differential equation like the damped harmonic oscillator, for the population of the emitting level. Instead of a damped oscillation, the solution is the sum of two decaying terms. To make the problem tractable, approximations are made for various temperature regions. At very low temperatures, it is as if the trap weren't there. At very high temperature, the fast component is completely quenched, and the slow lifetime is twice the intrinsic lifetime of the emitting level.

What temperature regime are we in? One might guess that 100°K to 300°K is a rather high temperature for most processes in inorganic crystals. The fast component typically has a much larger coefficient than the slow component, but it is so fast the the slow component dominates in total area. Since most of the emission is in the slow component, we are in the high temperature regime.

Support for this statement comes from measurements of the amount of fast component versus temperature [88]. In five doped alkali halide crystals over our temperature range, the fast component intensity is governed simply by a Boltzmann factor, where the energy in the exponent (on the order of 10-20 meV) is interpreted to be the barrier to trapping. Such a result can be derived from the equations only at high temperatures, where the rate of trapping is much faster than the intrinsic radiative rate.

Once the excitation is trapped, the system does attain "dynamic equilibrium." The Boltzmann factor for detrapping depends on the trap depth ε(energy difference between well bottoms), not the trap depth plus a barrier

height. When the approximations appropriate for the high temperature regime are made, the slow lifetime is found to be

$$\tau = \tau_{rad}(1 + e^{\varepsilon/kT}) \rightarrow \tau_{rad}e^{\varepsilon/kT} \quad , \tag{39}$$

where τ_{rad} is the intrinsic lifetime and $\varepsilon >> kT$. Eq. (39) is just a special case of Eq. (36). In agreement with Trinkler and Plyavin [89], it is found that an "equilibrium" situation is attained soon after the first component has disappeared. Their expression for a three-level system (X, T, and trap) is correct. However, theoretically [81,87] one expects X and T to each be underlain by a trap XO and TO. Let us develop a four-level model similar to the two-level model already described. Let ΔE again be $(E_T - E_X)$, $\varepsilon_X = (E_X - E_{XO})$, and $\varepsilon_T = (E_T - E_{TO})$. Assuming no nonradiative paths, one arrives at an equation for the lifetime that is like Eq. (36):

$$\tau = \frac{1 + K + \frac{g_{XO}}{g_X} \exp\,(\varepsilon_X/kT) + \frac{g_{TO}}{g_T} K \exp\,(\varepsilon_T/kT)}{k_X + Kk_T} \quad , \tag{40}$$

where K is defined as before in Eq. (32). To reduce Eq. (40) to Trinkler's one-trap equation, one sets $g_{TO} = 0$. Since traps take no part in steady state emission, the expression for the peak-area ratio is still Eq. (37).

Proof that traps do not change steady state data is provided by the steady state plot of fcc KBr:Tl in Fig. 35. It is much the same as those seen previously, although the RT lifetime of KBr:Tl is trap-dominated. From Fig. 35, we can again find $(g_T\tau_X/g_X\tau_T)$ and ΔE (p)(see Tables 7 and 8). We find that p_0 = 9 kbar and %X (p_0) = 17%.

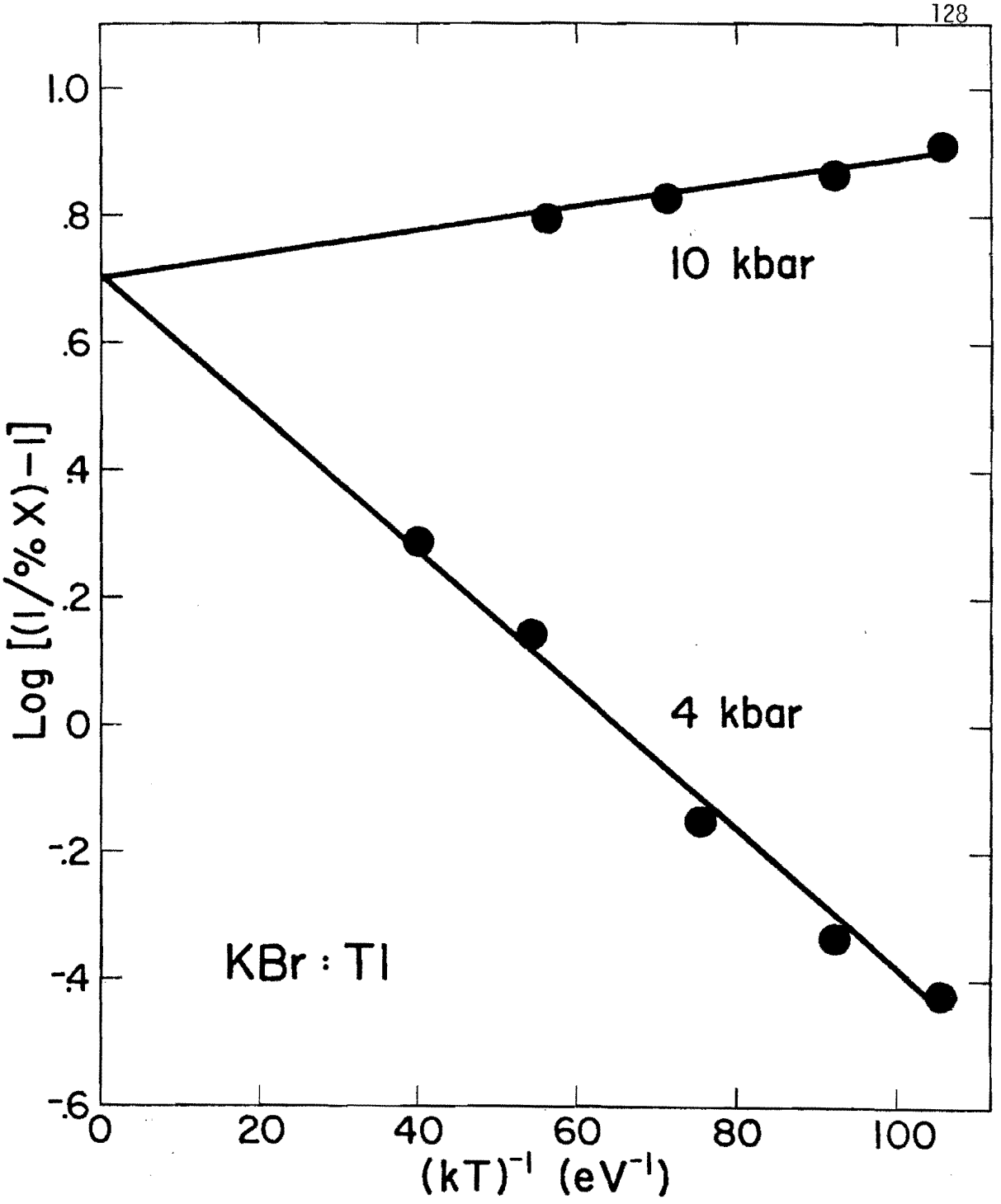

Fig. 35 Steady State Plot of KBr:Tl Below the Phase Transition

Lifetime data, however, are quite different from those of KH:In. Note that τ (p) rises in Fig. 36, instead of falling as before. The lifetime rises orders of magnitude as the temperature is lowered over our modest range, as in Fig. 37. Straight lines on such a plot of log τ versus 1/kT, imply that a single trap dominates the lifetime, which is then given by Eq. (39). The slope of the line is ϵ log e and the intercept is τ_{rad}. Below room temperature, the data in Fig. (37) do fall on lines. The problem is to show how Eq. (40) is approximated by the simpler Eq. (39) under certain conditions.

An atmospheric pressure, the trap depth in KBr:Tl measured from plots like Fig. 37 is 36 meV [88] or 40 meV [74]. Then at low temperatures ($<$RT), the trap terms dominate Eq. (40); we see this domination throughout our temperature range in Fig. 37. At a pressure as high as 18 kbar, K is large so the TO trap controls Eq. (40). Approximating, we find

$$\tau \text{ (18 kbar)} \simeq \tau_T \frac{g_{TO}}{g_T} \exp (\epsilon_T/kT) \quad . \tag{41}$$

Fitting a line to the points in Fig. 37, one finds a trap depth ϵ_T = 77 meV and an intercept $g_{TO}\tau_T/g_T$ = .02 μsec.

Ten kbar is nearly p_0, so Eq. (40) is simplified. Using the same value for $g_{TO}\tau_T/g_T$, but allowing the trap depth to change with pressure, one finds that ϵ_T = 69 meV and $\epsilon_X \simeq$ 49 meV. At four kbar, ΔE is so large and positive (ΔE = 25 meV) that the XO trap controls Eq. (40). From the slope and intercept of a line through the LT points of Fig. 37, one finds that ϵ_X = 43 meV and $g_{XO}\tau_X/g_X$ = .05 μsec. It appears that the trap depths do change with pressure, both increasing at a rate of about one meV/kbar. Thus

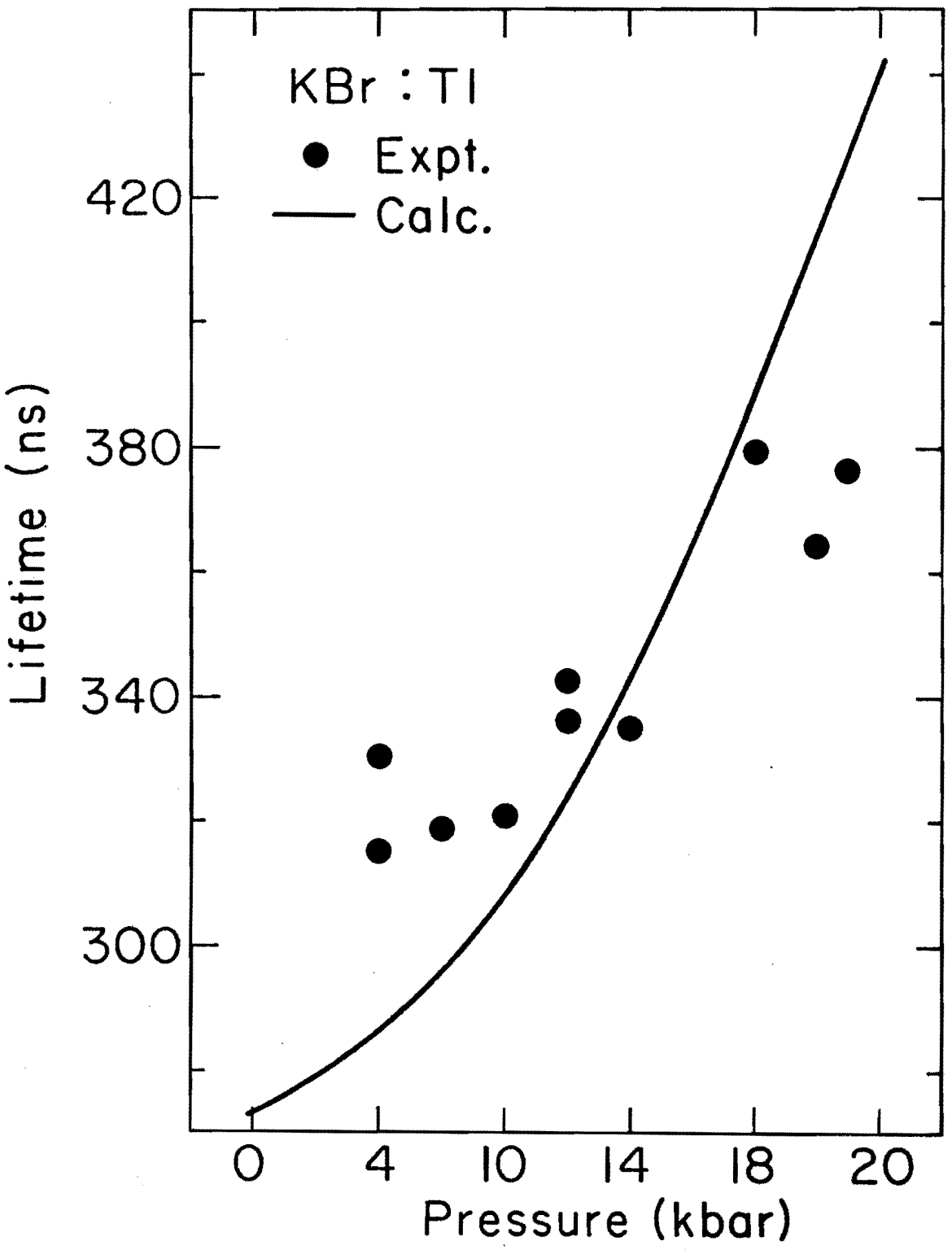

Fig. 36 Lifetime Change with Pressure for KBr:Tl at Room Temperature

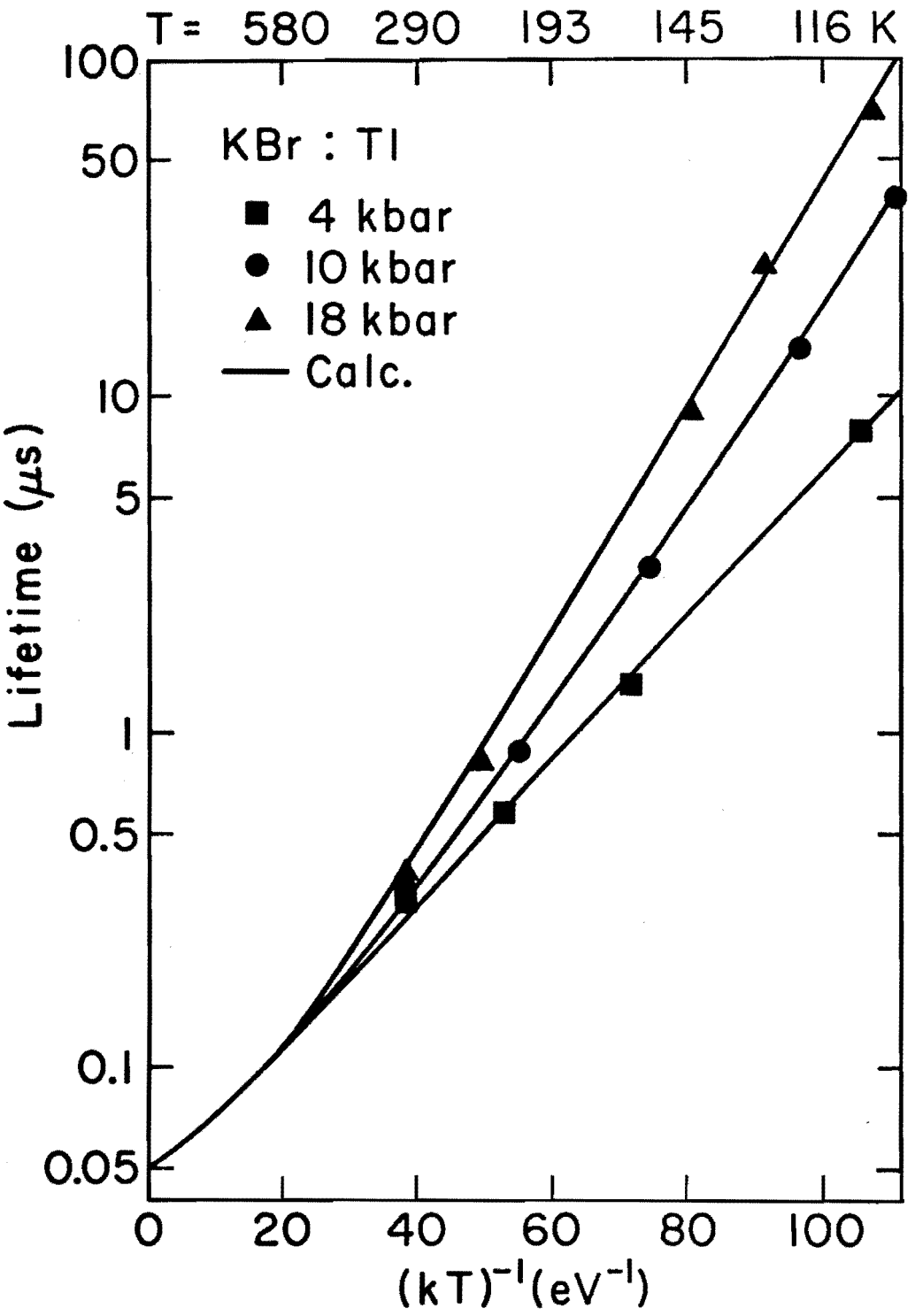

Fig. 37 Lifetime Change with Temperature for KBr:Tl at Several Pressures

$$\varepsilon_X(\text{meV}) \simeq 39 + p \qquad \text{and} \qquad \varepsilon_T(\text{meV}) \simeq 59 + p \ , \tag{42}$$

where p is measured in kbar.

If we take a ratio of the intercepts found from Fig. 37, we find that

$$\frac{g_T \tau_X}{g_X \tau_T} = 2.5 \frac{g_{TO}}{g_{XO}} \tag{43}$$

From the steady state plot, we know that the quantity on the left in Eq. (43) is five. So $g_{TO}/g_{XO} = 2$. If the two traps are nondegenerate, or if a one-trap model is used, Eq. (43) leads to a factor-of-two discrepancy. This is proof that a two-trap degenerate model must be used. Dang and Fukuda [86] have written that the X level is generally doubly-degenerate and underlain by a nondegenerate trap. These assignments fit KBr:Tl if the T level is nondegenerate and underlain by a doubly-degenerate trap.

Once the degeneracies are assigned (g_T, $g_{XO} = 1$; g_X, $g_{TO} = 2$), intrinsic lifetimes can be found: $\tau_X = 100$ nsec and $\tau_T = 10$ nsec. With all parameters known (they are tabulated in Table 10), curves are generated to fit τ (T) and τ (p) data, by using Eq. (40). The agreement in Fig. 37 is excellent. All the curves meet at $\tau = 50$ nsec, at infinite temperature. Note that the lifetime increases with pressure at every temperature (unlike the systems without traps). There are two reasons for this: 1) Both traps become deeper at higher pressures. 2) On conversion from X to T emission, the deep TO trap dominates the shallower XO trap.

Fig. 36 shows a calculation of RT τ (p) with the data. Agreement is good considering the expanded vertical scale. Using a degeneracy assignment of $g_X/g_T = 1$ in Fig. 36 gives slightly worse agreement, though it does

Table 10

Emission Parameters of KBr:Tl

$$\frac{g_T \tau_X}{g_X \tau_T} = 5$$

$\frac{g_{XO} \tau_X}{g_X} = .05$ μsec

$\frac{g_{TO} \tau_T}{g_T} = .02$ μsec

$\frac{g_{TO}}{g_{XO}} = 2$

$\frac{g_X}{g_T} = 2$

$\tau_X = 100$ nsec

$\tau_T = 10$ nsec

Energy (meV)	Pressure (kbar) 0	4	10	18
ΔE	44.4	24.9	-4.37	-43.4
ϵ_X	39	43	49	57
ϵ_T	59	63	69	77

(Symbols for the parameters are defined in Eq. (40))

not much affect Fig. 37. However, the trap degeneracy is certainly $g_{TO}/g_{XO} = 2$; any other assignment leads to a paradox.

Besides degeneracy assignments, some of the values in Table 10 are more certain than others. Trap depths ε_X(4kbar) and ε_T(18 kbar) were measured, but their increase with pressure is given only by the fit to τ (T) data at 10 kbar. Thus, other trap depths are approximate. Similarly, ΔE was measured at 4 and 10 kbar, and other ΔE values are linear extrapolations. The main conclusion is that a trap must underlie each level, X and T, and that the trap under the T level is doubly-degenerate.

In Table 11 is a tabulation of atmospheric pressure parameters of KBr:Tl, as measured by two experiments, and as extrapolated from this work at higher pressure. Agreement is quite good for the three parameters that can be compared.

Table 11

Atmospheric Pressure Values of KBr:Tl Parameters
(Symbols for the parameters are defined in Eq. (40))

Source	This Study (extrapolation)	Ref. 88	Ref. 74
ΔE (meV)	44.4	40	-----
ε_X(meV)	39	36	40
$\frac{g_{XO}\tau_X}{g_X}$ (nsec)	50	67	50

The other Tl^+-doped crystal which we studied is the CsI:Tl system; it is quite complicated, but complete conversion occurs from 0 to 40 kbar. Drotning found three emitting peaks coexisting at 24 kbar. They are

labelled (starting at lowest energy) 1, 2, and 3. Peak 3 is similar in behavior to a T peak, and peak 2 is probably the analog to an X peak [23]. Peak 1 appears to be the new addition, and probably has trigonal symmetry [83]. At atmospheric pressure, only peak 1 is seen at room temperature.

Peak 2 grows in with pressure until at 20 kbar it is larger than peak 1. To 30 kbar, peak 2 is largest, while peak 1 shrinks and peak 3 rises. Finally by 50 kbar and at higher pressure, only peak 3 is found. CsI has the sc structure at all pressures; there is no phase transition.

It is known from atmospheric pressure studies [90], that peak 2 grows in at lower temperatures down to 130°K. It turns out from our measurements that peak 2 rises as the temperature drops for every pressure from 0 to 40 kbar. Thus level 2 is at lowest energy throughout the pressure range of cell I. However, peak 2 is the largest peak only from 20 to 30 kbar at RT, because the intrinsic rate of emission from level 2 is much slower than for levels 1 and 3.

Since peaks 2 and 3 are probably analogs to peaks X and T respectively, let us examine them first. Fig. 38 shows a steady state plot, where peak 2 takes the place of peak X. The situation is similar to the preceding plots because we are at pressures at which no emission from peak 1 is seen. One unusual feature is the large intercept (.87). This means that $(g_3\tau_2/g_2\tau_3) = 7.4$. For the sake of simplicity, assume that all levels are nondegenerate. Then τ_2 is 7.4 times slower than τ_3. Levels 2 and 3 cross at p_0 = 41 kbar, where %2 = 12%.

The situation with lifetimes is more complicated. One might expect data similar to that of KBr:Tl, but from Fig. 39 it can be seen that the RT

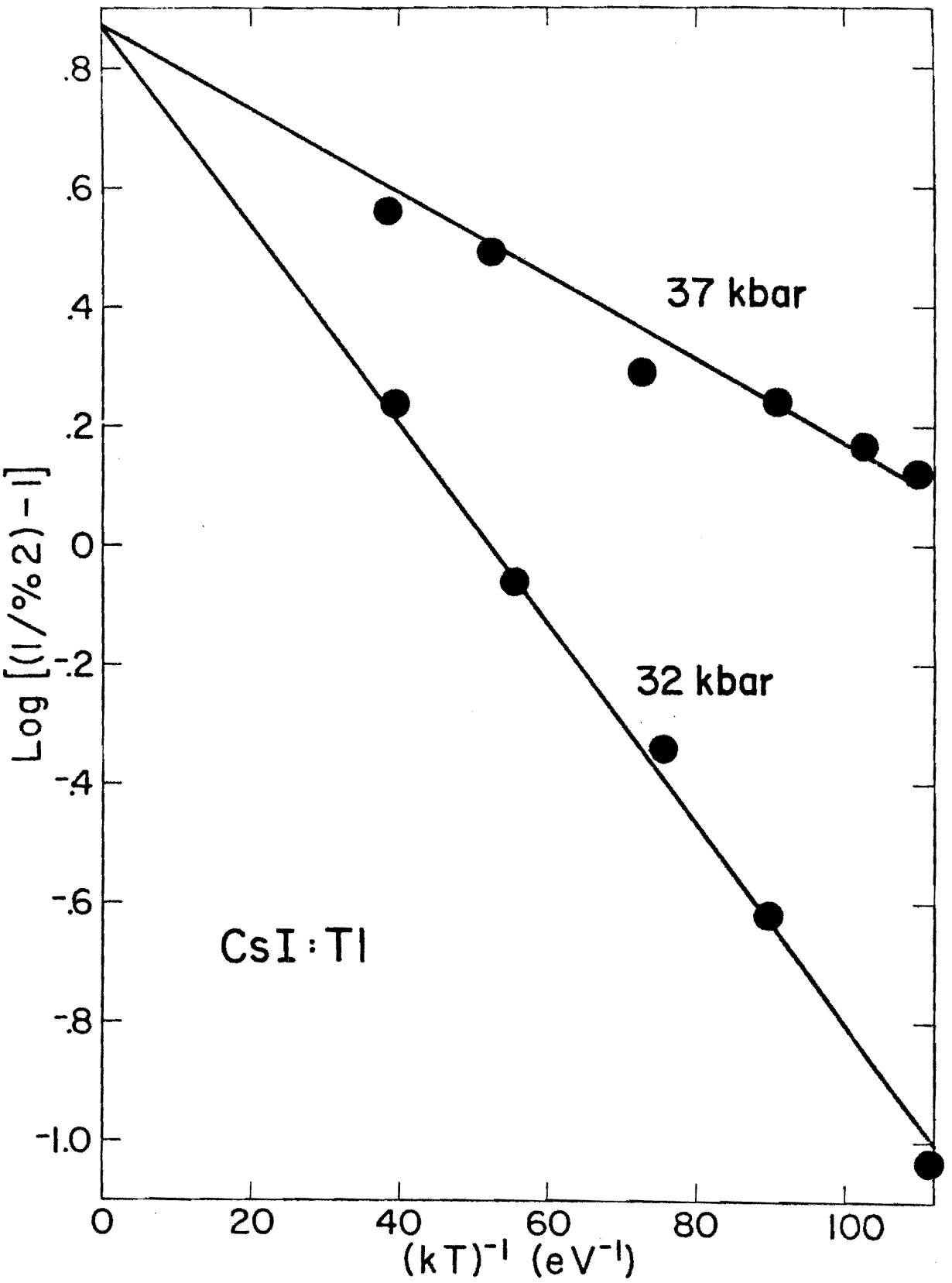

Fig. 38 Steady State Plot of CsI:Tl at High Pressures

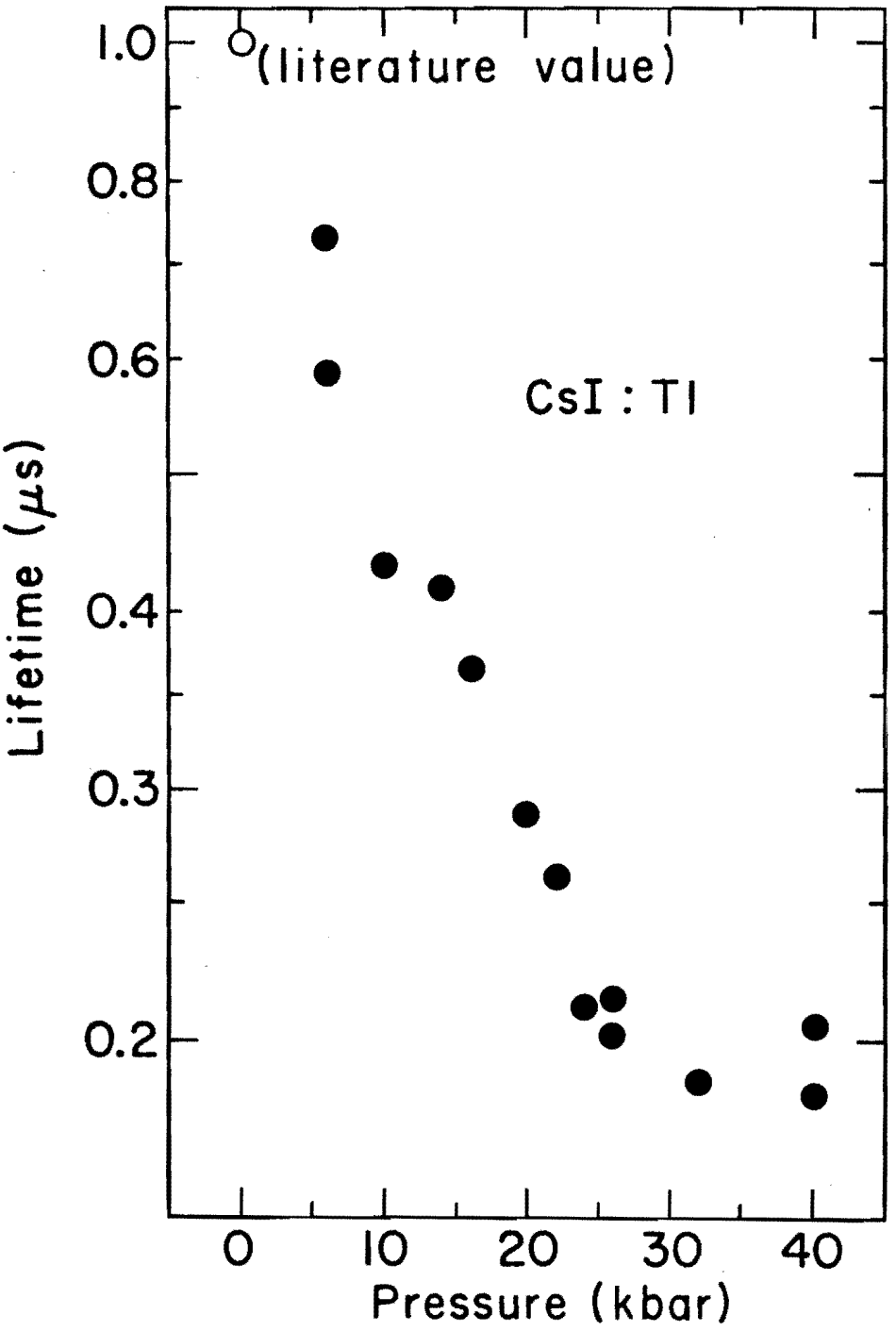

Fig. 39 Lifetime Change with Pressure for CsI:Tl at Room Temperature

lifetime drops with pressure instead of rising. In Fig. 40, τ (T) curves do not tend toward a common intercept, as with KBr:Tl, though they are clearly trap-dominated. Note that the dashed curves in Fig. 40 denote smoothed curves for the eye to follow, not calculation. It turned out that no calculations were possible for this system.

Eq. (40) for a trap-dominated lifetime can be easily extended to the CsI:Tl case. For a general system of n emitting levels of energy E_i, each underlain by a metastable level E_{i0} at depth $\varepsilon_i = E_i - E_{i0}$, all in "dynamic equilibrium," the measured lifetime is

$$\tau = \frac{\sum_{i=1}^{n} [g_i C_i + g_{i0} C_i \exp(\varepsilon_i/kT)]}{\sum_{i=1}^{n} g_i C_i k_i} , \qquad (44)$$

where $C_i = \exp(-E_i/kT)$. Depending on the C_i and ε_i, one trap or another may dominate at a particular pressure, in which case log τ (T) is a straight line versus 1/kT. That is the situation at 6, 16, and 40 kbar in Fig. 40. Table 12 summarizes the slopes and intercepts found by fitting lines to the data.

Table 12

Parameters from Linear Fits to τ (T) Data of CsI:Tl

Pressure (kbar)	Slope/log e (mev)	Intercept (nsec)
6	22.2	310.
16	24.1	130.
40	88.6	3.3

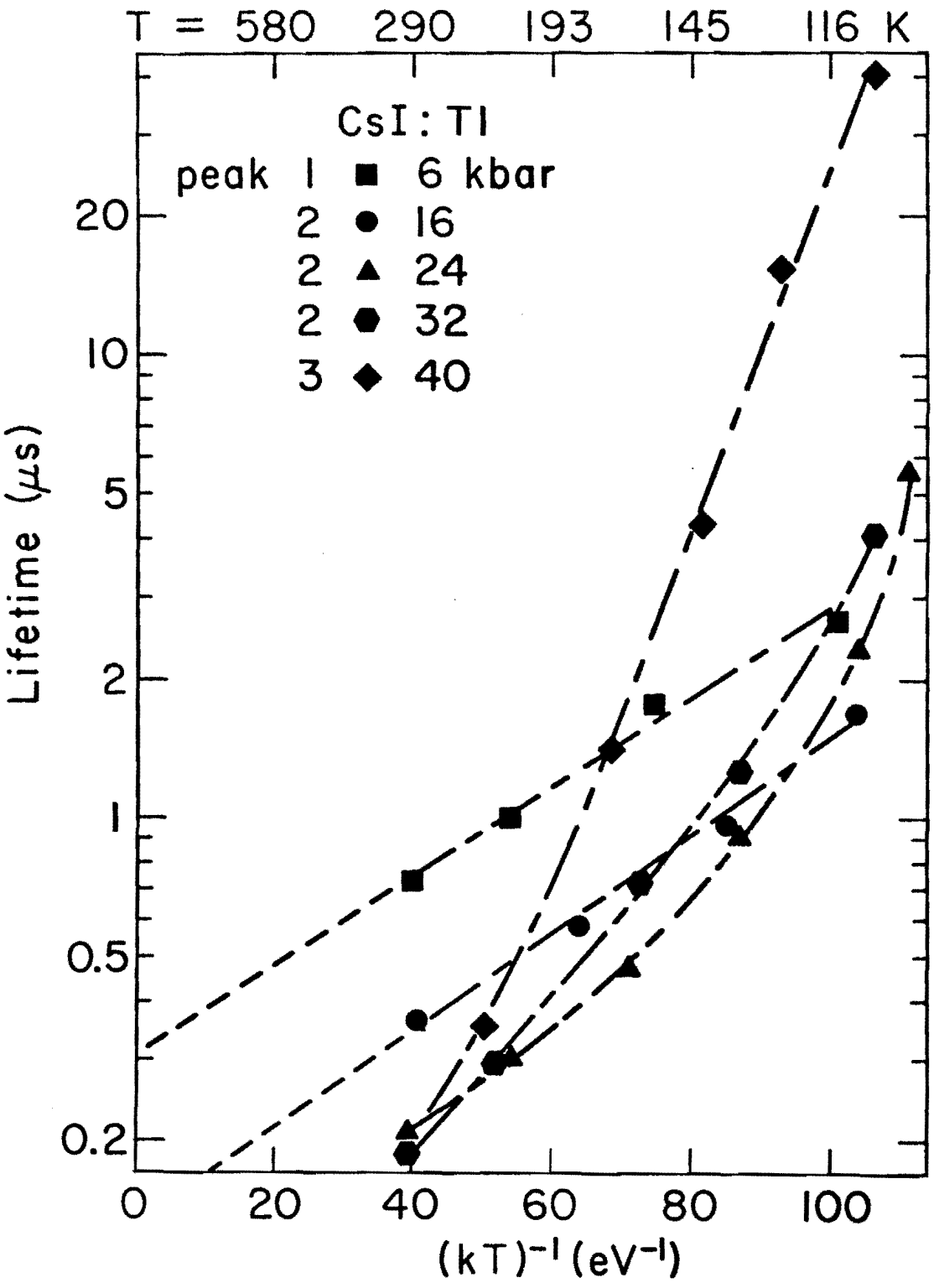

Fig. 40 Lifetime Change with Temperature for CsI:Tl at Several Pressures. Smoothed Curves Connect the Data Points

At 24 and 32 kbar, one trap does not dominate the lifetime and data for τ (T) are curved. Looking at the slopes in Fig. 40, there appears to be a gentle slope (~20 meV) for low pressures and for 24 and 32 kbar at RT, giving way to a steep slope (~90 mev) for 40 kbar and for 24 and 32 kbar at LT. The simplest theory would then have a shallow trap dominate the lifetime at low pressures and a deep trap at high pressures.

If τ (T) at 6 and 16 kbar is governed by the same trap (the slopes are the same), it is clear that an intrinsic rate must be increasing, since the 1/kT = 0 intercept in Fig. 40 drops. Even when three traps are considered, contradictions appear for the following reason: From the 1/kT = 0 intercept of 3.3 nsec at 40 kbar, τ_3 must be very fast. We know that τ_2 is 7.4 times slower than τ_3 at high pressure. From the 1/kT = 0 intercept of 310 nsec at 6 kbar, τ_1 must be very slow, and from steady state measurements τ_2 is slower than τ_1. Therefore τ_2 at high pressure must be ten times faster than at low pressure.

From Fig. 38, it appears that τ_2 and τ_3 are constant above 32 kbar. At low pressure, where peak 3 vanishes, a steady state plot was attempted, but there was no common intercept. The intercept τ_2/τ_1 dropped with pressure, implying (like the τ (T) intercepts) that τ_2 drops with increasing pressure. A decrease with pressure of the intrinsic lifetime of τ_2 of level 2 would explain the falling 1/kT = 0 intercepts in Fig. 40, if the intercepts are given by τ_2 and the trap underlies level 2. The same reasoning applies to the room temperature lifetime (Fig. 39), which drops quickly at low pressure, where τ_2 is changing, and levels off at 30 kbar, where τ_2 must be constant by Fig. 38.

Thus a picture of the CsI:Tl system from 0 to 40 kbar would resemble the following: At low pressure, level 3 is very high and unpopulated. Level 1 is just above level 2, which is underlain by a shallow trap. At intermediate pressures, level 3 (which is underlain by a deeper trap) has dropped and level 1 has risen to an energy comparable with level 3. At high pressures, level 1 is very high and unpopulated, while level 3 is just above level 2. Since the trap under 3 is much deeper than the trap under 2, the former controls the lifetime at high pressures. In this latter situation, levels 2 and 3 behave like levels X and T in KBr:Tl, with τ_2 constant. However, as the pressure is lowered below 30 kbar, τ_2 rises by at least a factor of ten.

What causes the change in τ_2? A thermal quenching process is unlikely because according to the equations, this would not affect the low-pressure steady state plot, which is affected. A nonradiative drain on level 2 would have an equal effect on levels 1 and 3, because of "dynamic equilibirum." That "equilibrium" applies is certain because barrier effects and fast components are seen only below 130°K in CsI:Tl. The drop in τ_2 must simply be due to a decrease in forbiddenness of emission from level 2, perhaps because of one of the many factors enumerated in Part 1.

3. Summary

A two-level "equilibrium" model of the Jahn-Teller split $^3T_{1u}$ APES is found to explain emission in KH:In above 100°K. Several independent sets of data including lifetimes and intensities versus pressure and temperature, are in good agreement with calculations from the model. Pressure invariably

stabilizes the T level with respect to the X level, often inverting the two-level system. The intrinsic radiative lifetime of the T level is faster than that of the X level.

Drotning's data for %X versus pressure showed that %X dropped from 100% to zero with increasing pressure. Calculations with the model using parameters from other data fit his points quite well (Fig. 22). In addition, Drotning published a graph similar to Fig. 41 [83]. The lines are smoothed curves through Drotning's data for the doublet separation. They are derived directly from experiment, and thus are dashed to distinguish them from calculated curves which have been solid. The doublet separation is mainly due to a Stokes' shift, but the small decrease with pressure is due to the stabilization of the T level. Points in Fig. 41 are calculated from the measured JT splittings; values for ΔE from Table 7 are simply added to the Stokes' shift (assumed to be that at the lowest pressure). In other words, the calculated points are normalized to the experimental curve at the lowest pressure. Agreement between experiment and calculation is good, implying that nearly all information about the excited state wells is contained in the model.

In KBr:Tl and CsI:Tl, metastable levels from the Jahn-Teller split $^3A_{1u}$APES are found to dominate lifetime measurements. Parameters are extracted from KBr:Tl data for a four-level "equilibrium" model. A six-level model could explain the CsI:Tl data, but for the fact that the intrinsic radiative lifetime of one of the three emitting levels is found to be pressure-dependent.

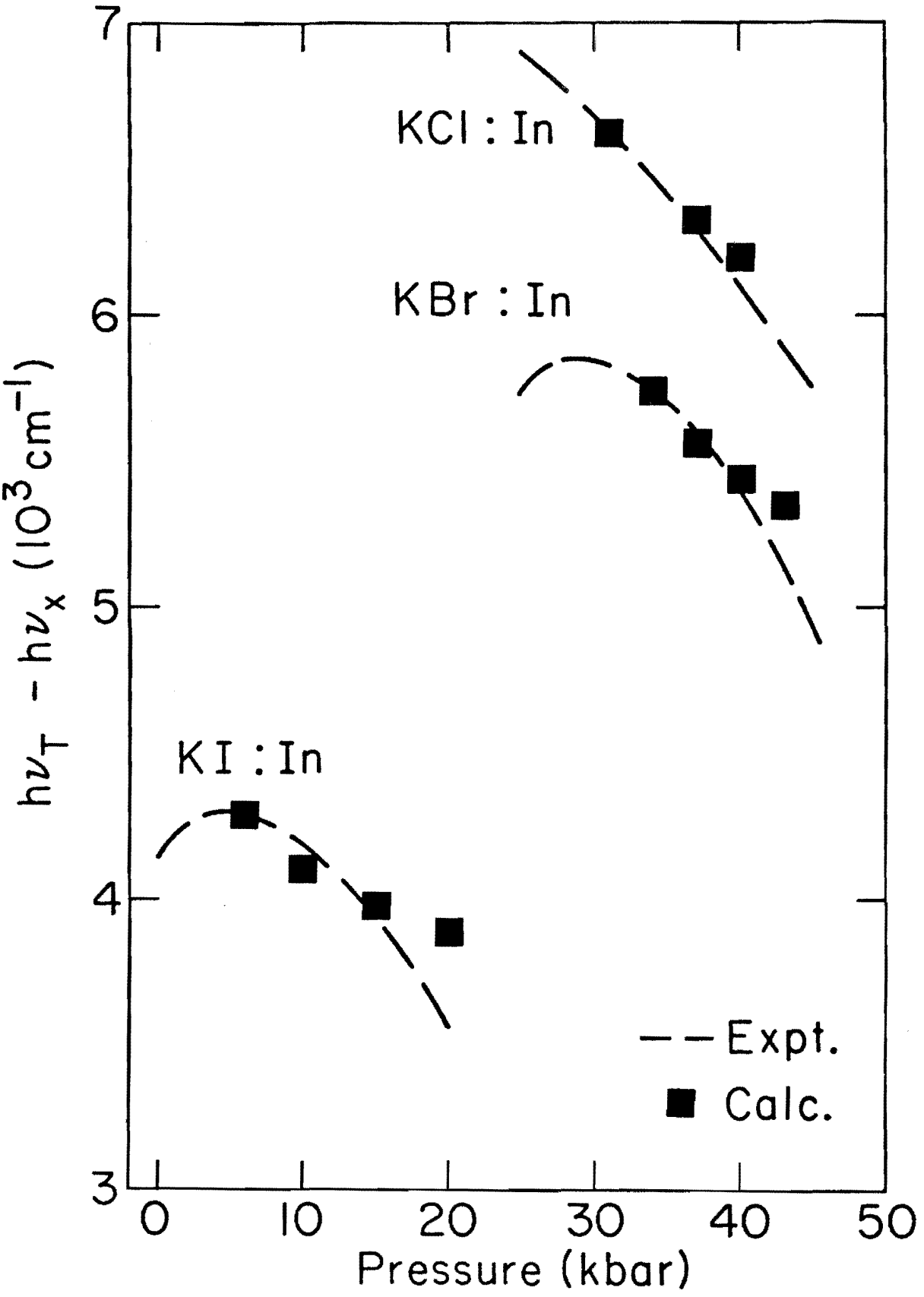

Fig. 41 Comparison of Experimental and Calculated Values for the Doublet Energy Separation vs. Pressure. Experimental curves were Measured by Drotning and Points are Calculated from Steady State Plots

4. Possible Further Investigation

This study suggests possibilities for future work. The drop with pressure of τ_2 in CsI:Tl remains unexplained. Intensity measurements of CsI:Tl total emission versus pressure might be helpful in this regard. Likewise, lifetime measurements of NaH:Pb versus pressure would help to elucidate the intensity data that were gathered and tentatively explained by the JTE [91]. Preliminary measurements given in Table G9 show that the lifetime approximately mirrors the intensity, suggesting a quenching effect. It is difficult to see how only one of a pair of JT-split peaks can be thermally quenched (see [91]) if they are in "dynamic equilibrium."

As was stated, one cannot expect to describe in as much detail other JT-split Tl^+ systems. Still, τ (p) and τ (T) data could be taken, and certainly some information could be extracted. On the other hand, In^+, Sn^{++}, and Ga^+ systems are nearly unaffected by traps, so that the four types of data now available are redundant. Since steady state plots are difficult except for KH:In, we have %X (p), τ (p), and τ (T). In addition, from Drotning's data for the steady state doublet separation, one can find $[d\Delta E(p)/dp]$ as in Fig. 41. For CsBr:In, CsI:In, and sc KI:In, complete conversion from X to T occurs. Data for τ (p) could be taken in Cell II and fit to Eq. (36). The resulting parameters could be used to generate curves for %X (p) and τ (T) to be compared with the data.

Although JT-split Tl^+ systems are complicated, many Tl^+ and Pb^{++} systems are not JT-split. These should be governed by a two-level model (one emitting level underlain by a trap). One could take τ (p) and τ (T) data on crystals such as NaCl:Tl, NaBr:Tl, and sc KH:Tl to find how the

trap depths change with pressure. Preliminary measurements given in Table G9 show the lifetime slowly increasing with pressure. This behavior, which is like that of KBr:Tl, suggests that the trap depths increase with pressure. Drotning [92] (following a method of Reiffel [93]) has derived an expression for the trap depth in terms of CC parameters for the emitting state. These parameters could presumably be found from Drotning's steady state data. Information can also be gleaned from the fast component. If the amount of fast component can be measured [88,73], the barrier (to intersystem crossing) height versus pressure would be known. Perhaps the Tl^+ system could serve as a prototype for other phosphorescent mechanisms, such as organic singlet-triplet systems.

5. SUMMARY OF RESULTS

The effects of temperature and high pressure on the luminescent decay and spectra of impurity-activated alkali halides were investigated. For the transition-metal ions Cu^+ and Ag^+, pressure was found to decrease the phonon assistance. For the heavy metal ions In^+ and Tl^+, pressure was found to change the Jahn-Teller splitting. In both cases, pressure couples to a nontotally symmetric lattice distortion.

The effect of pressure to 140 kbar was measured on the room temperature luminescent properties of the sodium and potassium halides doped with Cu^+ and Ag^+. In all cases, emission peaks shift strongly to higher energy with pressure (as much as 20% in 100 kbar). The measurements are interpreted through a simple configuration-coordinate model. For most centers, the increase in volume upon excitation is about 20% of the molecular volume, and the ratio of force constants R of the excited state compared with the ground state is less than one. Compression of the breathing mode couples to the odd phonon which assists the forbidden transition in Cu^+- and Ag^+-doped alkali halides. The model predicts that pressure will decrease the phonon assistance. Measured lifetimes are found to increase with pressure (typically doubling in 100 kbar), in agreement with predictions.

In the potassium halides doped with In^+, a simple two-level "equilibrium" model is found to explain the kinetics of the Jahn-Teller split excited state. Several independent sets of data, including spectral and decay measurements versus pressure (0-60 kbar) and temperature (100-300°K), provide enough redundancy so that model parameters are well established. The T level, which at low pressure has a higher energy than the X level,

falls until at high pressure it is more stable than the X level. The intrinsic radiative lifetime of the X state is longer than that of the T state. In KCl:In, the X level is doubly-degenerate and the T level is nondegenerate, while in KBr:In, the X and T levels are equally degenerate.

In KBr:Tl, each emitting level is underlain by a metastable level or trap. The trap under the T level is deeper than and twice as degenerate as the trap under the X level. Behavior of the X and T levels is similar to that just described for In^+. In CsI:Tl, there are three emitting levels underlain by traps. One of the emitting levels has a pressure-dependent intrinsic radiative lifetime, which makes it difficult to describe the system quantitatively.

To our knowledge, the decay measurements taken with the apparatus herein described are the first high-pressure measurements of lifetimes in the microsecond range. The apparatus is capable of measuring high-pressure lifetimes of from 100 nanoseconds to five seconds long. In addition to its use in this work, this apparatus has been employed in the study of thermal quenching and resonant energy transfer under high pressure.

APPENDIX A

Photon Counting

Photon counting is a widely accepted method of taking low light level spectra. The development of fast electronics has allowed the method to be extended to medium light levels as well, covering the full dynamic range encountered in this laboratory. Single photon counting (SPC), a lifetime method, uses much of the same equipment. References for steady state photon counting (SSPC) include [37-40], and for SPC [41,45-48].

When a photon hits the PM photocathode (which is typically a two inch disc) it may or may not eject an electron. The probability of ejection is given by the wavelength-dependent photocathode efficiency, which might have a maximum of 20%. If an electron is ejected, it causes an avalanche of electrons to cascade down the dynodes to the anode. The number of electrons per pulse is given by the gain (say 10^6). This large pulse size allows pulses to be easily amplified to manageable levels. Pulse shape is determined by the PM and the dynode chain of resistors and capacitors. The ideal PM for photon counting has maximum gain (say 10^8), minimum risetime (say one nsec), and few dark counts (say one per second). There are various methods to decrease dark count [37,38], once the PM is installed: masking off part of the photocathode, shielding the PM body, and cooling the PM are among them.

The PM used in this work was an EMI 9558 QA #14651. It has a gain of 10^6, an 8 nsec risetime, and a dark count rate of 20 Hz. This is adequate for our purposes. A "standard" dynode chain was used [44], which is also adequate. The PM and dynode chain should be changed for more demanding

work (see Appendix B). The PM is cooled to -70°C and shielded from magnetic fields and RFI. In such an environment, many of the dark counts are generated by cosmic rays and radioactivity.

To avoid picking up RFI on a long cable length, the PM pulses are sent into a nearby preamp with 50 Ω input impedance. A long cable can then be used to the amplifier/discriminator. The preamp has a 1.5 nsec risetime (RT) and the amplifier has a 3 nsec RT. To distinguish photon-generated pulses from small thermal pulses (which don't travel the full dynode chain), a discriminator is employed. Ideally one wants a constant fraction timing discriminator which reduces walk (jitter in the time the threshold is crossed). However, the discriminator chosen has a 2 nsec walk, which is acceptable.

The discriminator not only removes thermal noise, it also makes each pulse equivalent, so that the differences between pulses that the dynodes artificially introduce are eliminated. In addition, DC drift is avoided, and lower PM bias voltages can be used than are possible in an analog system. A voltage of -1200 was used for SSPC (since the PM was already calibrated at this voltage) and -1400 for SPC (since use of this maximum voltage increases PM gain).

The threshold level is set by varying it while the count is monitored. Fig. A1 shows the count rate for a medium light level and no light at each discriminator setting. (The discriminator is controlled by a 28-turn potentiometer, but only the middle 22 turns are effective.) Here the PM is under SSPC run conditions with "disc #7." One looks for a plateau in the dark count; 13 turns is the setting where the most photons are counted while the

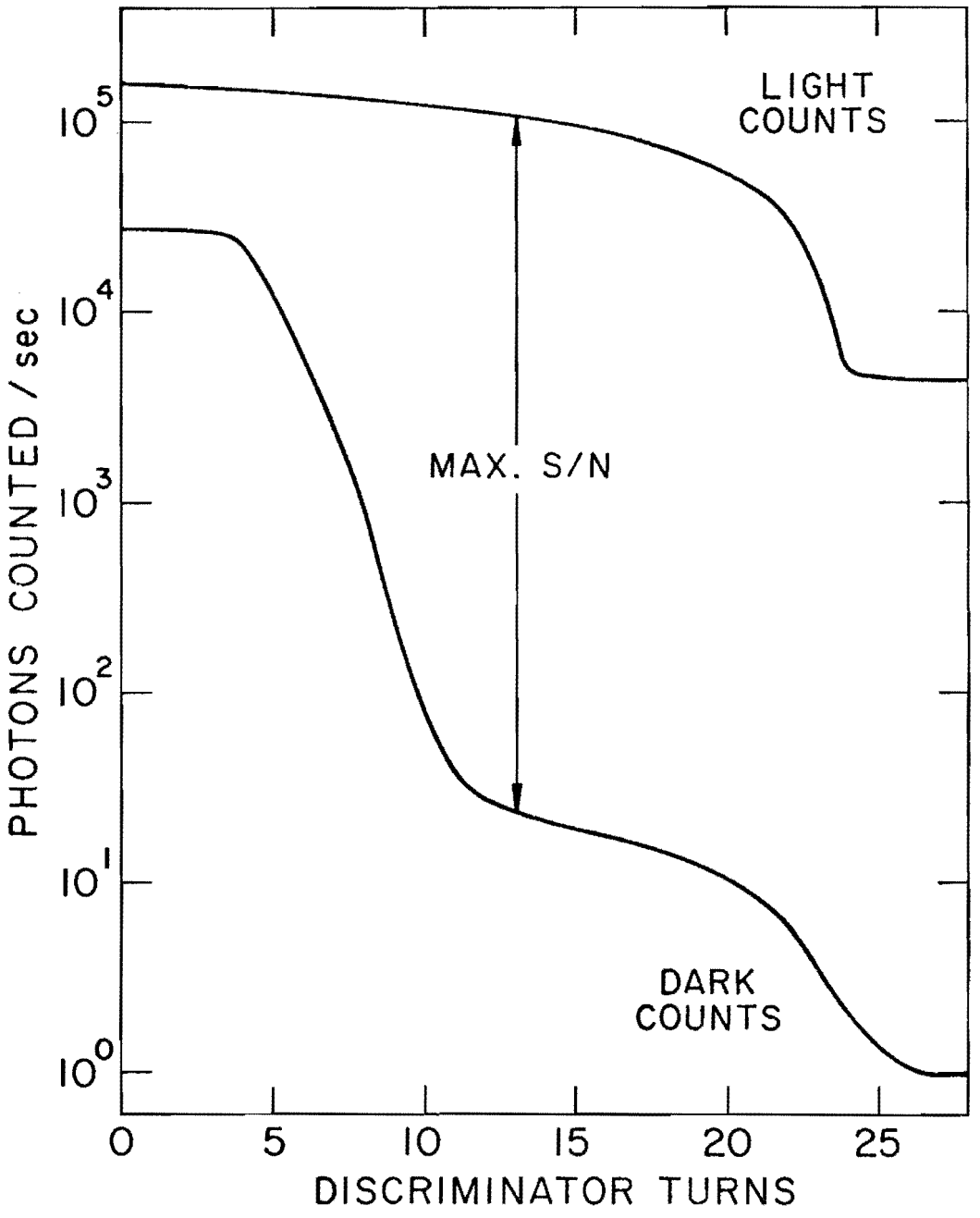

Fig. A1 Light and Dark Count Rates vs. Discriminator Level for Steady State Photon Counting

dark counts are still on a plateau, giving a maximum signal to noise ratio. Other PM's and discriminators have similar curves.

Pulses from the discriminator are counted by the photon counter, which has a 100 MHz maximum count rate. Since the discriminator only has a 9 nsec pulse pair resolution, it appears that the discriminator limits the electronics at high count rates. If the analog output is plotted against the digital output for identical high light levels, the curve is linear to a one MHz count rate (within 1%). The analog system previously used saturates at the equivalent of 2 MHz, so it is little better. At the other end, the photon counting system gives at least a five-fold reduction in signal fluctuation at low light levels. The photon counting system also allows more variation in averaging time and is faster to use than the analog system.

For SPC, the same components are used, but the setup is slightly different. The amplifier/discriminator is connected directly to the PM by a one-half foot cable. Fig. A2 shows how the threshold level was determined for SPC run conditions (cooled PM, disc #7). The dotted lines are for a bias voltage of -1200 v (similar to Fig. A1), while the solid lines are for -1400 v. On the left, the total gain is x200 (as with Fig. A1), while on the right, the gain is reduced by ten. One desires to set the threshold level high above the baseline, which is fluctuating due to lamp-induced RFI. On the other hand, if the level is too high, only large pulses produced by photon pile-up will register. It was found that above 20 turns with a gain of x20, decay curves were affected by the pile-up effect; indicative of this is the extreme drop in Fig. A2 at that level.

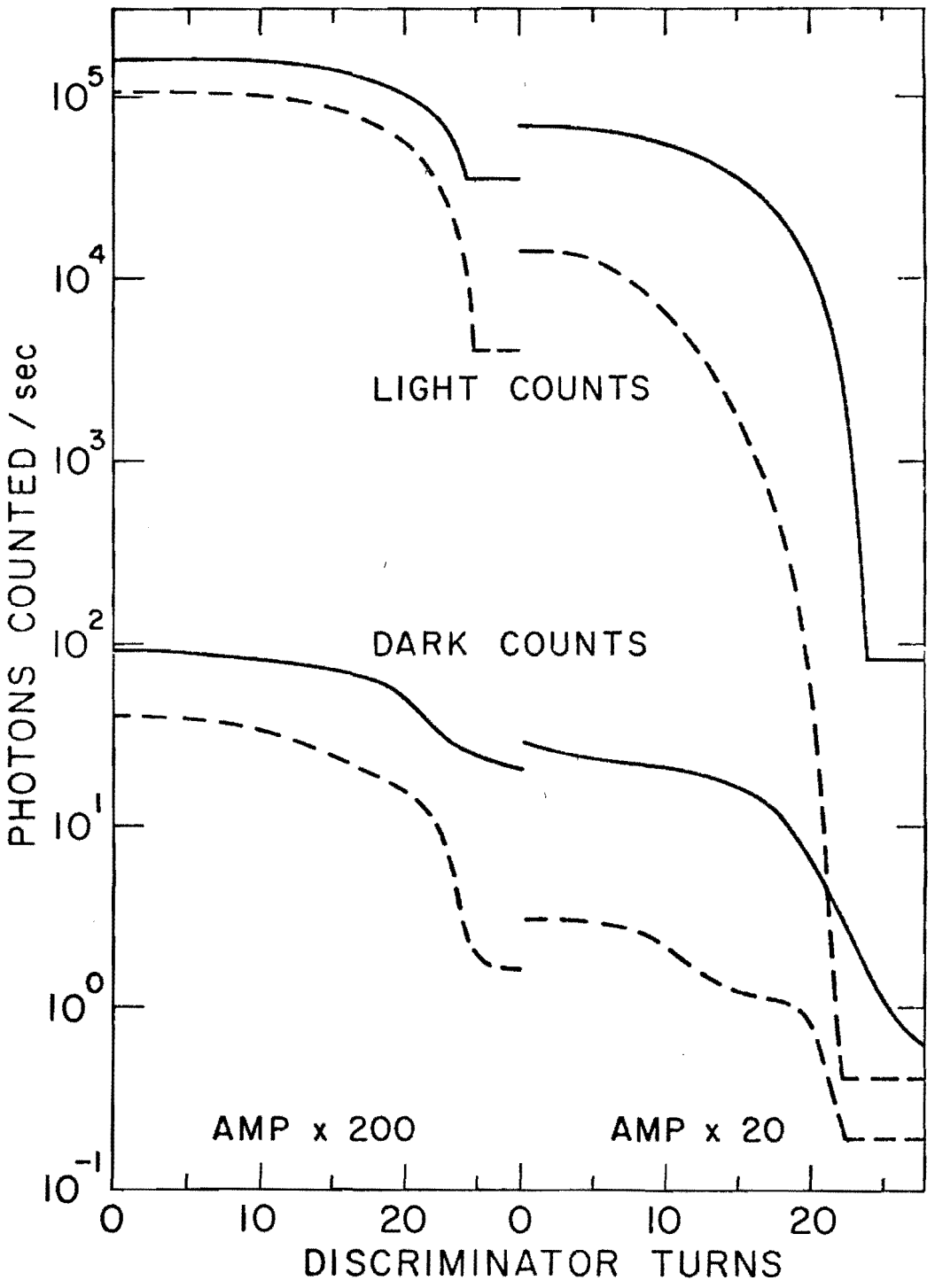

Fig. A2 Light and Dark Count Rates vs. Discriminator Level for Single Photon Counting

Therefore, the proper discriminator setting for SPC is below 20 turns with a gain of x20 and a bias voltage of -1400 v. If RFI is not a problem, lower settings are useful when low light levels are encountered.

Graphs similar to Fig. A1 were plotted for three other PM tubes which we occasionally use. The results showed that all are usable with photon counting, but that none is better than the PM used in this work.

APPENDIX B

Laser Emission Rig

Many improvements of the high pressure decay apparatus described here are possible. It is hoped that some of these suggestions will be incorporated in a laser emission rig. The idea is to construct an instrument to study luminescent kinetics and efficiencies, whereas the present emission rig was designed to measure spectra. For many materials, especially organics, lifetimes are faster or quantum yields are lower than we can measure. In addition, the competition between fluorescence and phosphorescence makes some sort of time-resolved spectroscopy desirable.

To this last end, a phosphoroscope seems the correct solution. Another possibility is a brighter flashed source (e.g., the ILC 100 Joule flaslamp or a pulsed laser) coupled with a boxcar integrator. Still another is a weak spark gap with a high repetition rate, coupled with a gated photon counter [46]. However, this is one case where a chopper (the phosphoroscope) is probably superior to a pulsed source.

A more powerful steady state source is desirable. The present source (a 200 W Hg lamp) has a .6 x 2.2 mm arc, magnified by three, and the lens collects 3% of the light. Then only about .3% of the light enters the cell. If the 365 nm line is selected, ~2 mW reaches the sample. Calculating similarly for a 1000 W Hg lamp, which has a longer arc, one finds that the amount of light into the cell is not much more (at most a factor of two). However, for a Xe or XeHg 1000 W lamp, there is about a factor of four improvement.

If the excitation bandpass is increased over the present maximum of 1.6 nm (to, say, the 9.6 nm bandpass of a Schoeffel double 1000 W monochromator), Hg line transmission will not be affected, but Xe continuum usable intensity will be increased by x24 over that of the present arrangement. A single monochromator is insufficient for stray light rejection, unless its output is further filtered by Schott UV-R filters (or possibly liquid or colored glass filters).

One could use a CW laser instead of a steady state lamp. However, the reasonably priced available lasers are HeCd (325 nm), which puts out 2 mW like the Hg 365 line, and argon ion, which can output about 100 mW (near 350 nm) as price approaches $10,000. When price, uv output, and tunability are considered, it is clear that the steady state lamp is still superior to the CW laser for us.

A pulsed laser, however, offers a great improvement over a flashed lamp. For example, the Laser Energy N99 pulsed nitrogen laser puts 5 KW (at 337 nm in a 10 nsec pulse) into the pressure cell. By comparison, the usable uv output from the spark gap in a 40 nm bandpass might be 5 W. The factor of 10^3 comes entirely from the fact that the laser beam is monochromatic and linear. The laser must have a small aperture and divergence to be focussed into the cell. (Some N_2 lasers are not focussable to a point.) Another possibility is the excimer laser, for deep uv excitation. Tunable lasers are available: A frequency-doubled dye laser excited by an N_2 laser or a solid state harmonic laser coupled with a dye cell or crystal tuner would cover the range from uv to ir.

The pulsed laser should not be used for SPC, since it would quickly wear out. Electronics might consist of a boxcar integrator, a transient recorder, or an oscilloscope. The transient recorder is not suitable for the fastest decays. A boxcar integrator of sufficient resolution is expensive and would require almost as many flashes as SPC. A fast scope (300 MHz) would be adequate for measuring the decays induced by most laser pulses. The result of a single shot could be photographed, or a number of decay curves could be superimposed photographically. Digitization of the curve would not be difficult.

A more versatile SPC rig could be designed. At present, the electronics have risetimes of about 3 nsec and somewhat smaller time jitter. By using a faster lamp and PM, lifetimes on the order of 10 nsec should be measurable. In the present spark gap, the output is reduced to 10% in 70 nsec. In the PRA 510 low-pressure spark gap in N_2, it takes 4.5 nsec. The 510's output is a uv line spectrum whose maximum is at 337 nm. The rated focussed intensity of 10^9 photons/flash for the 510 is to be compared with the present spark gap's 10^{12}. When the intensity is multiplied by the repetition rate (40,000 vs. 60) to get average power (the figure of merit for SPC), one finds that the two lamps have comparable average powers, though the 510 is 15 times faster. (The full repetition rate can be used with the present electronics if they are adjusted properly.)

A PM specifically designed for photon counting would be useful. It would have a fast RT (3 nsec), a high gain (10^8), poor red response, and few dark counts. With proper cooling, dark aging, and shielding, the dark count could be further reduced for study of inefficient phosphors. For

SPC, photons should be focussed to a spot on the photocathode, and the PM should have little jitter in its transit time.

The fast PM might also be used with the laser. In this case the PM would see a bright pulse; one ideally would use a different dynode chain, optimized to produce a linear output without ringing [47]. For SSPC, the laser emission rig should be calibrated in wavelength at the PM voltage optimum for photon counting. For lifetimes, attention should be paid to RFI problems.

APPENDIX C

Biomation → MCA Interface

The Interface is a specialized circuit that will only join the Biomation 610B transient recorder to the HP5401A multichannel analyzer (MCA). It dumps the 256 word memory of the Biomation into one quarter of the MCA 1024 channel memory. For each 6-bit word in the Biomation, the Interface gates a clock for a time proportional to the value of the word. The MCA counts the clock pulses in the multichannel scaling (MCS) mode, adding the counts to the previous contents of the channel. Both the Biomation and the MCA are incremented one channel, and the parallel-to-count conversion is repeated. After 256 repetitions, the memory dump is completed.

A Biomation data word has a value from 0 to 63 (6 bits). In the DECAY mode, this value is multiplied by ten; thus 0 to 630 counts are sent to the MCA, and the MCA memory receives a curve proportional to the recorded curve. For weak decays (case 2) when the curve consists of <5 individual "photons," baseline fluctuations can be comparable to the light signal. Then it is useful to discriminate against the noisy baseline and only count the "photons." In the PULSES mode, the discriminator level is set from 0 to 63. If the data word is larger than the level, 500 counts are sent to the MCA; if not, zero counts are sent. The result is a series of rectangular pulses and a flat background. On averaging, the PULSES method results in a smooth decay curve of the same shape as in the DECAY mode, if the following precautions are taken: The typical "photon" should last only 2-5 channels, and the average flash should produce at most two "photons."

The digital output of the Biomation is connected to the Interface. The Biomation provides the 6-bit data word and a FLAG that indicates if a new word is available. In return, it desires a WORD COMMAND (telling it to increment channels) and a REMOTE ARM signal (which arms the trigger before another flash).

The MCA has three inputs in the MCS mode. SWEEP TRIGGER begins the dump; SAMPLE TIME/RATE increments channels; and MULTISCALE is the clock input that is counted in each channel. The memory is displayed on a scope during accumulation, so that one knows when sufficient averaging has occurred by the visible smoothness of the curve. As the curve enlarges, one increases the scale of the display with the COUNTS/DIV control. The maximum setting is 10^6 counts full scale, which is never reached. Since the minimum setting is 10^3 counts full scale, the Biomation word is expanded to a maximum of 630 counts, so that the decay curve from a single flash nearly fills the screen.

Fig. C1 is a flowchart of the dumping process. The dump begins by starting an MCA sweep, which increments channel zero. (Channel zero thus contains the number of flashes.) The data word in channel 1 is converted to counts for the MCA. Then both the Biomation and MCA channel addresses are incremented (reaching the bottom of Fig. C1). When the Biomation returns a FLAG (within 512 μsec), the question "Is there a data word?" is answered yes, and the process is repeated. The dump of a decay curve can take about 131 msec, so the maximum flash rate is 7 Hz.

Included in the Interface box is a sequencer, which controls the entire transient digitization automatically. (A common box for dumper and

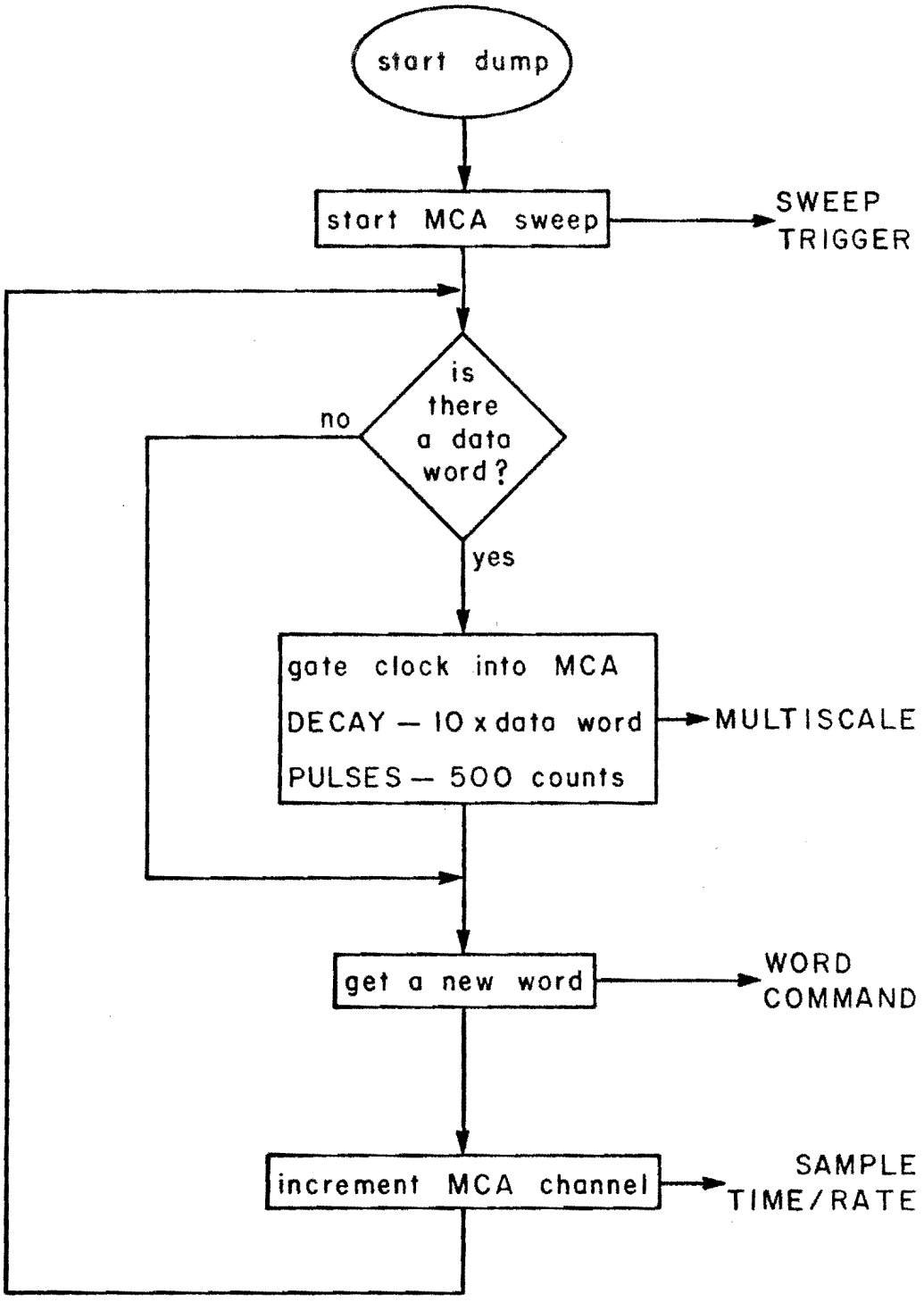

Fig. C1 Flow Chart of "Dumper" Section of Interface

sequencer obviates the need for four interconnecting cables.) Fig. C2 shows the sequencer flow chart. The sequencer can be manually started, in which case collecting and dumping the data are separately mandated. When the FLASH button is pushed the Biomation trigger is armed, then a downward transition appears at TRIGGER BIOMATION, and about 6 μsec later, the lamp is flashed.

The sequence stops until the DUMP button is pushed, at which time the memory dump described above is initiated. Now the decay curve from the single flash can be displayed, and run conditions can be adjusted. Careful examination of several individual curves is recommended before proceeding to add curves.

When the single curves are to be averaged, the mode switch is turned to AUTO. The repetition rate is turned to FAST (7 Hz) or SLOW (2 Hz), depending on the lamp. As stated earlier, the dump takes about 131 nsec. The maximum flash rate is then about 7 Hz. For the spark gap, the repetition rate was set to exactly 7 Hz. Only a short time (3.5 msec) was allowed after the flash before the dump is started, but this is enough for any decay for which the spark gap is used. The flashlamp circuit allows a maximum rate of only 2 Hz. At this rate, the sequencer can wait .35 sec before initiating a memory dump. Therefore, decay curves as long as .35 sec (i.e., sample interval $\leq$1 msec) can be automatically averaged. Slower decay curves must be manually averaged.

After waiting 3.5 msec or .35 sec, the dump is started. Whether or not the dump is completed, the sequence is restarted .15 sec later. If the lamp flashed and triggered the Biomation, there will be a FLAG so that the new

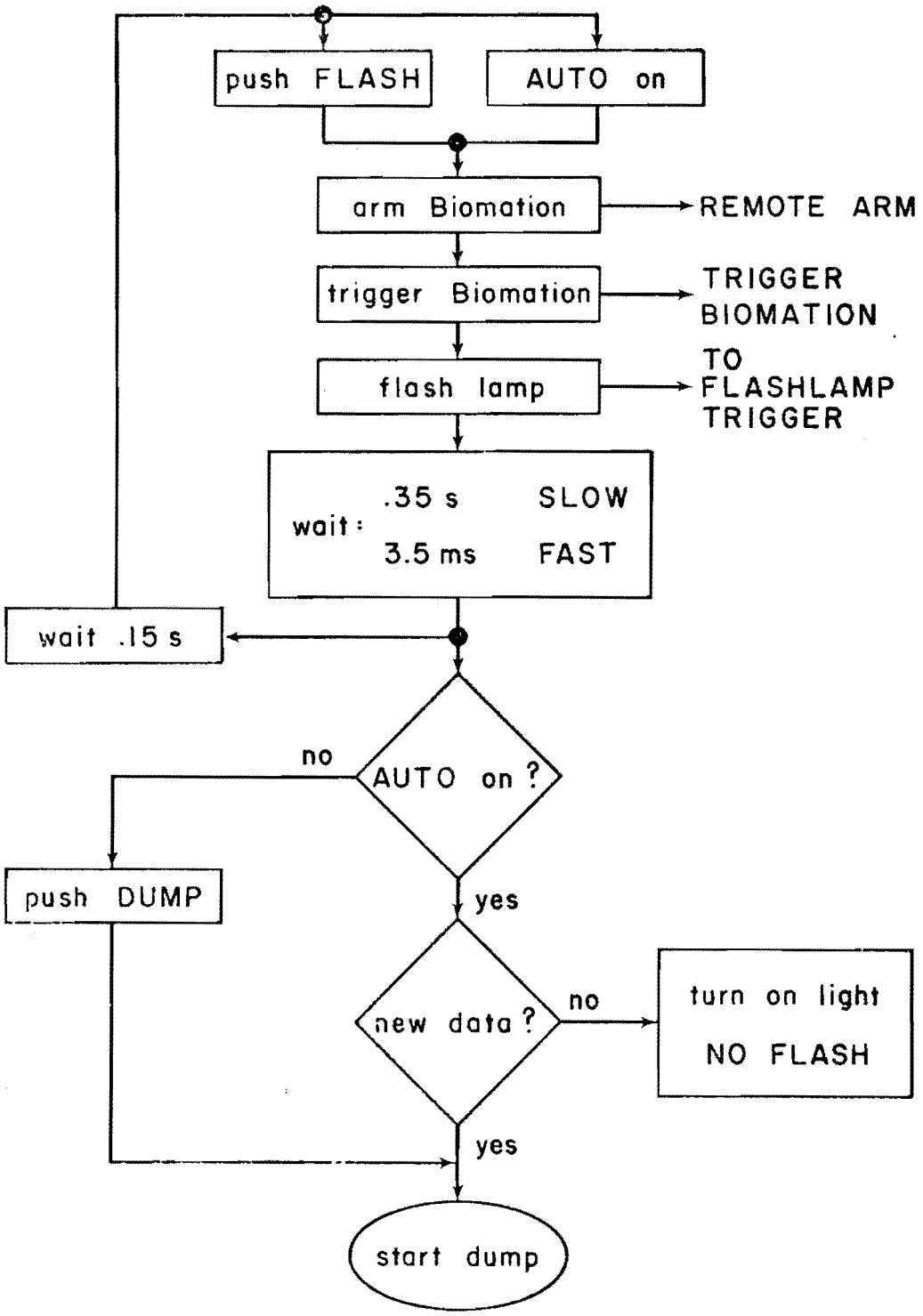

Fig. C2 Flow Chart of "Sequencer" Section of Interface

curve is dumped. But if there is no FLAG, the Interface turns on a NO FLASH indicator, and waits for the next flash, without dumping.

Fig. C3 shows the dumper circuit (all TTL). It is made mostly of monostable multivibrators, which unfortunately are sensitive to RFI. The FLASHLAMP TRIGGER output is isolated from RFI that can return after the flash, but occasionally the sequence is disrupted anyway by RFI. Sometimes the sequence stops; then it should be restarted by turning to AUTO again. At other times, a dump will follow the flash even in the manual mode, and curves are not added correctly. The solution is to flash manually, allowing the dump to occur; then block the path to the lamp before the next flash can occur. To add curves, repeat the process.

A module was built that appears to eliminate RFI transmission along the Interface → lamp cable. It is an optical coupler, pictured in Fig. C4. The one foot optical fiber eliminates the electrical connection between lamp and Interface. Only the "flash initiate" signal from the Interface can pass, and RFI from the lamp cannot reach the Interface. The FLASHLAMP TRIGGER output of the interface provides a high current to the LED. At the other end of the optical fiber, a phototransistor picks up the pulse, which is amplified and shaped. The FLASHLAMP TRIGGER output is a 50 μsec, 5 v pulse; the output of the optical coupler is a 64 μsec, +4 volt pulse with 80 nsec RT, and it is delayed 6 μsec from the input pulse. This pulse will trigger both lamps without any RFI problems. (The optical coupler's battery should be changed occasionally.)

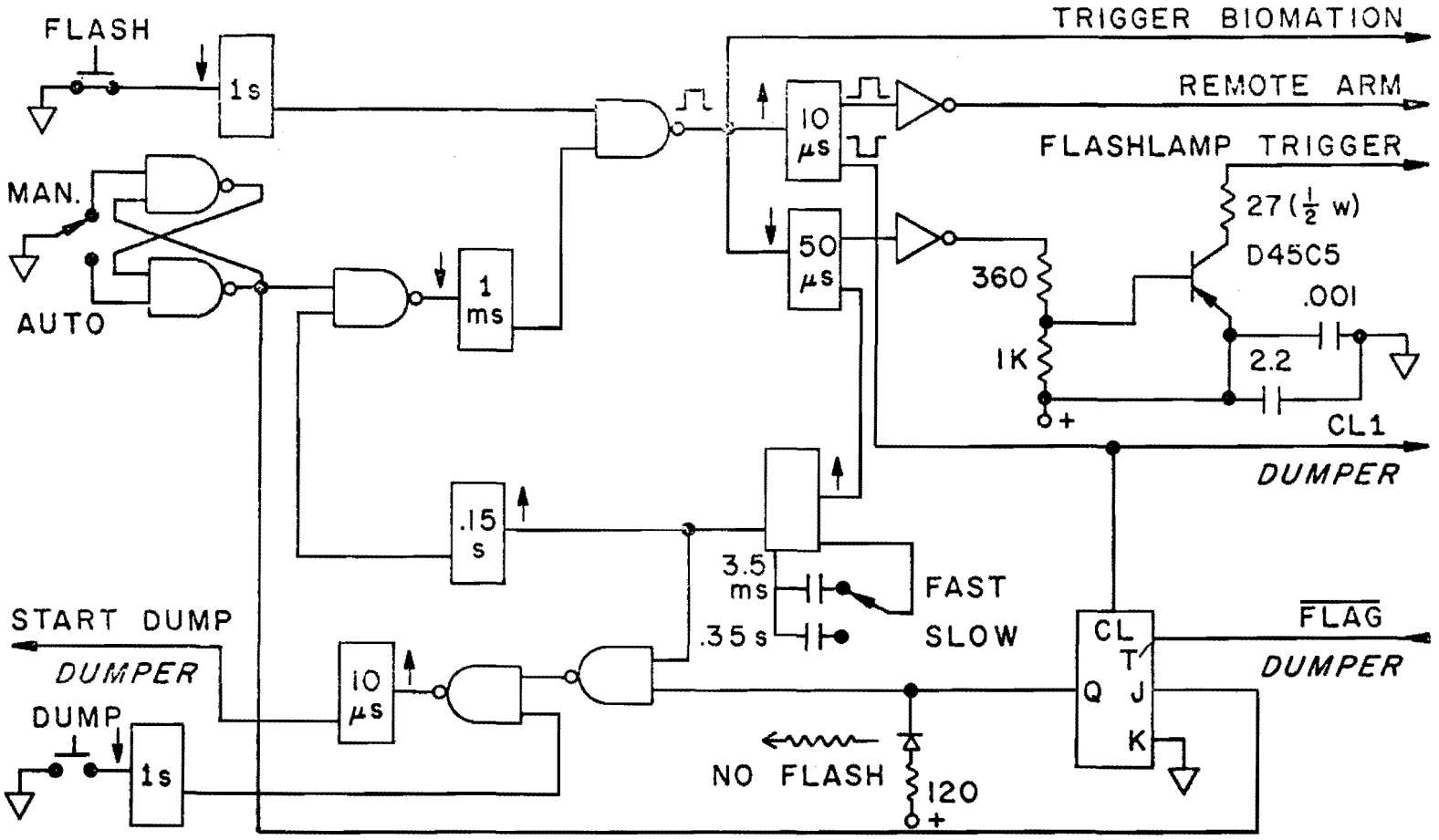

Fig. C3 Circuit Diagram of "Sequencer" Section of Interface

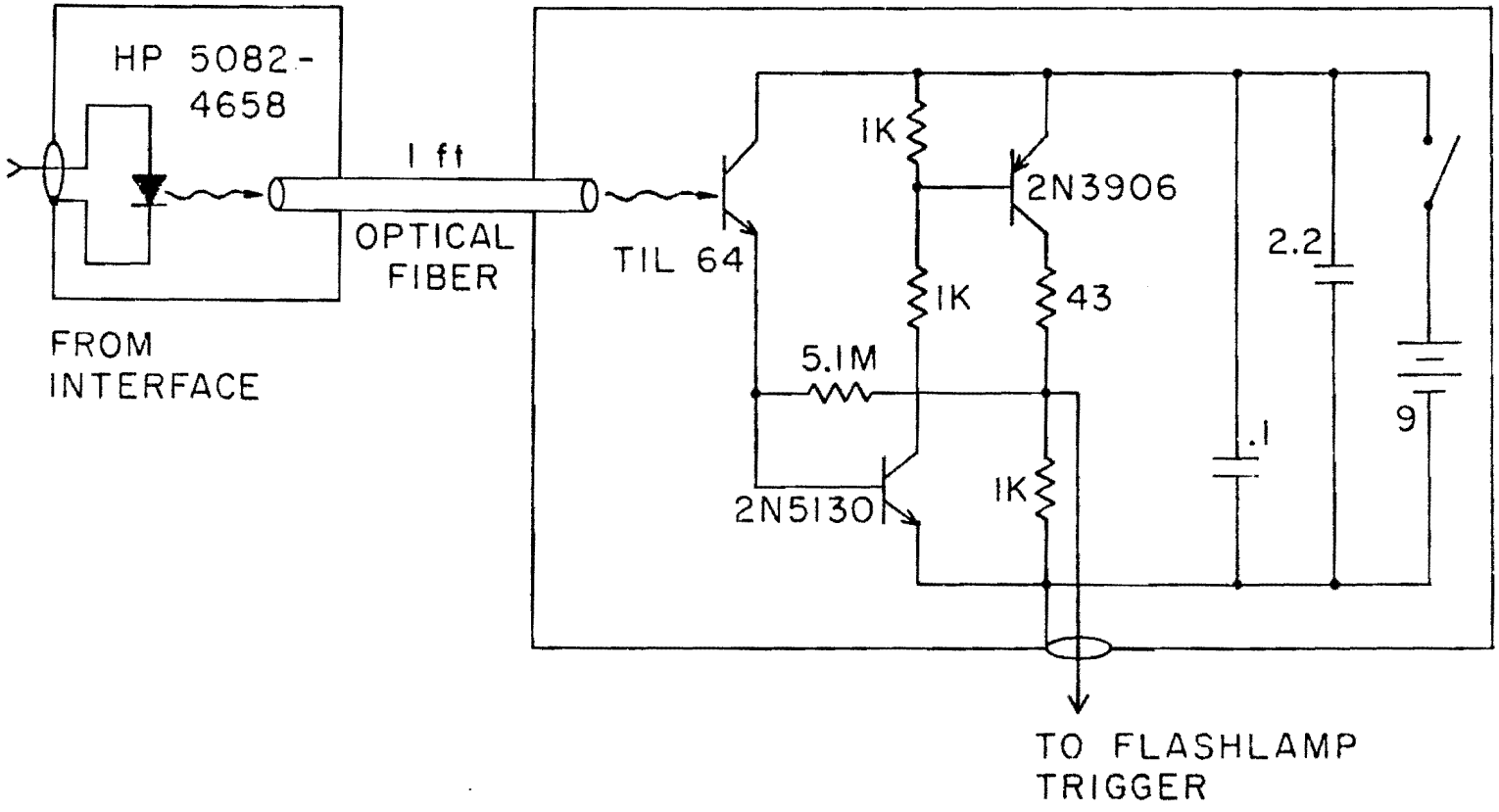

Fig. C4 Circuit Diagram of Optical Coupler for Isolating Interface from Lamp

APPENDIX D

Checklist for Decay Measurement
(Transient Digitizer)

Contents:

Page numbers in text refer to pages in the book accompanying the lifetime rig. The "slow lamp" is the flashlamp; the "long lamp" is the spark gap.

I. Set-up

A. Photomultiplier -- Cool signal PM. Attach TNC-BNC adapter to PM anode.

B. Flash lamp -- Decide on lamp.

1. Slow decays (>20 μs)

a) Slow lamp in Schoeffel housing, for monochromatic excitation of bright samples. Attach brass holders to an EG&G FX-12 flashlamp. Place the lamp either end up in the housing. Remove the back mirror to the plexiglass box. Put the EG&G TM-11 A trigger module on the platform behind the housing. Connect negative to the table by a braid. Connect positive to the lamp trigger wire through the back with the alligator clamp in the bakelite plate. Place the cubical "energy storage box" with an MHV connector, and set it to -1400 V.

b) Slow lamp in slow box, for filtered excitation of weak samples. Put the TM-11A into the slow box, allowing 2" from the HV posts to metal. Connect neg. to the box and pos. to the lamp trigger wire. (Check the lamp usage (p. 1). Replace after ~10^4 flashes.) The trigger wire should be wrapped so that top is just below the gap and the bottom is ~1/8" above ground. Plug a Fluke power supply into an interference filter. Connect it at -1400 V to the slow box with an MHV connector. Plug in the fan and plug the TM-11A into an interference filter.

2. Fast decays (<20 μs)

a) Long lamp loading. Check usage (p. 25); electrodes should be replaced after 5×10^5 flashes or if blunt. Use the special allen wrench to loosen the set screws. Turn the electrodes around, or, if both ends are

worn, get new electrodes. Center the gap and set it to the desired thickness with the metric feeler gauge. Consult Figs. 10 and 12 to set the gap. Typically set gap at <4.1 mm.

b) Long lamp set-up. Plug the Xenon 437A nanopulser into an interference filter. Connect the nanopulser to the long box with the HN cable. Tighten the three screws in the long lamp box.

C. Optics -- If the excitation comes from the Schoeffel housing, the optics are as usual. If not, the excitation cone fits into the filter box. Sweep out the filter box track, and then lock it in place, flush against front and side.

Choose the excitation filter. If you use a Corning or Schott UV-pass colored glass filter (lowest λ ~250 nm) place it on the filter box wall. If you want high-energy, broad-band excitation, use the UV-R filter centered at 220, 250, 280, or 310 nm. (Handle these carefully and keep covered when not in use. Never touch the filter surface.) Fit the cardboard mask around the filter. Slide it onto the posts in the filter box.

On the emission side, a cutoff filter is wise even if there is no danger of second order. Otherwise, the reflected flash sometimes gets through.

Mount the quartz f/1 lens (which should be covered when not in use) on the lamp box, and set it according to Table D1. Align the lamp box in its track according to Table D1.

E. Electronics

(Plug excitation electronics into a different outlet from detection electronics; the latter should be connected to a regulator.) Wheel the Tektronix 545B scope next to the signal PM (see Fig. 14). Connect the RC Low

Table D1

Lens and Lamp Box Position

Lens position is varied by moving a bar between two stops. Divide the distance between stops into tenths. Facing the press, look down from the top. Lens position is given in tenths left or right of center. Thus the bar moves from L 5/10 to R 5/10.

Lamp box position is given in inches from the end of the table. The box can move from 0" to 4", when it hits the filter box. Prevent light leak by covering the space between lamp box and filter box. Optimum positions are:

Lamp	Filter	Lens	Box
Slow	Colored	R 1/10	4"
	UV-R	L 2/10	0"
Long	Colored	R 2/10	4"
	UV-R	R 3/10	2"

Pass Filter directly to the Type L preamp input, and through a 1 ft. BNC cable to the signal PM.

Wheel the lifetime rack next to the scope. Connect "vert. sig. out" from the scope to "-input" on the Biomation. Connect the Biomation in back to the Interface (15 pin connector). Connect the 3 Interface outputs to their counterparts on the MCA Digital Processor. Connect the Teletype as instructed on p. 51. NEVER operate the teletype in the "local" mode while it is connected to the MCA! Don't run the steady state lamp as well as the lifetime apparatus, or a fuse will blow.

On slow decays (>20 μs), the interface can trigger the Biomation (connect this). For fast decays, connect the reference PM anode to "Trigger in" of the Biomation, with a BNC cable. Connect the reference PM cathode to a Fluke power supply through an MHV connector. Set the Fluke voltage and the reference PM aperture according to Table D2. Be careful not to expose the reference PM to room light, while the HV is on.

Turn on the instruments in the rack (4 switches), Interface last. Connect the Interface output "flashlamp trigger" to the "oscillator" input of the TMA-11A or "remote auto trigger" of the nanopulser through the interference inhibitor described in Appendix C.

II. Testing -- Put a mirror where the cell is. Turn the slits down. Turn on the HV of the PM's.

A. Triggering

The circuit should trigger every time the Interface sends out a pulse ("trigger Biomation"), or every time the lamp flashes (reference PM). If not, consult Table II and switch between "ext" and "ext ÷10," adjust

Table D2

Reference PM Aperture and HV

The reference PM negative pulse goes into "trigger in" (100 K on "ext" and a 1 M:100 K divider on "ext ÷ 10"). The input is limited and protected at -10 v on "ext" and -100 v on "ext ÷ 10." The "trigger level" varies a discriminator between -5 v (-50 v on "ext ÷ 10") in the 7:00 position and 0 v in the 12:00 position.

If possible, keep the PM output low (pulse volts ~15 v), but for reliable triggering higher voltage pulses may be necessary. Typical pulse voltages for various settings are:

Lamp	Filter	Aperture (mm)	HV(v)	Pulse Volts
Slow	Colored	3	800	60
		2	"	25
		1	"	12
	UV-R	1	"	70
		pinhole	"	40
		"	700	12
Long	Colored	20	800	25
		10	"	10
		5	"	3
	UV-R	5	"	25
		3	"	12
		2	"	6

the "trigger level," or vary the reference PM aperture or high voltage. If those changes fail, the lamp may be flashing incorrectly.

B. Finding trace -- Open the signal PM and flash manually in the "decay" mode. Flash manually by "erase," "start," "accumulate," "start"; "flash," "dump," "display," "start." If the flash profile is not seen turn the "trigger delay" until it is. A cw turn moves the trace left, while a ccw turn moves it right. A very small turn moves the trace far. Move the flash to where you want it.

C. Instrument Time Constant

Choose R and C of the RC Low Pass Filter such that RC ≃ "sample interval." Adjust the scope amplification so that the flash is seen. Is the time constant acceptable? How about the flash width? Is there jitter in the flash position that will bother you?

D. Pressure Cell -- Shut off the PM tubes and remove the mirror. Load a pressure cell as for the emission rig. If the excitation comes from the Schoeffel housing, orient the cell as usual. If not, rotate the platform and the cell 90°. (With the liquid cell, you must first remove the tips of the alignment posts.)

Open the slits wide to encompass the whole emission peak of interest. Turn on the PM tubes. Flash manually, and change amplification until a good trace is obtained. No trace should be as high as the cutoff of 630 counts.

E. Interference -- Close the signal PM and flash several times. Is the interference bothersome? If the interference is tiny but visible, and the signal is <5 photons/flash, the interference might be comparable to the signal after averaging. [In this case, use the "pulses" mode to

discriminate against low-level noise. Set the discriminator from 1 to 63 (10 to 630 counts), so that medium sized photons will register. Turn down the slits so that each flash produces ~2 photons.]

III. Take Data -- When manual traces are ok, set "lamp" to fast (7 HZ) or slow (2 HZ), and switch to "auto." The MCA display should light every time the lamp flashes. If the lamp does not flash, and the reference PM is used, no trace should be added, and "no flash" should light. Follow the accumulation by increasing the counts/div on the MCA display.

When a good curve is obtained (say ~120 flashes = 1 min. = 60¢ for the slow lamp or ~4200 flashes = 10 min. for the long lamp), turn from "auto" to "manual." "display." Read out by turning to "read," have teletype on "line" and push "start." Store by turning to "transfer (A to B)," set B to 2 at right, push "start," and reset B to 1.

IV. Process Data

A. Tape → punch cards

Accumulate punched tape and roll it onto a reel, as on p. 53. Transform the reel into punched cards on the IBM 1800 computer (p. 61).

B. Data Reduction

Fit and plot the data using file "Decay" in MRL 1210F. The data can be fit to several equations. Deconvolution of the finite flash width is possible. Log or linear plots are available.

APPENDIX E

Checklist for Single Photon Counting

1) Set up Teletype (TTY): Check amounts of paper and paper tape (PT). Plug in and turn to "local." "Break" until you can grab PT under TTY. Press "release" and pull through 1 m of PT.

   Press "break" briefly several times so that there are holes for the optical reader. Turn to off. Do not turn to "local" while TTY is hooked to MCA.

2) Set up the multichannel analyzer (MCA) as in Appendix D. Only one setting is different for SPC operation: the Accumulate Mode is switched to "PHA." Plug in the MCA, and make sure the steady state lamp is off. Turn on the two MCA power switches. Plug the TTY data line into "serial out" at the back of the MCA. Turn the TTY to "line."

3) Set up the pressure cell, long lamp, and filters as in Appendix D. The only change is that the electrode gap should be about one mm and well centered, rather than 3-4 mm (see Figs. 10 and 12). Also, instead of the 3' high-voltage cable from Nanopulser to lamp, use a 10' one, to reduce RFI. Set the Ref. PM aperture and voltage as in Table D2:

   UV-R filter, 5 mm, 600 V

   colored glass, 20 mm, 700 V

   Set the lens and box position as in Table D1:

   UV-R filter, R 3/10, 2" forward

   colored glass, R 2/10, full forward

   Unhook the braided MHV power cable from the PM under the table, and connect to the MVH connector of the Ref. PM.

4) Apply N_2 at a flow rate of 2.0 units to the long lamp gap. Leave on while the lamp is flashing, to prevent ozone buildup. Make sure the other tubes are closed.

5) Roll over the Ortec bin, and rest it on the emission rig table. Store the preamps away. Use shielded cables of minimum length for all connections. Cable lengths are given in Fig. 15.

6) Ref. PM is hooked to the left hand discriminator (LHD) (3 ft).
Sig. PM is hooked to RHD, by a tight fit (1/2 ft.).

7) Hook the photon counter (PC) "Neg In A" to LHD "out" (2 ft.).
Hook LHD "out" to "start input" of the time to pulse height converter (TPHC) front (3 ft.). Hook RHD "out" to the upper connector of Delay (2 ft.). Hook the lower connector of Delay to the TPHC "stop input" (1/2 ft.). Hook "true stops" from the TPHC back to "stops" on the SPC control (1/2 ft.). Hook "TPHC out" in front, to the input of the MCA analog-to-digital converter (ADC)(3 ft.).

8) The instrument controls should not be touched, unless they are different from the following

PC

selector	- A
mode	- recycle
hold	- off
B input	- 1 msec
preset inner	- 3
outer	- 1

LHD

gain	- 20
disc level	- to be set
monitor	- no matter

RHD

gain	- 20
disc level	- 18-20 turns
monitor	- no matter

Delay typically ~20 nsec

4 and 16 nsec "in." All others "out."

TPHC back

sync	- int. stop	SCA mode	- normal
reset	- 120 ns	mode	- out

TPHC front

range	- to be set	inhibit	- out
multiplier	- to be set	anti coinc	
delay	- max. CW		

MCA ADC

lower disc	- 0	input offset switch	- 0
upper disc	- 0	base line monitor	- off
output range	- 256	time to peak	- var (max. CCW)
output offset	- 0	coincidence (both)	- free

SPC Control

stops	sec - 1
man. override	- off

9) Plug in the Ortec bin and the SPC Control. Turn them on. Set the Sig. PM voltage to -1400 v. Turn on the Ref. and Sig. PM's. Push "stop, start, reset" on the PC and "clear, start" on the SPC control. Set TPHC range and multiplier to the full scale desired (usually at least 3 x lifetime).

10) Plug the Nanopulser (which is 10' from emission rig) into an interference filter and turn on. Turn "remote auto trigger" full CW, so that lamp is flashing at 50-60 Hz. Looking at the PC, turn up the LHD

level until the count drops below 60, then turn it back to where it is steady between 50 and 60. A card placed between lamp and Ref. PM should stop the counting. If changing the discriminator level (a fine adjustment) does not achieve a steady 50-60 counts, the coarse adjustments are the aperture and bias voltage of the Ref. PM.

11) The RHD level should be set as explained in Appendix A (18-20 turns). With the Sig. PM shutter closed, the SPC control should not be counting (these are interference-generated counts).

12) Set PC B input selector to "ext" so that it will count forever. Open Sig. PM shutter. Set monochromator wavelength and slits as desired. The SPC control should now be counting. If not, open slits (not beyond 10 mm). To increase signal counts, the RHD level can be lowered, but this may allow RFI to disrupt data.

13) Now test the ratio of starts to stops (S/S). S/S is the display on the photon counter over the display on the SPC Control. It should be about 10.

14) Push PC "stop, reset." Now press PC "start" and SPC control "clear" simultaneously. When starts (PC display) reaches 1000, what is stops (SPC Control display)? If S/S is too small, turn down the slits (not below zero!). If S/S is too large, open the slits (not beyond 10!) or increase gap (not beyond 4 mm). Repeat step 14.

15) Set MCA counts/div full CW (100 counts/div). Set group selectors A & B at 1. Turn vertical gain max. CW.

16) To take a decay curve, turn off lamp, press "stop, reset, start" on PC and "clear" on SPC Control; set MCA function to "erase," push "start,"

"accumulate," "start." Now start lamp. Displays should be counting and MCA accumulating.

17) After about 1/4 hour, turn off lamp, set to "read," push "start," and read out should begin. Increase pressure. Take down starts and stops and note S/S. Repeat steps 14) and 16).

18) To produce RT data as fast as possible, the lamp can be left on for the whole run. During the 3 min. printout, increase pressure, test S/S at new pressure, and adjust slits. After printout, erase and push "accumulate" but not "start"; the channels that receive counts will sparkle. For best results, leave a long tail; that is, make sure the last 50 channels receive very few counts. A background is not necessary for SPC since one just fixes it at zero in the program (dark counts are negligible).

19) At the end of a run, turn TTY off, unplug from "serial out," turn to "local," type two "control C's." Roll up paper tape, and coil up the cords. Turn off equipment and put away. Reset "accumulate mode" to "MCS." Reset disc levels to 13 turns, PC B input to "1 msec." Sig. PM to -1200 v and Ref. PM to -800 v. Return trigger PM MHV cable to Ref. PM. Replace cables on Ortec equipment for steady state use. Turn off N_2 and put away lamp.

APPENDIX F

Oscillator and Power Supply

A combination oscillator and power supply was built to aid in testing electronic components in the lab. It contains a 180 mA, +5 v power supply and another at 30 mA, ±15 v, which can be accessed by banana plugs. If in addition the oscillator is turned on, only 15 mA is available at ±15 v.

The oscillator, an Intersil 8038 waveform generating chip, is connected as shown in Fig. F1. Its frequency is variable from .01 Hz to 1 MHz. At high frequencies it becomes quite hot, but this is normal. There is a coarse and a fine frequency adjustment. Three outputs are available: sine, triangular, and digital. The sine wave has a ±13 v sweep, triangle ±5, and digital 0 to +5, which is TTL compatible.

The digital pulse width and duty cycle can be varied by adjusting the "fine frequency" and "pulse width" controls in the "pulse" mode. In this mode, the sine and triangular waveforms are skewed, and one can even generate a sawtooth. Another feature is the voltage controlled oscillator (VCO) input. As the DC input level is increased from 0 to 10 v, the output frequency rises from 0 Hz.

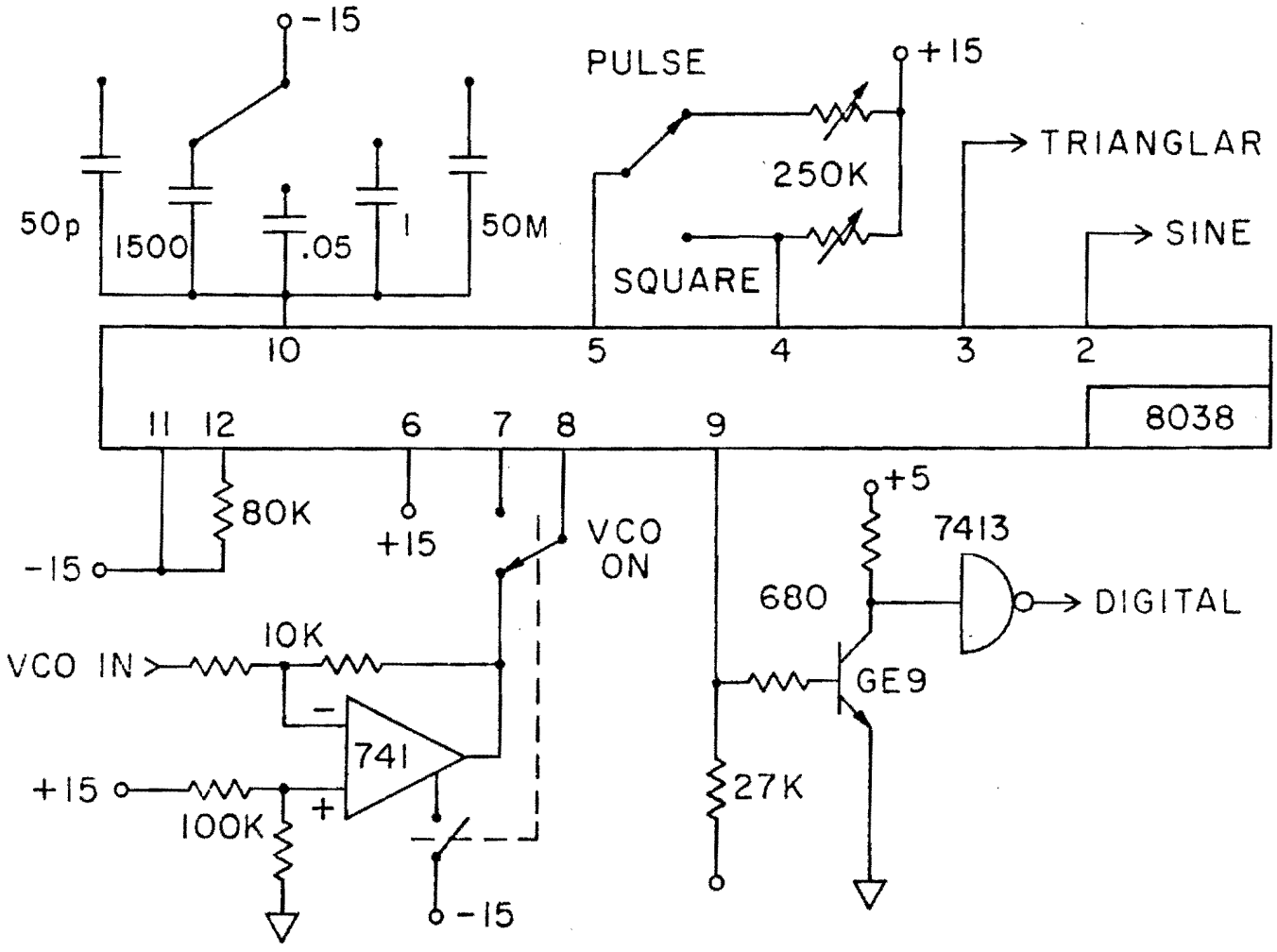

Fig. F1 Circuit Diagram of Oscillator

APPENDIX G

Tabulated Data for Impurity-doped Alkali Halides

The tables in this appendix give tabulated data for the effect of pressure on the optical properties of alkali halides doped with Cu^+, Ag^+, In^+, and Tl^+. Pressures are in kilobars (kbar), temperatures in °K, peak positions and halfwidths in 10^3 cm^{-1} (KK), and lifetimes in microseconds (μsec). Values in Tables 1-3 are taken from least square fits to the data (as explained in Part 3); those in Table 6 are taken from smooth curves through the data points; and values in Tables 4, 5, and 7-9 are individual data points. In the potassium halides, values at 20 kbar or below refer to the fcc phase, while those at 25 kbar or above refer to the sc phase. Unless otherwise specified, the temperature is room temperature, about 295°K.

Table G1

Emission Peak Position (in 10^3 cm^{-1}) vs. Pressure in Cu^+- and Ag^+-doped Alkali Halides

Compound	Pressure (kbar)											
	0	10	18	20	25	30	40	60	80	100	120	140
NaCl:Cu	28.17	28.78		29.36		29.92	30.46	31.47	32.38	33.19	33.91	34.53
NaBr:Cu	27.68	28.28		28.86		29.42	29.96	30.99	31.95	32.82		
NaI:Cu	26.64	27.22		27.77		28.28	28.76	29.61	30.33	30.91	31.36	31.67
KCl:Cu	24.73	25.58	26.25		24.12	24.37	24.84	25.74	26.56	27.31	27.99	28.58
KBr:Cu	25.79	26.60	27.25		23.45	23.70	24.17	25.01	25.72	26.28		
KI:Cu	24.99	25.77	26.39		22.74	22.84	23.04	23.36	23.61	23.77	23.85	23.85
NaBr:Ag	38.02	38.63		39.23		39.84	40.44					
KCl:Ag	36.26	37.35	38.22		34.69	35.06	35.75	36.97	37.97	38.74	39.29	
KBr:Ag	34.78	36.06	37.09		37.05	37.10	37.20					

Table G2

Emission Peak Halfwidth (full width at half maximum in 10^3 cm^{-1}) vs. Pressure in Cu^+- and Ag^+-doped AH

Compound	Pressure (kbar)											
	0	10	18	20	25	30	40	60	80	100	120	140
NaCl:Cu	2.09	2.12		2.15		2.18	2.21	2.26	2.32	2.38	2.44	2.49
NaBr:Cu	1.87	1.95		2.04		2.12	2.21	2.38	2.54	2.71		
NaI:Cu	1.73	1.70		1.66		1.62	1.59	1.51	1.44	1.36	1.29	1.22
KCl:Cu	2.33	2.44	2.52		1.91	1.87	1.80	1.66	1.52	1.37	1.23	1.09
KBr:Cu	2.21	2.21	2.21		2.28	2.28	2.28					
KI:Cu	2.21	2.09	2.00		1.97	1.92	1.83	1.63	1.43	1.24	1.04	
NaBr:Ag	2.34	2.28		2.23		2.18	2.13					
KCl:Ag	3.39	3.17	2.99		2.99	2.99	3.00	3.01	3.02	3.04	3.05	
KBr:Ag	3.75	3.25	2.85		2.89	2.85	2.77					

Table G3

Emission Lifetime (in microseconds) vs. Pressure in Cu^+- and Ag^+-doped Alkali Halides

Compound	Pressure (kbar)											
	0	5	10	18	20	25	30	40	60	80	100	120
NaCl:Cu	43.1		48.7		54.1		59.2	64.0	72.7	80.3	86.8	92.2
NaBr:Cu	142		152		163		173	183	203	224	244	
NaI:Cu	23.8		30.1		35.6		40.2	43.9	48.7	50.0	47.7	
KCl:Cu	25.0	27.0	29.0	32.2		46.6	47.3	48.8	51.6	54.4	57.2	
KBr:Cu	91.6	101	110	125		140	144	151	167	183	198	214
KI:Cu	12.4	17.4	22.3	30.3		7.56	8.03	8.97	10.8	12.7	14.6	
NaBr:Ag	7.27		11.7		14.6		16.1	16.0				
KCl:Ag	12.3	14.1	15.8	18.6		49.9	48.7	46.2	41.4			
KBr:Ag	<1	3.87	7.53	13.4		13.2	13.9	15.3				

Table G4

Low Energy Fraction in KH:In
(Temperature (°K) above and LE area fraction below in each set)

			KCl:In			
31 kbar	297	221	154	111		
	.56	.71	.84	.91		
37 kbar	294	212	159	130	108	
	.29	.27	.29	.30	.34	
40 kbar	295	238	176	150	118	
	.23	.17	.13	.12	.10	
			KBr:In			
4 kbar	297	221	155	110		
	.40	.30	.30	.31		
34 kbar	297	213	152	130	110	
	.52	.70	.83	.88	.89	
37 kbar	298	236	176	145	124	110
	.30	.36	.45	.49	.51	.52
40 kbar	295	213	163	136	110	
	.11	.18	.23	.28	.30	
43 kbar	295	228	174	144	126	110
	.12	.12	.12	.11	.11	.10
			KI:In			
6 kbar	298	228	145	107		
	.81	.89	1	1		
10 kbar	297	226	155	112		
	.57	.74	.89	.95		
15 kbar	297	222	174	130		
	.46	.53	.64	.77		
18 kbar	297	225	162	135		
	.37	.56	.72	.80		
20 kbar	294	225	155	106		
	.40	.55	.62	.71		
40 kbar	289	230	168	134	115	
	.72	.85	.94	.95	.94	

Table G5

Low Energy Fraction in Tl^+-doped Compounds
(Temperature (°K) above and LE area fraction below in each set)

			KBr:Tl			
4 kbar	295	214	155	126	110	
	.34	.42	.58	.68	.73	
10 kbar	289	207	163	126	110	
	.21	.14	.13	.12	.11	
			CsI:Tl			
6 kbar	301	223	168	139	119	109
	.91	.90	.76	.70	.70	.71
10 kbar	294	221	157	131	108	
	.78	.77	.67	.61	.59	
16 kbar	294	218	164	135	113	
	.60	.56	.45	.46	.57	
24 kbar	295	214	156	126	108	
peak 1	.08	.04	.04	.05	.07	
peak 2	.76	.84	.91	.95	.94	
32 kbar	295	209	154	130	104	
	.37	.53	.69	.81	.92	
37 kbar	301	221	160	128	113	116
	.22	.24	.34	.37	.41	.43
40 kbar	297	217	154	128	110	
	.27	.26	.14	.12	.09	

Table G6

Emission Lifetime vs. Pressure
(Time constant in microseconds)

Compound	Pressure (kbar)										
	5	10	15	20	25	30	35	40	45	50	55
KCl:In	4.14	4.10	4.06	4.01	6.4	3.85	2.32	1.37	1.07	1.04	1.02
KBr:In	2.52	2.33	2.23	2.18	3.77	2.77	1.94	1.29	1.06	.92	.85
KI:In	2.36	1.98	1.75	1.60	2.37	2.00	1.63	1.26			
NaCl:In		3.0			3.0			3.0			
KBr:Tl	.319	.336	.362	.397	.38	.38	.38	.38			
CsI:Tl	.67	.47	.346	.268	.217	.202	.194	.191			

Table G7

Emission Lifetime vs. Temperature in KH:In
(Temperature (°K) above and lifetime (μsec) below, in each set)

			KCl:In			
26 kbar	298	220	151	122		
peak X	7.31	7.14	8.70	7.72		
31 kbar	298	200	155	130	111	
peak X	3.61	5.11	5.48	6.25	6.57	
34 kbar	295	229	167	135	110	106
peak X	2.96			4.94	8.80	
peak T	2.36	2.62	2.69	2.64		1.91
38 kbar	298	215	160	130	116	
peak T	1.42	1.62	1.55	1.55	1.62	
53 kbar	295	210	150	130	113	
peak T	1.02	1.19	1.22	1.21	1.31	
			KBr:In			
4 kbar	295	208	164	156	129	125
peak X	2.26	2.30	2.57		2.11	
peak T	2.42	2.43		2.53		2.31
18 kbar	293	188	125			
peak T	2.04	2.03	1.95			
26 kbar	226	171	147	123	110	
peak X	4.41	4.49	4.26	4.39	4.30	
			KI:In			
6 kbar	296	224	168	141	123	107
peak X	2.40	2.56	2.62	2.84	2.87	2.99
15 kbar	300	221	166	136	118	105
peak T	1.75	2.05	2.23	2.44	2.65	2.65

Table G8

Emission Lifetime vs. Temperature in Tl^+-doped Compounds
(Temperature (°K) above and lifetime (μsec) below, in each set)

			KBr:Tl			
4 kbar	296	221	162	110		
peak X	.315	.571	1.38	7.70		
10 kbar	299	211	156	120	105	
peak T	.342	.876	3.05	13.6	38.0	
18 kbar	301	234	166	144	127	108
peak T	.465	.806	2.88	8.94	24.6	69.0
			CsI:Tl			
6 kbar	292	216	156	115		
peak 1	.730	1.00	1.78	2.67		
16 kbar	286	182	137	112	110	
peak 1					2.07	
peak 2	.363	.585	.964	1.69		
24 kbar	297	215	164	134	112	104.5
peak 2	.210	.301	.469	.911	2.29	5.49
32 kbar	297	225	160	134	109	
peak 2	.186	.296	.726	1.25	4.13	
40 kbar	299	230	170	142	125	109
peak 3	.204	.353	1.40	4.32	15.2	41.2

Table G9

Lifetime (μsec) vs. Pressure for Tl^{+}- and Pb^{++}-doped Crystals Not Exhibiting a Jahn-Teller Doublet

Compound	Pressure (kbar)				
	8	16	24	32	40
NaCl:Tl	.89	.90	.88	.90	.98
NaBr:Tl	.39	.42	.45	.50	.50
NaCl:Pb	.89	.98	1.06	1.14	1.10
NaBr:Pb	.58	.93	2.38	1.82	1.13

LIST OF REFERENCES

1. H. G. Drickamer, Solid State Phys. 17,1(1965).

2. H. G. Drickamer and C. W. Frank, Electronic Transitions and the High Pressure Chemistry and Physics of Solids, Chapman and Hall (London), 1973.

3. P. W. Bridgman, The Physics of High Pressure, Dover Publications (New York), 1970.

4. G. J. Piermarini, S. Block, J. D. Barnett, and R. A. Forman, J. Appl. Phys. 46, 2774 (1975).

5. H. K. Mao, and P. M. Bell, Science 191, 851 (1976).

6. R. A. Fitch, T. E. Slykhouse, and H. G. Drickamer, J. Opt. Soc. Amer. 47, 1015 (1957).

7. A. S. Balchan and H. G. Drickamer, Rev. Sci. Instr. 32, 308 (1961).

8. C. C. Bradley, High Pressure Methods in Solid State Research, Plenum Press (New York), 1966.

9. R. S. Bradley (ed.), Advances in High Pressure Research, Academic Press (New York), 1966.

10. W. Paul and D. M. Warschauer (eds.), Solids Under Pressure, McGraw-Hill (New York), 1963.

11. R. H. Wentorf (ed.), Modern Very High Pressure Techniques, Butterworth and Company (London), 1962.

12. H. W. Leverenz, An Introduction to Luminescence of Solids, Dover Publications (New York), 1968.

13. P. Goldberg (ed.), Luminescence of Inorganic Solids, Academic Press (New York), 1966.

14. D. Curie, Luminescence in Crystals, Wiley (New York), 1963.

15. C. C. Klick and J. H. Schulman, Solid State Phys. 5, 97 (1957).

16. W. B. Fowler, Physics of Color Centers, Academic Press (New York), 1968.

17. D. L. Dexter, Solid State Physics 6, 353 (1968).

18. H. A. Bethe and R. Jackiw, Intermediate Quantum Mechanics (2nd ed.), W. A. Benjamin (Reading, MA), 1973.

19. J. B. Birks and I. H. Munro, Prog. Reaction Kinetics V, 4 (1967).

20. B. Y. Okamoto, Ph.D. Thesis, University of Illinois (1974).

21. G. S. Zavt and N. N. Kristofel', Opt. Spectrosk. 13, 229 (1962).

22. W. B. Fowler and D. L. Dexter, Phys. Rev. 128, 2154 (1962).

23. W. D. Drotning, Ph.D. Thesis, University of Illinois (1975).

24. B. Dibartolo, Optical Interactions in Solids, Wiley (New York), 1968.

25. C. E. Tyner, Ph.D. Thesis, University of Illinois (1977).

26. G. L. House, Ph.D. Thesis, University of Illinois (1977).

27. C. E. Tyner, W. D. Drotning, and H. G. Drickamer, J. Appl. Phys. 47, 1044 (1976).

28. K. W. Bieg and H. G. Drickamer, J. Appl. Phys. 48, 426 (1977).

29. H. G. Drickamer, C. W. Frank, and C. P. Slichter, Proc. Nat. Acad. Sci. USA 69, 933 (1972).

30. B. Y. Okamoto, W. D. Drotning, and H. G. Drickamer, Proc. Nat. Acad. Sci. USA 71, 2671 (1974).

31 H. W. Offen, in Organic Molecular Photophysics V. 1, edited by J. Birks (Wiley, New York, 1973), Chap. 3.

32. W. D. Drotning and H. G. Drickamer, Phys. Rev. B 13, 4586 (1976).

33. W. D. Drotning and H. G. Drickamer, Phys. Rev. B 13, 4568 (1976).

34. K. W. Bieg and H. G. Drickamer, J. Chem. Phys. 66, 1437 (1977).

35. D. W. Gregg and H. G. Drickamer, J. Appl. Phys. 31, 494 (1960); J. Chem. Phys. 35, 1780 (1961).

36. K. W. Bieg, Ph.D. Thesis, University of Illinois (1976).

37. M. R. Zatzick, E-O Systems Design June, 20 (1972).

38. G. A. Morton, Appl. Optics 7, 1 (1968).

39. J. D. Ingle, Jr. and S. R. Crouch, Anal. Chem. 44, 777 (1972).

40. H. V. Malmstadt, M. L. Franklin, and G. Horlick, Anal. Chem. 44, 63A (1972).

41. W. R. Ware, in Creation and Detection of the Excited State, edited by A. Lamola (Dekker, New York, 1971), Chap. 2.

42. J. Zynger and S. R. Crouch, Appl. Spectrosc. 26, 631 (1972).

43. John Hook, private communication.

44. RCA 1P28 specification sheet and EMI manual.

45. D. E. Donohue and R. C. Stern, Rev. Sci. Inst. 43, 791 (1972).

46. M. A. West and G. S. Beddard, Amer. Lab. November, 77 (1976).

47. A. E. W. Knight and B. K. Selinger, Aust. J. Chem. 26, 1 (1973).

48. T. Binkert, H. P. Tschanz, and P. E. Zinsli, J. Luminescence 5, 187 (1972).

49. K. Kojima, M. Sakurai and T. Kojima, J. Phys. Soc. Japan 24, 815 (1968).

50. K. Fussgaenger, Phys. Status Solidi 36, 645 (1969).

51. T. P. Martin and W. B. Fowler, Phys. Rev. B 2, 4221 (1970).

52. A. S. Barker, Jr. and A. J. Sievers, Rev. Mod. Phys. 47, 1-179 (1975).

53. M. Li, M. de Souza, and F. Luty, Phys. Rev. B 7, 4677 (1973).

54. R. L. Bateman and W. J. van Sciver, Phys. Status Solidi B 46, 779 (1971).

55. A. Niilisk and A. Laisaar, Phys. Status Solidi 33, 851 (1969).

56. G. Baldini, A. Jean, and G. Spinolo, Phys. Status Solidi 25, 557 (1968).

57. R. Onaka and S. Yano, J. Phys. Soc. Japan 20, 1740 (1965).

58. M. Tomura and H. Nishimura, J. Phys. Soc. Japan 18, Suppl. 2, 277 (1963).

59. T. A. Kuketaev, et al., Opt. Spectrosk. 27, 83 (1969).

60. S. A. Mack and W. J. van Sciver, Phys. Status Solidi B 46, 193 (1971).

61. M. Piccirilli and G. Spinolo, Phys. Rev. B 4, 1339 (1971).

62. R. Kubo and Y. Toyozawa, Progr. Theoret. Phys. 13, 160 (1955).

63. N. E. Lushchik and T. A. Kuketaev, Opt. Spectrosk. 25, 889 (1968).

64. W. Dultz, Phys. Status Solidi 34, 95 (1969).

65. R. Smoluchowski, in Colloque Ampere IV (North-Holland, Amsterdam, 1969).

66. W. E. Hagston, J. Phys. C: Solid State Phys. 5, 691 (1972).

67. K. Fussgaenger, W. Martienssen and H. Bilz, Phys. Status Solidi 12, 383 (1965).

68. M. D. Sturge, Solid State Physics 20, 91 (1967).

69. R. Englman, The Jahn-Teller Effect in Molecules and Crystals, (Wiley-Interscience, New York, 1972).

70. C. C. Klick and W. D. Compton, J. Phys. Chem. Solids 7, 1970 (1958).

71. R. Edgerton and K. Teegarden, Phys. Rev. 129, 169 (1963); 136, A1091 (1964).

72. Atsuo Fukuda, Phys. Rev. B 1, 4161 (1970).

73. V. Gerhardt and W. Gebhardt, Phys. Status Solidi B 59, 187 (1973).

74. Robert Illingworth, Phys. Rev. 136, A508 (1964).

75. S. Benci, M. P. Fontana, and M. Manfredi, Phys. Status Solidi B 81, 603 (1977).

76. A. Ranfagni, Phys. Rev. Lett. 28, 743 (1972).

77. A. Ranfagni and G. Viliani, J. Phys. Chem. Solids 35, 25 (1974).

78. A. Ranfagni and G. Viliani, Phys. Rev. B 9, 4448 (1974).

79. A. Ranfagni, et al., Sol. St. Comm. 14, 1169 (1974).

80. M. Bacci, et al., Physics Letters 50A, 405 (1975).

81. M. Bacci, et al., Phys. Rev. B 11, 3052 (1975).

82. M. Bacci, et al., Phys. Rev. B 12, 5907 (1975).

83. W. D. Drotning and H. G. Drickamer, Phys. Rev. B 13, 4576 (1976).

84. A. Fukuda, A. Matsushima, and S. Masunaga, J. Lumin. 12/13, 139 (1976).

85. A. Niilisk and A. Laisaar, Phys. Status Solidi 33, 851 (1969).

86. L. S. Dang, et al., Phys. Rev. Lett. 38, 1539 (1977).

87. Atsuo Fukuda, J. Phys. Soc. Japan 40, 776 (1976).

88. M. F. Trinkler, et al., Opt. Spectrosk. 19, 378 (1965).

89. M. F. Trinkler and I. K. Plyavin, Phys. Status Solidi 11, 277 (1965).

90. S. Masunaga, I. Morita, and M. Ishiguro, J. Phys. Soc. Japan 21, 638 (1966).

91. K. W. Bieg, D. L. Woracek, H. G. Drickamer, J. Appl. Phys. 48, 639 (1977).

92. W. D. Drotning, Optical Transitions vs. Pressure (unpublished notebook).

93. L. Reiffel, Phys. Rev. 114, 1493 (1959).

VITA

David Ira Klick was born in Washington, D. C., on August 13, 1951. He attended public schools in Washington, D. C. and London, England, graduating from Woodrow Wilson High School in June, 1969. In June, 1973, he received a Bachelor of Arts *cum laude* in Physics from Lawrence University in Appleton, Wisconsin. He received a Master of Science degree in Physics from the University of Illinois at Urbana-Champaign in August, 1974. On June 21, 1975, he married Beverly Anne Schwinn. He is a member of the American Physical Society. His thesis research was done under the direction of Professor H. G. Drickamer.